Influences of Climate Change on Western North Pacific and North Atlantic Landfalling Tropical Cyclones and Their Impacts as Inferred from High-resolution Model Simulations

CHEN, Jilong

A Thesis Submitted in Partial Fulfilment
of the Requirements for the Degree of
Doctor of Philosophy
in
Earth and Atmospheric Sciences

The Chinese University of Hong Kong
September 2019

Thesis Assessment Committee

Professor LEE Shing Yip (Chair)

Professor TAM Chi Yung Francis (Thesis Supervisor)

Professor YIM Hung Lam Steve (Committee Member)

Dr. CHEUNG Kevin (External Examiner)

Abstract

Associated with strong winds, extreme rainfall and storm surges, tropical cyclone (TC) is one of the most devastating natural disasters to coastal regions and can inflict huge economical and human losses. Although it has been argued that global warming is almost certain to cause more intense storms, heavier rainfall and stronger storm surges globally, changes of these characteristics regionally are still not clear. In this study, changes in characteristics of landfalling TCs in two active basins, namely Western North Pacific (WNP) and North Atlantic (NA), are analysed under global warming conditions. Two scientific questions are addressed: (1) How will the landfalling TCs in these two basins change due to global warming? (2) If TCs are intensified, will these systems sustain longer over land, thereby having stronger influences over coastal regions?

Historical change of WNP land-falling TC activities from 1970 to 2016 is first examined using different best track datasets. Observations of maximum sustainable surface wind speed at landfall (hereinafter referred to as TC landfall intensity) of intense storms (Typhoon class or stronger) indicates a marked increasing trend of $\sim$2 m/s (6.7%) per

decade. Superimposed onto such long-term rise are strong inter-annual variations in the TC landfall intensity, which is closely associated with the occurrence of Central Pacific (CP)-type El Niño. During CP El Niño, low-level vorticity (vertical wind shear) is enhanced (reduced) near South China Sea and WNP, thereby providing a more favorable environment for storm intensification. On the inter-decadal timescale, enhancement of landfall intensity is found to be highly related to local SST warming and weakened of vertical wind shear over the region of 10-25^oN, 115-140^oE, as revealed by stepwise regression analyses. In fact, the local SST has been increasing by $\sim$ 0.1 K per decade, implying a rise of the maximum potential intensity (MPI) by 0.75 m/s per decade, or 37.5% of the observed landfall intensity intensification rate. The vertical wind shear in this region also sees a steady reduction of 0.25 m/s per decade. While the SST change is very likely a response to global warming, the reason of reduced vertical wind shear near East Asia is less clear.

In addition to becoming stronger during landfall, WNP typhoons also tend to sustain longer and travel farther inland after landfall along the East Asia coastline. From 1970 to 2016, the sustaining time after landfall is observed to have almost doubled, or from 7 to $\sim$13 hours, and with distance traveled over land increased by about 100 km (or 67%). Moreover, the power dissipation index (PDI) computed over land areas were also doubled. Further inspection of future climate projections from the Meteorological Research Institute's 20-km resolution global atmospheric general circulation model (MRI-AGCM)

shows a similar phenomenon. In particular, by comparing the model simulated WNP TCs during the 2075-2099 period with those from 1979 to 2003, under the Special Report on Emissions Scenarios(SRES) A1B scenario, TC landfall intensity is enhanced by 3 m/s under 2.2K of SST warming in the South China Sea and WNP. Also, TCs are found to sustain 6 hours (26%) longer and travel 133 km (35%) farther over land in 2075-2099 as compared to the present era in the model environment.

In the second part of this study, 20 intense historical TCs that made landfall over the Pearl River Delta (PRD) region and brought highest storm surges in the Hong Kong waters in the past 6 decades are selected, and the potential impacts of warmer climate conditions on these landfalling TCs and their induced storm surges are investigated. In particular, these storms are replicated by the Weather Research and Forecasting (WRF) model at 15- and 3-km resolution, with its outputs used to drive the Sea, Lake, and Overland Surges from Hurricanes (SLOSH) model for simulating storm surges. The resolution of SLOSH is 7 km in open water and increases gradually to 1 km near Hong Kong. The tracks, intensities as well as the circulation structure of these 20 TCs are found to be well simulated by WRF, when verified against the Hong Kong Observatory (HKO) best track data. The average track bias is 40 km, and the root mean square error of TC maximum surface wind speed is within 20%. Relative bias of storm surge outputs from SLOSH is also within 20% compared to observations. The pseudo global warming (PGW) technique is then used to provide a warmer background climate, and the same TCs are re-simulated by

WRF. Using a new spin-up and adjustment method in conjunction with PGW, systematic increase of the peak as well as landfall intensity of TCs in the warmer future is found. On average, TC lifetime peak intensity in the 3 (15) km resolution domain is intensified by 9.4% (7.5%), while the landfall intensity is expected to rise by 11.4% (8.1%). Based on these results, a 3.4% increase of TC intensity per K SST warming can be inferred. Moreover, radius of maximum wind (RMW) of storms is found to be about 7% smaller in the warming experiments, while the storm size and potential dissipation energy (both based on area with wind speed > 17 m/s) show 10% and 18.4% increase, respectively, when TCs approach to the PRD area. Finally, averaged over all TC cases, the induced storm surges are projected to increase by about 4% (6 cm), 11% (16 cm), 9% (8 cm) and 7% (9 cm) at Tai Po Kau, North Point, Quarry Bay and Tsim Bei Tsui station, respectively. Inspection of individual cases shows that global warming can lead to storm surge height increase > 40 cm at a number of stations, for more than 20% of TCs.

In the third part of this study, PGW experiments are performed using a 6 km Geophysical Fluid Dynamics Laboratory (GFDL) regional model, for examining global warming's impact on Atlantic hurricanes making landfall over the eastern US coastline. 30 Rankine vortices are randomly seeded in Gulf of Mexico, and 30 seeds over the Caribbean Sea in the model's initial conditions. Initial dates are determined based on the large-scale steering flow, so as to guarantee a high probability of landfall at the U.S. coastline. Eventually 42 of the inserted vortices made landfall in Gulf of Mexico and near Caribbean Sea. Future

changes (2075-2099) compared to the historical period of 1975-1999 of SST, air temperature, humidity, and wind fields derived from the GFDL CM4 simulations according to the RCP 8.5 scenario are then incorporated into the model environment and the 60 vortices are re-simulated. Comparing the control and PGW runs, 8% increase of peak intensity and around 11% increase of landfall intensity are found in the warming future. Such landfall intensity intensification results in 62% (6 hour) longer sustaining time after landfall, 87% (170 km) increase of travelling distance and 52% (63 kW*h) stronger potential dissipation power along east coast of US.

摘要

伴隨著強風，極端降水和風暴潮，熱帶氣旋是沿海地區最具破壞性的自然災害之一，可造成巨大的經濟和人員損失。雖然許多研究表明全球變暖幾乎肯定會引致全球更強烈的風暴，降雨和風暴潮，但颱風在不同地區的變化仍不明確。本文分析了兩個颱風活躍地區，西北太平洋和北大西洋的登陸颱風在全球氣候變暖的條件下的變化。本次研究主要集中于兩個科學問題:（1）這兩個海域的登陸颱風在全球變暖的背景下如何改變？（2）如果颱風的登錄強度增強，這些風暴系統是否會在陸地上持續更長時間，從而對沿海地區產生更大的影響？

本文首先使用不同的風暴路徑數據研究了 1970-2016 年西北太平洋登錄颱風活動的歷史變化。觀測到的颱風登錄時之最大持續地表風速 (以下簡稱登陸強度) 顯示，颱風登陸強度正以每十年增加約 2m/s (6.7%) 的趨勢增強。除了上升的長週期變化，颱風登陸強度也表現出強烈的年際震蕩，這種年際震蕩與太平洋中部型厄爾尼諾活動密切相關。當中部型厄爾尼諾現象發生時，南海和西太平洋附近的低層渦度（垂直風切變）增強（減弱），從而為風暴增強提供了更有利的環境。在年代際時間尺度上，通過逐步回歸分析顯示，登陸強度的增強與局部海表溫度變

暖高度相關，並且在 10-25^oN，115-140^oE 區域的垂直風切變減弱。事實上，現已觀測到局部海表溫度每十年增加約 0.1 K，這導致了每十年颱風的最大潛在強度（MPI）上升 0.75 m/s。0.75 m/s 的颱風 MPI 上升佔據了觀測到的登陸強度增強率的 37.5%。該區域的垂直風切變也使每十年穩定減少 0.25 米/秒。SST 變化很可能是對全球變暖的響應，但東南亞附近垂直風切變減小的原因尚不清楚。

由於登陸強度增強，西北太平洋登錄颱風在登陸后可以維持的時間更長，從而更容易進入東亞的內陸地區。自 1970 至 2016 年間，颱風登陸后可持續的時間幾乎翻倍，從 7 小時升至約 13 小時。颱風在陸地上行進的距離也增加了約 100 公里（或 67%）。此外，登陸后在陸地上釋放的功耗指數（PDI）也增加了近一倍。基於日本氣象研究所 20 km 分辨率全球大氣環流模型（MRI-AGCM3.2s）對未來氣候變化的進一步預測也顯示了類似的現象。具體來說，在排放情景特別報告（SRES）A1B 的情景下，通過對比模擬西北太平洋颱風在 2075-2099 年間與 1979-2003 年之間的區別發現，西北太平洋颱風在南海和西北太平洋海表溫度升高 2.2K 的背景下其登錄強度增強了 3 m/s。我們還發現在現在（1979-2993）與未來（2075-2099）的實驗對比中，颱風登錄后持續的時間延長了 6 小時（26%），並且在陸地上可多行進 133 公里（35%）。

在本研究的第二部分，我們選擇了 20 个在過去 60 年中登錄珠江三角洲（PRD）並在香港水域帶來最高風暴潮的歷史性熱帶氣旋，並研究了登陸颱風及其引發的風暴潮对全球氣候變暖的響應。這些被選擇的熱帶氣旋首先用 Weather Research and Forecasting (WRF) model 進行 15/3 公里的數值模擬，其輸出的颱風路徑、海表

氣壓以及颱風尺度數據又用於驅動 Sea, Lake, and Overland Surges from Hurricanes (SLOSH) 模型來計算在香港水域帶來的風暴潮。SLOSH 在開闊水域的分辨率為 7 公里，在香港附近逐漸增加至 1 公里。與香港天文台（HKO）的最佳路徑數據進行對比發現，WRF 可以很好地模擬這 20 個 TC 的路徑，強度以及環流結構。模擬和觀測的平均路徑偏差為 40 km，TC 最大地面風速的均方根誤差也在 20% 以內。與 HKO 的觀測結果相比，SLOSH 模擬的風暴潮的相對偏差也在 20% 以內。基於良好的颱風以及風暴潮模擬結果，我們又採取了 pseudo global warming (PGW) 技術在全球氣候變暖的背景下用 WRF 來模擬相同的颱風。在運用 PGW 的期間，我們發展了一套新的模型預熱和調整方法。基於新的模型調整方法，我們發現颱風的最大和登錄強度在氣候變暖的情況下都會有系統性的增強。平均而言，3（15）km 分辨率區域的颱風最大強度增加了 9.4%（7.5%），而登陸強度預計將增加 11.4%（8.1%）。基於這些結果，我們可以推斷出海表溫度每升高 1 度，颱風的最大強度會增加 3.4‰。此外在全球氣候變暖背景下的實驗中，我們發現颱風的最大風速半徑（RMW）減小了約 7%，而颱風尺寸和潛在耗散能量（均基於風速 >17 m/s 的面積計算）在接近 PRD 時分別增加了 10% 和 18.4%。最後，考慮到所有熱帶氣旋案例的平均值，預計香港 4 個潮汐站（大浦窖，北角，鰂魚涌及尖鼻咀站）的風暴潮將增加約 4%（6cm），11%（16cm），9%（8cm）和 7%（9 cm）。對個別案例的檢測表明，全球變暖可導致超過 20%的颱風在多個站點的風暴潮高度增加 > 40 cm。

在本文的第三部分，我們應用流體動力學實驗室（GFDL）區域模型（ZETAC），基于 PGW 技术，以 6 km 的精度模拟并评估了全球變暖對大西洋颶風對美國東部

海岸線的影響。此次實驗中，在 ZETAC 模型初始條件下，我們將 60 只藍金渦旋隨機插入在墨西哥灣（30 個渦旋）和加勒比海（30 個渦旋）中。為了保證這 60 粒種子渦旋的登陸頻率，選擇的颱風模擬時間應保證颱風的引導氣流須吹向美國的海岸線。經檢測，插入的 42 個蘭金渦旋在墨西哥灣和加勒比海附近登陸。然後利用 PGW 技術，我們將 GFDL CM4 基於 RCP 8.5 排放情景得到的海表溫度、氣溫、濕度和風場在未來（2075-2099）的變化納入控制實驗環境，並重新模擬插入的 60 個渦旋。通過比較對照實驗和 PGW 實驗的模擬結果，我們發現颱風的最大強度在全球氣候變暖的情境下（2075-2099）增加 8%，登錄強度增加約 11‰ 這種劇烈的登陸強度增強可以使颱風登陸後的持續時間延長 62%（6 小時），穿越美國東部海岸線的長度增加 87%（170 公里）以及 52%（63 kW * h）更強的耗散能量（PDI）。

Acknowledgement

First of all, I would like to show the depths of my gratitude to my supervisor Professor Francis Tam, who introduced me to the research field of tropical cyclones. Three and a half years ago, I didn't think I would work in tropical cyclone research. It was him who gave me this valuable opportunity and instructed me to open the gate of typhoon exploration. He is always open minded, and I am impressed by his intelligence and knowledge. He gives us sufficient freedom in research, and provides constructive suggestions when we are stuck by some problems. If we deviate from our research topic, he can always guid us back onto the right track at the right moment. Without his support and supervise, this research would not be possible.

Second, I would like to thank to Professor Tam and our department, for the reason that they encourage and support me plenty of opportunities to attend workshops and conferences. During these activities, I was able to present my research work to other experts and exchange ideas with the scientists worldwide. Through these kinds of international communications and interactions, I was fulfilled with much more open knowledge.

I am also grateful to the thesis assessment committee members, who are Professor Lee, Professor Cheung, Professor Yim and Professor Tam, for reviewing and providing helpful comments on my work. Moreover, I want to show my deep respect to Dr. Steve Garner from GFDL, who supervised me to complete the Atlantic hurricane research when I was in exchange at Princeton. He taught me to use GFDL regional model and discussed with me for the experiment design. I do not think I could finish that project without him. The storm surge projection part is in the collaboration with Dr. Mok Hing Yim and Dr. Dickson Lau from HKO.

I would say thank you to all the friends in CUHK. They are so important to my life experience in this lovely place and city. We share happiness and sadness with each other. They encouraged me when I was down, and were truly happy for me when I got good news. All of the stories happened here will be my good memories forever.

Finally, I really want to say thanks to my family. My parents are typically traditional Chinese, and they hope I can go back home and live near them before I came to Hong Kong for my PhD study. But after they knew my decision and saw my persistence, they became to understand and stand with me. Now three years have past, and they are getting older and older. I hope I can find a good way to make them happy after my graduation.

Contents

List of Figures

List of Tables

Chapter 1

Introduction

With a low pressure center and closed circulation, tropical cyclone (TC) is a well organised rotating storm system that forms over tropical ocean, and brings strong surface winds and extreme rainfall. Based on the genesis location, TCs are called differently in different basins. Hurricanes are TCs that formed in the North Atlantic (NA) and Eastern North Pacific (ENP). Typhoons are those formed in the Western North Pacific (WNP), while in the South Pacific (SP) or Indian Ocean (IO), these storms are just called TCs.

1.1 Physics of TCs

1.1.1 Typical structure of a mature TC

As is shown in Fig. 1.1, a typical mature TC consists of an eye with about 50 km of radius, inside which winds are calm[5], and is surrounded by an eyewall of 10-20 km wide consisting of clouds[6]. Within the eyewall, there are strong cyclonic winds converging into the center at low levels. Anti-cyclonic outflows are found, associated with intense convection at the top of the system in the upper troposphere on the Northern Hemisphere. Outside the eyewall, the speed of the cyclonic/anti-cyclonic wind gradually decreases from the TC center, and active convection is organised as squall lines or spiral rainbands. A relatively clear region is usually found outside of the spiral rainbands due to weaker convection. On average, the size of a TC is about 6^o from the storm center, while for some extreme cases it can be 1000 km or larger. Generally, the most intense convection is found within 4^o from the TC center[7].

The mechanism for eye formation remains controversial. One mechanism suggests that the eye forms due to the pressure gradient which is restrained by the buoyancy force associated with the decay and radial spreading of the tangential wind field with height[8]. Another hypothesis is that the eye is driven by latent heat released at the eyewall, which forces subsidence in the storm center[9]. According to either of these mechanisms, when the air subsides, it is compressed and becomes warmer than the air outside the eye at the same upper level, thus generating locally upward buoyancy. This upward buoyancy can

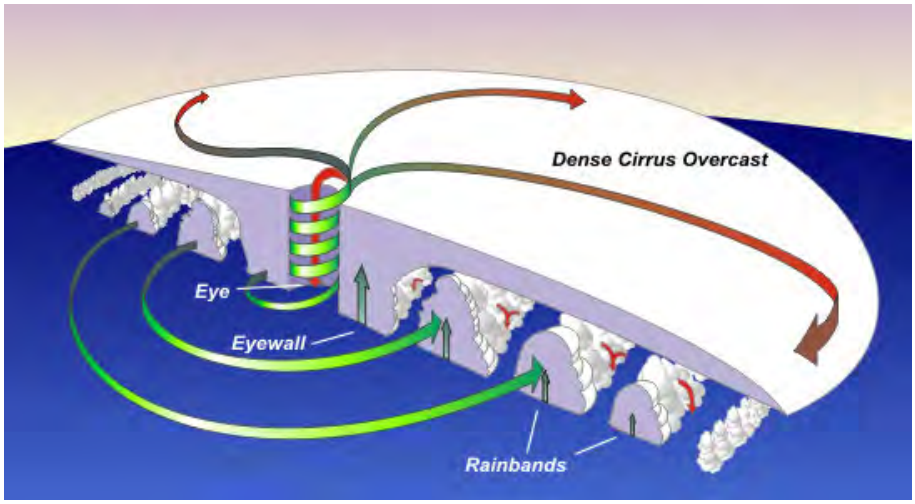

Figure 1.1: Cross section of a typical mature TC. The figure is from National Weather Service, `https://www.weather.gov/jetstream/tc_structure`.

then approximately depress the downward pressure gradient, leading to the weakening of the subsidence in the eye. The weakening of the subsidence eventually makes the eye being departed into two parts. The eye is warm and dry aloft, moist and cloudy below, with the two regions separated by an inversion layer. At the subsiding level (850 hPa-500 hPa), the center can be 10-30 K or even 100 K warmer than the eyewall[10]. Eyes are always formed for intense TCs.The median wind speed is 50 m/s for TCs with eyes, but 18 m/s for those without[11]. From the analysis of Hurricane Satellite (HURSAT) B1 infrared satellite imagery data in the period of 1982-2015, TCs with eyes seem to be much common in the Northern Hemisphere, especially over the WNP; on the other hand, TC eyes are larger in comparison, for storm systems in the Southern Hemisphere[11].

An eyewall is the location where the strongest winds, deep thunderstorms and extreme precipitations are found. Near the eyewall, the strongest winds have a rotational compo-

nent but also converge at the low levels, while divergence is found in the upper levels. Taking the structure of simulated TC Hope in 1979 as an example, shown in Fig. 1.2, the TC center is warm, dry and calm in the mid- to upper- levels. The strongest winds are found near 50 km from the vortex center (Fig. 1.2b), indicating the eyewall. Fig. 1.2b also shows that the humidity in the western part of the vortex is stronger than that in the east part, which probably due to moisture advection to the western part of the TC brought by the south westerly monsoon flow from the South China Sea (SCS). Note that stronger wind speed is found in the east part of the TC (Figs. 1.2b and c), which is the result of superposition of northwestward translation velocity onto the storm-related wind in the northeast part of the system.

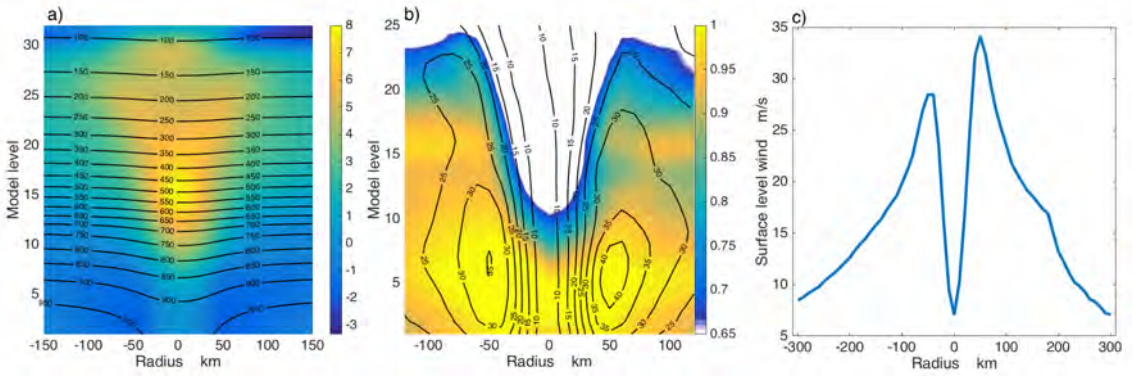

Figure 1.2: Cross section of model simulated TC Hope-like vortex in 1979. (a) The pressure-temperature profile, while shading is vertical temperature change (Units: K), and contours are pressure levels (Units: hPa); (b) The vertical relative humidity (shading) and wind speed (contours, m/s) distribution; (c) Surface wind profile.

Controlled by the rotating wind field, strong convection is shaped into long, narrow rainbands or "spiral bands". Fig. 1.3 shows the simulated spatial distribution of precipita-

tion associated with TC Hope. A long rainbands spiralling from outer region of the vortex into the center part can be seen. The outer part of the rainbands farther from the TC center is referred to as the outer rainbands, while the rainbands near radius of maximum wind speed (RMW) are referred to as the inner spiral rainbands.

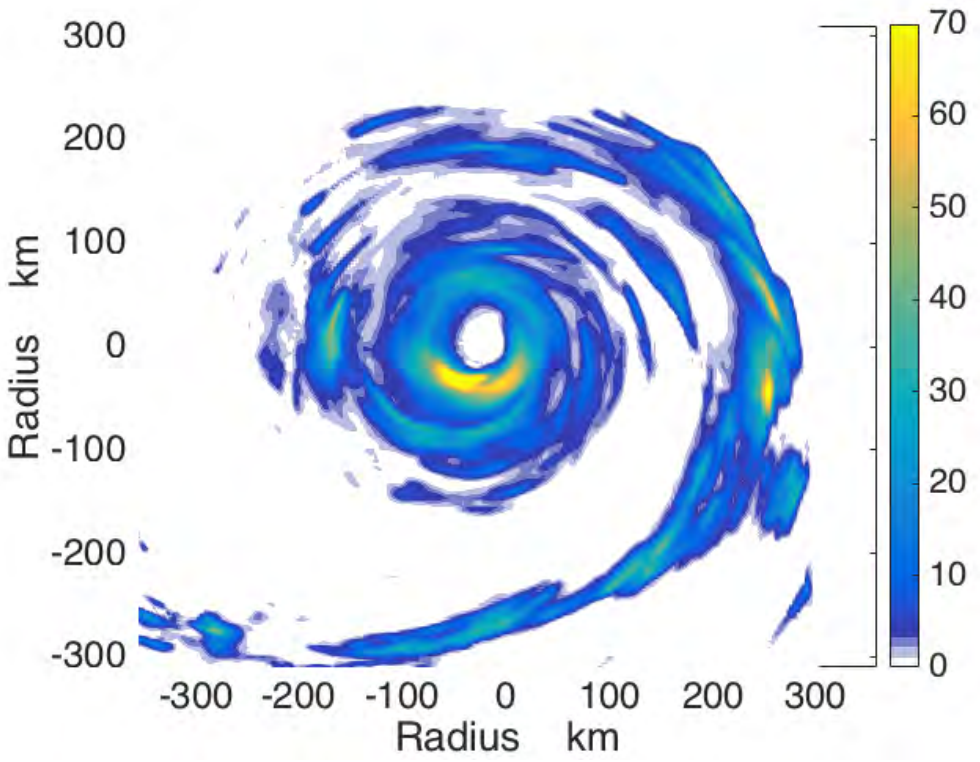

Figure 1.3: Simulated spatial distribution of precipitation of TC Hope (Units: mm/hour).

The formation process of the two types of rainbands is different. It was suggested that inner spiral rainbands are related to vortex Rossby waves[12], which is as a result of barotropic instability passing the elevated potential vorticity (PV) ring near the inside part of RMW or caused by the asymmetric convective activities near the eyewall[13, 14,

15, 16]. Sheared vortex Rossby waves may play an important role in the formation of inner spiral rainbands[12, 17, 18]. The outer spiral rainbands are mainly driven by inertia-gravity waves[19, 20], which could be triggered by deep convection in the eyewalls and some relevant instabilities[21, 22, 18, 23]. In detail, the outer rainband is suggested to be controlled by the radial wind speed and terminal velocity of ice species in the upper level of the eyewall. Model simulations show that when the snow/graupel melting and the evaporation of rain are turned off in the model, the outer spiral rainbands are largely suppressed or even disappear[24].

1.1.2 TC intensity scales

Based on the maximum sustained surface winds, TCs are classified into different intensity levels. TCs developing in different regions are ranked according to different rules. TCs in NA and ENP are issued based on the Saffir-Simpson hurricane wind scale, in which the estimated 1-minute average maximum sustained surface winds are used. In the WNP, the ESCAP/WMO Typhoon Committee applies four classifications according to the estimated maximum sustained 10-minute mean winds. Storms in the North Indian Ocean (NIO) are classified using the India Meteorological Department's scale with 7 different classifications, based on the averaged 3-minutes maximum sustained winds. TCs in the Southern Hemisphere are classified by two warning centres. The Australian TC intensity scale classifies storms in the Australian or South Pacific basin. In the South-West Indian

Ocean, Meteo France warns various French territories about TC occurrence. For classification of TCs in both basins, 10-minutes sustained wind speeds are used. In Hong Kong, TCs are classified using maximum sustaining surface wind speed based on 10-minutes averages, as shown Table. 1.1. The intensity scale in Table. 1.1 is adopted in this study.

Table 1.1: TC classification by the Hong Kong Observatory

TC classification	Max 10-min mean wind (km/h)
Tropical Depression	41 to 62
Tropical Storm	63 to 87
Severe Tropical Storm	88 to 117
Typhoon	118 to 149
Severe Typhoon	150 to 184
Super Typhoon	185 or above

1.1.3 TC genesis

In general, TCs tend to develop under some favourable environmental conditions[25]. First, to maintain a TC, the ocean surface temperature should be at least 26.5 °C and with warm water extending to at least to 50 m of depth. Second, the vertical atmosphere temperature should decrease fast with altitude, which is potentially favourable for moist convection. Third, a humid atmosphere, with high relative humidity in the mid level (around 600 hPa) that allows the development of widespread thunderstorms is needed. Fourth, strong low-level or near-surface disturbance systems with large vorticity and convergence are required. Fifth, vertical wind shear should be less than about 10 m/s thus can reduce the ventilation effect and is beneficial to the growth of TCs. Another requirement is that

genesis location should be at least 500 km far from equator, such that Coriolis force is strong enough to maintain the cyclonic flow near the low pressure system.

The above conditions, however, may not guarantee the development of disturbances into TCs. Generally, warm moist air converges at the surface of the tropical convective system and latent heat is converted into kinetic energy in the mid- to upper- levels. If such circulation can overcome the dissipating effects due to friction, it can become self-sustaining. To maintain the growth of the low pressure system, mass of the air column should be removed in the net, this is because the subsidence near the convection area will decrease the buoyancy within the clouds[10, 26], for the reason that the compressed subsiding air leads to warming and reduces the temperature gradient between the in-cloud and outside atmosphere. Removal of air mass from TC center is achieved through the upper-level outflow[27, 28]. Even if pressure begins to fall at the surface, the atmosphere could generate gravity waves and re-adjust back to the original state, unless the Rossby radius of deformation is small enough for residual circulation formation[29, 30, 31]. To summarize, the mechanisms for a tropical cloud cluster system overcoming the above limitations and developing to a TC are complex, and some are still unclear.

One of the earliest proposed theory for accounting for the development of tropical convections into TCs is called the conditional instability of the second kind (CISK)[32]. CISK can be described as the a lowering of surface pressure process through latent heating released, decreased surface pressure then leads to enhanced radial inflow and convergence,

which in turn strengthens the latent heat, and further decreases the surface pressure. The problem of the CISK theory is that the latent heating process in the tropical cloud clusters is not strong enough to form circulation in the order of Rossby radius which is large in the tropics ($\sim$1000 km). Although CISK has trouble in explaining how TCs can be formed from cloud clusters, it can be applied to explain how a TC intensifies after being formed. Since the 1990's, more recent theories have been proposed to explain the development of TCs from tropical cloud clusters, focusing on mesoscale convective vortices (MCV) which are mid-level vortices found in many cloud clusters. They are usually referred to as "Top-down Merger"[33, 34, 35, 36], "Top-down Showerhead"[37, 38] and "Bottom-up Development"[39, 40, 41, 42, 43], all of which attempt to explain how an MCV can result in the formation and amplification of a vortex system, which can then further develop into a TC.

1.1.4 Impacts of TCs on coastal regions

With extremely strong winds, heavy rainfall and storm surges, TCs can bring the most devastating natural disasters to coastal regions, threatening to human lives and inducing large economic losses [44, 45]. During the last two centuries, TCs have been responsible for the deaths of about 1.9 million people worldwide. It is estimated that 10,000 people per year died due to TC related disasters[46], with annually 740 deaths in East Asia[47], 25 in the United States[46] and 5 in Australia[48]. TCs can also cause damages inland,

through floods and landslides, sometimes hundreds of km from the coastline.

TCs can also bring heavy precipitation and may cause severe floods to the coastal areas. A global distribution of TC induced rainfall was calculated using the best-track TC datasets together with daily precipitation data from 1970 to 2014[1]. It was found that the highest TC-induced total rainfall occurs in East Asia (>400 mm/yr) and northeastern Australia (>200 mm/year), followed by the southeastern United States and along the coast of the Gulf of Mexico (100-150 mm/yr) (Fig. 1.4). TCs account for 35%-50% of the mean annual rainfall in northwestern Australia, southeastern China, the northern Philippines and south coastlines in US.

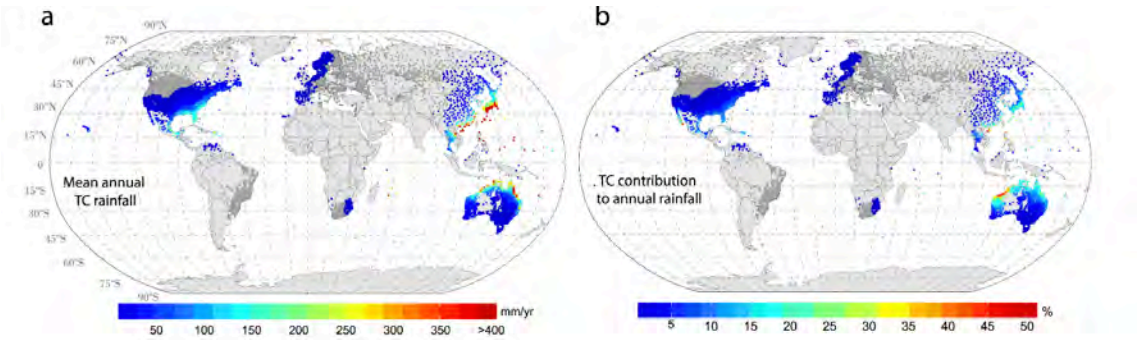

Figure 1.4: (a) Spatial distribution of the mean annual TC rainfall (mm/yr). (b) The relative contribution of TCs to the mean annual rainfall. Figure is from Villarini & Vecchi[1].

Storm surge is an abnormal rise of the water above the astronomical tide induced by the passing of TC systems. Strong TC winds can amplify the surge due to surface shear stress, and the most effective place is over shallow water along the coastal regions. Generally, storm surge height is more than 1 m globally. For example, Super Typhoon Hato in 2017 caused a maximum storm surge of 2.79 m in Zhuhai, China, while super Typhoon

Mangkhut in 2018 induced a high storm surge of 3.38 m in Hong Kong waters (Storm surge data can be checked in HKO website, https://www.hko.gov.hk/wservice/tsheet/pms/stormsurgedb_e.htm). For some extreme cases, the storm surge height can be more than 8 m[49]. Global distribution of storm surge is reviewed[50] and it was found that Bay of Bengal (BOB) in NIO sees the world's highest surge, with five surges higher than 5 m per decade on average and the storm tide magnitude reaching up to 13.7 m. Coastal locations adjunct to WNP have the highest rate of low-magnitude surges, e.g., the China coast experiences 54 surges higher than 1 m per decade, and even higher rates are found in the Philippines. The US Gulf Coast has the largest frequency of both high-magnitude (> 5 m) and low-magnitude (> 1m) surges.

China is the most populated country in the world; its coastal cites are densely populated, but also frequently hit by landfalling TCs, especially those in southeastern China[51, 52]. Situated in Southeast China, Pearl River Delta (PRD) includes Hong Kong, Macao and other highly developed megacities in the Guangdong Province, which is exposed to WNP TCs that can bring marked social and economic damages[52, 53, 54]. Destructive storm surges induced by the two deadliest typhoons caused heavy causalities in Hong Kong in 1906 and 1937, with over 10,000 people killed in each incident [55]. Typhoon Wanda, which induced 3.2 m storm surge and killed 183 people in 1962, ranked the third in the deadliest TCs in Hong Kong since 1884 [55]. Super Typhoon Hato in 2017 Mangkhut in 2018 are two recent extreme cases that hit PRD region and caused huge eco-

nomic and social losses, each of them were associated with more than 3 m of storm surge height. Benefitted from the improvement of cyclone monitoring and forecasting technique, the loss of human lives in relation to TC occurrence has decreased significantly in PRD region (see `https://www.hko.gov.hk/education/article_e.htm?title=ele_00444` for example).

Although casualties caused by TCs are decreasing, rapid urbanization and economic growth of coastal regions have increased the exposure of people and assets to TC related disasters. TC-related extreme rainfall rates are projected to increase by about 20%[56]. Combined with accelerating sea level rise (SLR)[57, 58] in the globally warmed future, there will be higher storm surges and increased flood risks to coastal areas. Therefore, understanding the impacts of climate change on land-falling TCs and their related hazards are essential and important from the scientific, societal and economic point of view.

1.2 The influence of background climate on TCs

1.2.1 TC climatology

As is discussed in Chapter 1.1.3, TCs are formed over warm oceanic locations, with weak vertical wind shear, strong low level cyclonic vorticity and away from equator. Ramsay[2] compared Northern Hemisphere TC genesis locations with climatological sea surface temperature (SST) in August, and Southern Hemisphere TC genesis locations with January

SST. It is seen from Fig. 1.5 that TC genesis locations are concentrated in some parts of warm ocean basins, namely WNP, ENP, NA, IO and SP. Each year, there are about 80 TCs formed globally, and the number has been remarkably steady since the beginning of reliable global best track records. The Northern Hemisphere accounts for 70% of the global TC number, compared to just 30% in the Southern Hemisphere. Almost one third (31%) of the global storms originate in WNP, with the ENP and NA basins accounting for 19% and 16%, respectively. The North Indian basin experiences significantly fewer cyclones, with only about 4% of the global number. Among the 30% of global TCs that develop in the Southern Hemisphere, 11% is found in the South Indian basin, 12% in the Australian region, and 7% in the South Pacific basin[2].

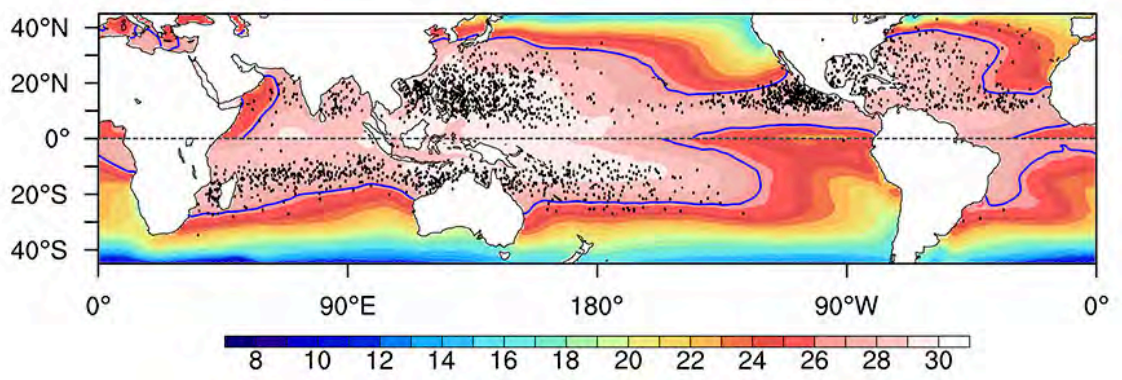

Figure 1.5: TC genesis locations for the period 1985-2014 from IBTrACS-WMO overlaid on climatological SST data for August in the Northern Hemisphere, and SST for January in the Southern Hemisphere. The 26.5°C isotherm is outlined in blue. Figure is from Ramsay[2].

1.2.2 Natural variability of TC activity

Climate variabilities strongly modulate TC activities from inter-annual to decadal time scales. El Niño- Southern Oscillation (ENSO) is one of the most important modes of natural climate variability modulating TC activities. ENSO arises from coupled ocean-atmospheric dynamics in the tropical Pacific ocean[59], and its effects on TCs can be felt in various ocean basins. The inter-annual variability of WNP TC activity is greatly affected by ENSO, inluding TC number, intensity and genesis location. A decrease of TC number in WNP was also found following an El Niño event, and it was suggested to be related to the shift of the Walker circulation[60]. The Genesis Potential Index (GPI)[61] was applied to examine the relationship between TC activities and ENSO. It was found that during El Niño years, relative humidity (RH) and vertical wind shear (VWS) are modulated, leading to a suppression of TC genesis in the Atlantic basin, while changes in RH and VWS result in eastern shift of the mean genesis location in WNP[62]. The two flavours of ENSO, namely the Eastern Pacific (EP) and Central Pacific (CP) type, also affect TC genesis frequency differently. It was found that WNP TC frequency has significant positive correlation with the El Niño Modoki index which characterises CP El Niño[63], while the Niño-3 index shows a negative (positive) correlation with TC numbers in the northern (southeastern) quadrant of WNP[64]. This is due to the low-level large-scale cyclonic anomaly formed over WNP during CP El Niño, favouring TC genesis. On the other hand, an anti-cyclonic anomaly in the subtropics and meanwhile a cyclonic anomaly near the

equatorial central Pacific are formed in EP El Niño years[63]. ENSO is also responsible for TC genesis location change, with a southeastward (northwestward) shift during El Niño (La Niña) years[64], which can be attributed to the eastward extension of the monsoon trough and westerlies together with the reduction of VWS in WNP[64, 65]. TC intensity could then be modulated during El Niño years because of the east shift of genesis region and longer sustaining time over the ocean, with stronger low level vorticity and weaker VSH[66, 67]. The passed 30 years have also seen a shift of the Pacific climate regime, during which more La Niña and CP El Niño events occurred. The decreased low-level relative vorticity and increased vertical wind shear at the WNP TC genesis locations (150-180^oE, 10-17.5^oN)[68] during this period in relation to such climate shift were suggested to be responsible for the reduction of WNP TC frequency[69]. The inter-annual relationship between TC activity and ENSO was also found to be enhanced[69]. ENSO also affects EP and Atlantic hurricanes[70, 71, 72], as well as Southern Hemisphere TCs[73, 74]. Finally, TC activity in both WNP[75] and NA[76, 77] are affected by the quasi-biennial oscillation (QBO).

Apart from the inter-seasonal and inter-annual time scales, some decadal climate modes or secular climate trends can also influence TC activities. Such climate modes or factors include North Pacific sea-ice cover variations[78], Tibetan plateau snow cover[79, 80], Pacific decadal oscillation (PDO)[81, 82] and North Pacific oscillation (NPO)[83]. Atlantic Multi-decadal Oscillation (AMO)[84] and Atlantic Meridional Mode (AMM)[85] play

important roles on NA hurricane occurrence. On the inter-seasonal timescale, Madden-Julian Oscillation (MJO), can also affect TC activities over almost all ocean basins[72, 86, 87, 88, 89].

1.2.3 More intense TCs after 1970s

How global warming might have affected TC frequency and intensity is still hotly debated[90, 91]. Based on Joint Typhoon Warning Center (JTWC) best track data, neither the global TC genesis frequency nor the number of storm days showed any trend in the last 50 years[92]. But the TC intensity during 1970-2004 did show a substantial change globally. The ratio of weak TCs has decreased, while TCs in the strongest categories (4 + 5 in Saffir-Simpson scale) have almost doubled both in number and in percentage[92]. Results based on satellite-derived TC wind speed on the lifetime-peak intensity of the strongest TCs, and the yearly lifetime maximum wind speed also showed a positive trend for the intense TCs, with stronger TCs obsereved higher increase rates[93].

Variations in WNP landfall TC characteristics were also examined through cluster analysis[3]. The landfall TC lifetime peak intensity change from the 1970s is shown in Fig. 1.6. It can be seen that the annual mean lifetime peak intensity for the landfalling TCs has increased by about 8 m/s ($\sim$15%) from 1977 to 2013. Consistently, category 4-5 typhoons have increased by nearly four times in number (from less than one per year in the late 1970s to more than four per year in recent years). The region with TC intensifi-

cation was found to coincide with local SST warming, suggesting that local ocean surface warming controls the TC intensification rate (Fig. 1.6b). However, limited historical observations mean large uncertainties and it is hard to identify responses of TCs to global warming from the inter-annual and decadal change records[56, 94, 95].It was also argued that the increase of WNP intense TC number could be just a reflection of the (natural) inter-decadal variation of TC activity[96].

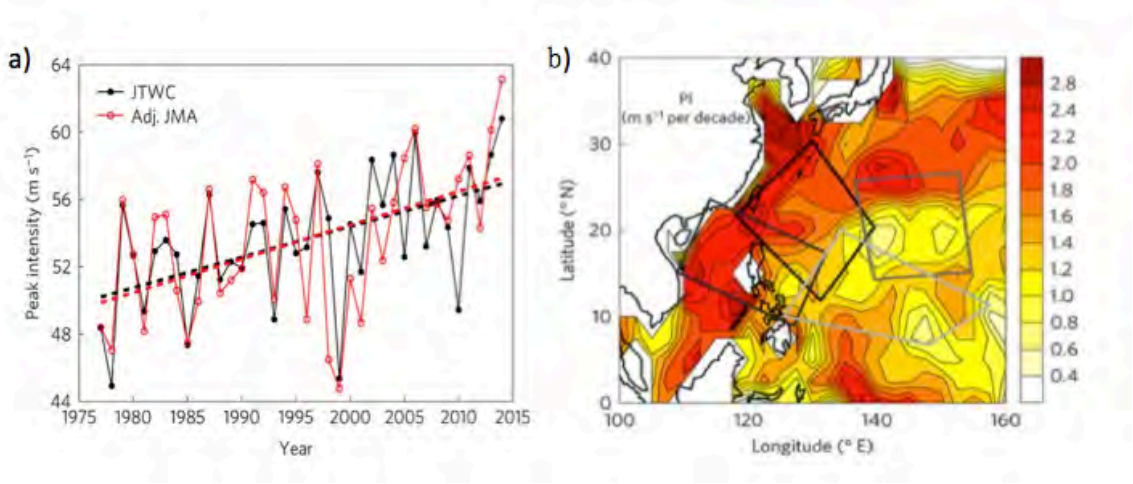

Figure 1.6: (a) The annual change of WNP landfall TC peak intensity in 1977-2013. (b) Spatial maps of linear trends in potential intensity (PI, m/s per decade). Figure is from Mei & Xie[3].

1.3 Projections of TCs from GCMs and mesoscale models

TCs are strongly influenced by SST[97, 98] and atmospheric conditions such as atmospheric stability[99, 100], vertical wind shear[101, 102] and large-scale low-level vorticity[103, 104]. Since these parameters are expected to change under global warming, the

latter will also influence WNP TCs behaviours. Combined with the projected accelerating sea level rise (SLR)[57, 58] in the warmer future, enhanced TC intensities could also lead to higher storm surges and increase flood risks to various coastal regions.

Based on projections from General Circulation Models (GCMs), it is likely that the global TC frequency will either decrease or remain the same, while their mean intensity (as measured by maximum surface wind speed) will increase by +2 to +11%, and TC rainfall by about 20% within 100 km of the cyclone center[56]. On the other hand, note that coarse resolution global models, such as those used in phase 5 of the Coupled Model Intercomparison Project (CMIP5)[105] could not reproduce very intense TCs[106, 107, 108]. Although there are global models with resolutions as high as 10 to 20 km[109, 110, 98], the resolution is still not high enough to reproduce the TC eye structure and rainfall distribution. At the same time, various downscaling techniques such as dynamical downscaling[111, 91], statistical downscaling[112] and statistical/dynamical methods[113] have been used to gain insight on the response of TCs to climate change. Knutson et al.[91] downscaled the 50 km Geophysical Fluid Dynamics Laboratory (GFDL) High Resolution Atmospheric Model (HiRAM) outputs with the GFDL Hurricane model. It was found that the 6-km GFDL Hurricane model can simulate very intense storms with a better eye structure and rainfall distribution.

1.4 Pseudo global warming technique

A new method for investigating climate change impacts on circulation systems called pseudo global warming (PGW) was introduced by Kimura and Kitoh[114], with the method first proposed by Schär[115]. In the PGW technique, the anomalous values of meteorologic variables including SST, atmospheric temperature, humidity and wind field, between current and future climates simulated by GCMs are first obtained. These perturbations will then be added to the initial and boundary conditions for an initial weather system, such that the same case can be re-simulated under a future climate background[115]. The PGW method was well used to examine the responses of snow storm[116] and Baiu rainband[117] to future global warming. It is also used in investigating changes in TC characteristics for both idealized[118] and real storms[119, 120, 121]. Using the Finite Volume Community Ocean Model (FVCOM), Nakamura ***et al.***[122] analysed the WNP TC Haiyan (2013) and its induced storm surge in future using PGW, according to four scenarios proposed by Intergovernmental Panel on Climate Change (IPCC) Fifth Assessment Report (AR5). It was found that, if only SST warming was imposed, the drop of minimum sea level pressure (SLP) would be as large as 21 hPa, with an 2.7 m increase of maximum storm surge under RCP 8.5 compared to the present climate. On the other hand, such TC intensification would be much reduced by incorporating air temperature warming. In fact, when SST, air temperature and humidity were all added, the minimum SLP decrease was only about 13 hPa and the storm surge increased by about 0.7 m. Overall, the PGW

technique proves to be useful for accessing how global warming might impact on particular weather systems, provided that similar one exists in the future under similar synoptic conditions.

1.5 Objectives and framework of the study

In this study, impacts of global warming on TCs over WNP and NA regions will be examined. Particular focus will be on the peak/landfall intensity of TCs, storm size, extreme rainfall, induced storm surges and also influences on land areas after landfall. Response of these characters to global warming will be investigated using global model outputs, and through high-resolution models using PGW technique. Datasets and methods used in this study are described in Chapter 2. Chapter 3 presents the observation results of TC character changes in the past 50 years from historical records. Future projections of TC activities are shown from Chapter 4 to 6. In particular, future WNP TC activities and their impacts on Asia inland regions are projected using 20-km MRI-AGCM3.2s model in Chapter 4; Chapter 5 displays future impacts of WNP landfalling TCs and associated storm surges on PRD region through PGW method based on 3-km resolution Weather Research and Forecasting (WRF) model and Sea, Lake, and Overland Surges from Hurricanes (SLOSH) model, while future projections of Atlantic hurricanes and the associated influences on US inland ares are proposed in Chapter 6. The conclusions, limitations and future directions of this study are discussed in Chapter 7.

Chapter 2

Methodology, models and data used

2.1 Outline of methods

In order to investigate the impacts of climate change on land-falling TCs and their associated influences on land areas, a suite of model experiments are conducted and their results anlayzed. The main parameters of concern in this study are the peak/landfall storm intensity, storm size, TC related rainfall, induced storm surge as well as storm decay processes, and their change due to global warming.

The historical change of WNP TCs peak and landfall intensities are analysed using 4 best track datasets from International Best Track Archive for Climate Stewardship (IBTrACS, see Chapter 2.3). Moreover, the TC decay process after landfall and their impacts over inland area are examined using a statistical TC decay model (see Chapter 2.2.1).

The projections of WNP TC activities under global warming conditions from the 20-

km mesh Meteorological Research Institute (MRI) atmospheric general circulation model (MRI-AGCM version 3.2s, see Chapter 2.2.2) are also evaluated, focusing on TC frequency, genesis location, intensity and impacts on East and Southeast Asia inland regions.

In the second part of this work, higher resolution numerical simulations are carried out to investigate changes of WNP landfall TCs at the end of 21st century through the PGW method. In particular, WNP TCs making landfall in PRD region are focused on. 20 historical intense landfall TCs that brought the highest storm surges to the PRD region (mostly to Hong Kong) during the last 6 decades are selected (see Chapter 2.4.1). These 20 selected TCs are simulated by the Weather Research and Forecasting (WRF) model (see Chapter 2.2.3). The response of the 20 TCs to global warming can then be inferred from the PGW experiments (Chapter 2.4.2), including TC intensity, storm size and extreme precipitation. Using Sea, Lake, and Overland Surges from Hurricanes (SLOSH, see Chapter 2.2.4) model, the changes of storm surges induced by the 20 TCs can also be projected in PRD region.

The responses of Atlantic TCs to global warming are also tested using the Geophysical Fluid Dynamics Laboratory (GFDL) regional model (ZETAC, Chapter 2.2.5). In these model experiments, a new kind of simulating method, namely vortex seeding, is introduced. Free vortices are randomly inserted to the model environment along US east coast and integrated for 8 days (see Chapter 2.2.5). The PGW technique is again applied to evaluate changes of these induced Atlantic storms under a warmer background climate

in 2075-2099 according to the RCP 8.5 scenario. Changes of landfall intensity, and the threats to east coast of US are examined.

2.2 Models

2.2.1 Statistical TC decay model

As described by Kaplan and Demparia[123], the decay rate of a TC is proportional to its maximum surface wind speed over the land, and can be expressed as below,

$$\frac{dv}{dt} = -kv \tag{2.1}$$

where v is TC's surface wind, k being the decay constant and t is the time after landfall. The solution of Eq. 2.1 is given by

$$v(t) = v_0 e^{-kt} \tag{2.2}$$

where v_0 is the landfall surface wind speed of the TC. However, TC intensity usually does not drop to zero, but to a background wind speed V_b. A possible physical interpretation of the background wind V_b is the lowest number of maximum sustained surface wind (MSSW) that a TC can be maintained over land under some idealized conditions[124].

Let $v = V - V_b$, where V is the observed MSSW, and using Eq. 2.2, we get

$$V(t) = (V_0 - V_b)e^{-kt} + V_b \tag{2.3}$$

where V_0 is the observed MSSW at landfall. Given the observed $V(t)$ change and the background wind, the decay constant k could be found by curve fitting. The observed $V(t)$ can be obtained from IBTrACS (see Chapter 2.3); however, there is no straightforward way to obtain the background wind speed. One way to obtain background wind is to use re-analysis data. But the background wind can be different for different TCs, which makes it difficult to derive the exact background wind speed from re-analysis datasets. In this study, TC's background wind speed is suggested to be between 0 and the weakest MSSW in the best track data, and the exact value can be determined by the best fitting of the TC decay process to an exponential curve.

For a particular TC decay process, given the range of background wind speed discussed above, the background wind speed V_b, landfall intensity V_0 and the scaling factor k in Eq. 2.3 can be fitted by least square method. Fig. 2.1 shows a well fitted case (TC Agnes in 1984) after landfall using the exponential decay model. The decay process and background wind speed, as well as the landfall intensity, are well estimated using the empirical model.

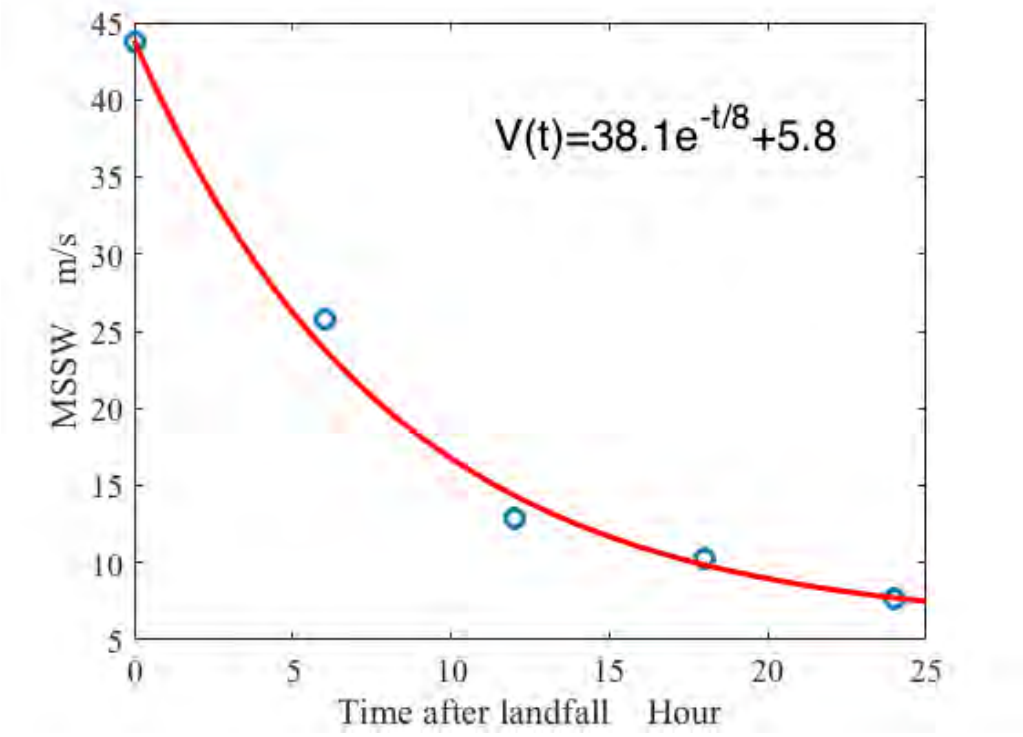

Figure 2.1: Observed (blue circle) and fitted (red line) MSSW (Units: m/s) decay process of TC Agnes in 1984.

Moreover, the sustaining time after landfall can be calculated based on Eq. 2.3,

$$T_v = \tau(ln(V_0 - V_b) - ln(V - V_b)) \tag{2.4}$$

where τ is time scale of the decay process and $\tau = 1/k$, and V is the surface wind speed

at the time T_v. The potential dissipation index can also be obtained,

$$\begin{aligned} PDI_v &= \int_0^{t(V)} V^3 dt \\ &= \frac{1}{3}\tau[(V_0 - V_b)^3 - (V - V_b)^3] + \tau V_b^3 ln\frac{V_0 - V_b}{V - V_b} \\ &+ \frac{3}{2}\tau V_b[(V_0 - V_b)^2 - (V - V_b)^2] + 3\tau V_b^2(V_0 - V) \end{aligned} \tag{2.5}$$

Uncertainties can be introduced in observation of TC's MSSW when the TC is too weak. In order to obtain more robust results from the best track datasets, this study just concerns the decay period from landfall to the time when the TC is no longer classified as a tropical storm ($V \geq 17m/s$). As such, the total sustaining time over the land can be calculated as,

$$T_l = \tau(ln(V_0 - V_b) - ln(17 - V_b)) \tag{2.6}$$

where T_l means sustaining time over land (Units: hour), while the units of both wind speeds and the value of 17 is in m/s. The PDI to the land area is,

$$\begin{aligned} PDI_l &= \frac{1}{3}\tau[(V_0 - V_b)^3 - (17 - V_b)^3] + \tau V_b^3 ln\frac{V_0 - V_b}{17 - V_b} \\ &+ \frac{3}{2}\tau V_b[(V_0 - V_b)^2 - (17 - V_b)^2] + 3\tau V_b^2(V_0 - 17) \end{aligned} \tag{2.7}$$

and PDI_l represents PDI releasing to land areas (Units: m^3/s^2).

Thus for any historical TC, given the observed decay process $V(t)$, the sustaining time and PDI over the land after landfall can be easily calculated by Eq. 2.6 and Eq. 2.7.

2.2.2 MRI-AGCM3.2S model

The MRI-AGCM versions 3.2S was developed as the atmospheric component of MRI Earth System model version 1(MRI-ESM1)[125], based on a very slightly earlier version (MRI-AGCM3.1), with resolution of about 20-km[126]. The dynamical core of MRI-AGCM3.2S is the hydrostatic primitive equations using a spectral transform method of spherical harmonics[127] at the TL959 resolution (20×20 km), with 64 unevenly-spaced vertical levels up to 1 Pa. The cumulus convection is parameterized by the Yoshimura cumulus scheme[125], and the radiation scheme is the same as that used in the JMA operational model[128], while the respective planetary boundary layer and land surface physics are represented by the Mellor and Yamada scheme[129] and the improved Simple Biosphere model[130]. More details about the model physics such as cloud physics and aerosols can be found in Mizuta's paper[131]. To examine the impacts of anthropogenic warming on climate, a pair of historical and future warming AMIP-type experiments are conducted. In the historical run, MRI-AGCM3.2S model is driven by monthly-mean SST and sea-ice concentration HadISST1 data[132], along with monthly climatology of sea ice thickness from from Bourke and Garrett[133], integrated from 1979 to 2003. For the future experiment, the difference between averaged SST projected by 18 CMIP3 models for the 2075-2099 period and 1979-2003 under the Special Report on Emissions Scenarios (SRES) A1B scenario is first calculated. The boundary SST forcing for the future experiment is then derived by superposing the obtained SST difference to the observed SST used

in the historical experiment.

2.2.3 WRF model

The model used to simulate the 20 selected TCs making landfall over the PRD area is the Advanced Research WRF (WRF-ARW) dynamical core (version 3.7,[134]), with doubly nested domains of 15- and 3-km resolution in horizontal respectively, and 45 layers in vertical from surface up to 10 hPa for both. The high spatial resolution in the daughter domain (3 km) is adopted, so as to better capture TC features such as the structure of the eyewall and rain bands[135]. The physics schemes used in WRF are as follows. Dudhia Shortwave Scheme[136] and RRTM longwave[137] are used for the radiative transfer physics, and Eta (Ferrier) microphysics scheme[138] is applied for the nucleation of cloud droplets, while Kain-Fritsch convective parameterization[139] is in use for cumulus parameterization. For the Planetary Boundary Layer (PBL) Physics, Yonsei University (YSU) Scheme[140] is applied, while for the land surface and surface layer schemes, Unified Noah Land Surface Model[141] and revised MM5 Scheme[142] are employed. More about WRF physics schemes can be found in `http://www2.mmm.ucar.edu/wrf/users/phys_references.html#SL`.

The initial and boundary conditions to simulate the TC cases are obtained from European Centre for Medium-Range Weather Forecasts (ECMWF) datasets. The mainly used data in this study is from ERA-Interim reanalysis data, while TC cases before 1979 are

driven by ERA 20C reanalysis data. The descriptions of the two datasets can be found in Chapter 2.3. It should be noted that these two datasets are not the same. For example, the two datasets may have different abilities in reproducing TCs' steering flow. Such kind of discontinuity, however, does not affect the sensitivity tests on TC responding to global warming, because for only specific TC, the initial and boundary data are from the same dataset for both PGW and historical experiments.

Domain size sensitivity was also tested before carrying out the whole set of TC simulations. As shown in Fig. 2.2, two domains in different sizes are tested for 4 TC cases, whose names can be seen in Fig. 2.3. Compared to the HKO best track data (see Chapter 2.3), there is no obvious improvement when using the larger domain in terms of track (see Fig. 2.3(a)) and minimum SLP (see Fig. 2.3(b)). Hence the smaller domain in Fig. 2.2(a) is chosen for all the numerical experiments. It is noteworthy that the daughter domain might differ a little in different TC cases, because it needs to be adjusted in order to cover different TC tracks for different cases.

To ensure TC tracks in the model being reasonably close to observations, model U- and V- winds above 500 hPa were spectrally nudged with wavelength of about 1200 km towards their reanalysis values. This serves to provide a realistic steering flow to TCs in the model environment, while minimising the effect of nudging on storm-scale circulations.

In general, each TC case is integrated for more than 96 hours, and at least 72 hours before landfall. In order to obtain a more realistic and accurate TC intensity and location

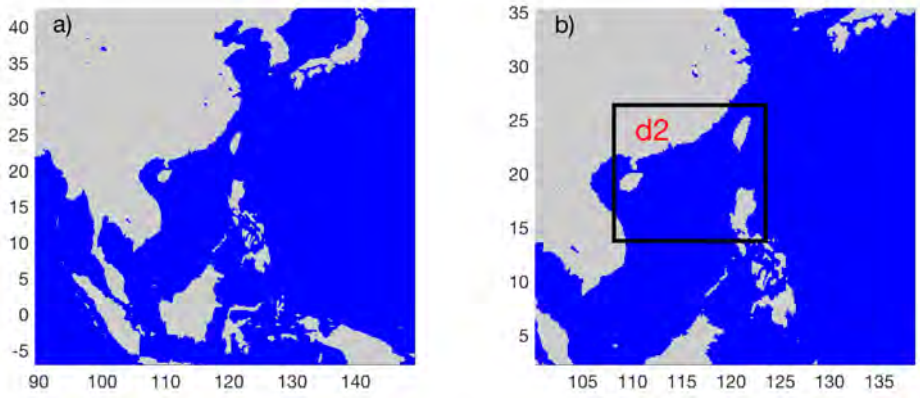

Figure 2.2: Two selected domains for WRF simulation test. (a) Larger domain; (b) Smaller domain.

in the initial condition, Rankine vortices are employed in the initial data based on the real TC intensity and location (from the HKO best track data) through the WRF bogus scheme. Description of the Rankine vortex can be found in Appendix A. WRF outputs of meteorological conditions on 3-hourly (for parent domain) and hourly (for daughter domain) basis are archived for the 20 cases, so as to determine the TC tracks, intensity, winds and related precipitation rates.

After the historical runs, the warming signals are then incorporated to the 20 TCs' initial and boundary conditions through the PGW technique (see Chapter 2.4.2). The 20 TCs are then re-simulated by WRF with the same experiment settings as those in the historical runs. By comparing results between historical and PGW runs, the impacts of global warming on the TCs can be analysed.

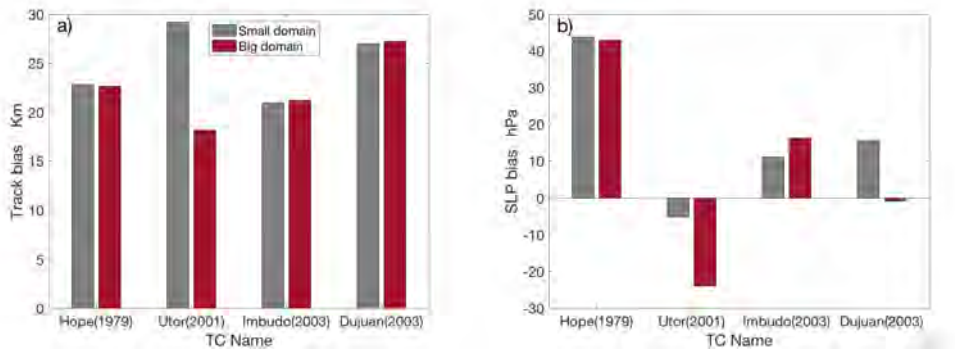

Figure 2.3: Comparison of the simulated (a) track bias, the root mean square compared to the HKO observed and (b) SLP bias, the difference of lifetime lowest TC centre SLP to the HKO observed, between the larger and the smaller domain.

2.2.4 SLOSH model

The SLOSH model, developed by the National Oceanic and Atmospheric Administration (NOAA) of US[143, 144], has been used by the HKO to support its TC warning operation since 1994. The equations of the model are based on the shallow water system.

$$\begin{cases} \frac{\partial U}{\partial t} = -g(D+h)[B_r\frac{\partial(h-h_0)}{\partial x} - B_i\frac{\partial(h-h_0)}{\partial y}] + f(A_rV + A_iU) + C_rx_\tau - C_iy_\tau \\ \frac{\partial V}{\partial t} = -g(D+h)[B_r\frac{\partial(h-h_0)}{\partial y} + B_i\frac{\partial(h-h_0)}{\partial x}] - f(A_rU + A_iV) + C_ry_\tau - C_ix_\tau \\ \frac{\partial h}{\partial t} = -\frac{\partial U}{\partial x} - \frac{\partial V}{\partial y} \end{cases} \tag{2.8}$$

where U and V are the components of transportation; g is the gravitational constant; D is the depth of the quiescent water relative to a common datum; h and h_0 are the real height of water and hydrostatic water height above datum; f is Coriolis parameter; x_τ and y_τ are

the components of surface stress; while A_r,...,C_i are the bottom stress terms.

Eq. 2.8 was developed by Platzman[145] and modified with a bottom slip coefficient by Jelesnianski[146]. The bottom stress terms are functions of the total depth, which are different from other studies, saying in the Manning or Chezy type[147]. Advective terms are not considered in Eq. 2.8[148]. The parameterization of model coefficients, such as the viscosity, drag coefficients, and bottom stress terms can be found in the NOAA Technical Report[149].

The model operates on a polar grid when solving Eq. 2.8. The surface stress and surface winds in SLOSH are parameterized with a pressure-wind relationship, using the positions of the TCs, the corresponding values of central minimum pressure and RMW. As seen in Fig. 2.4a, the grid size ranges from 1 km near the centre around Hong Kong and increases to about 7 km in the open sea. When integrating the storm surges, the TC tracks, central SLP and RMW are inputted 6-hourly from 48 hours before to 24 hours after the time of closest approach to Hong Kong.

2.2.5 GFDL regional model (ZETAC)

ZETAC is a non-hydrostatic and compressible regional model developed by GFDL. It is integrated on a C-grid with leap-frog time stepping for advection and physics, and a split-explicit adjustment time stepping for acoustic-gravity waves[150]. Physical parameterization schemes used in this model was fully described by Garner[151], as well as

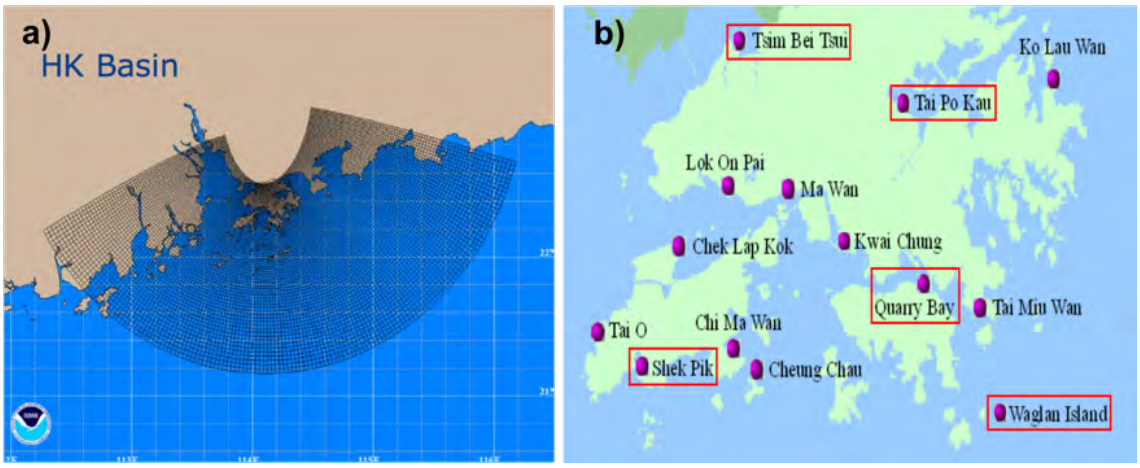

Figure 2.4: (a) Integration domain for SLOSH; (b) Locations of the 5 tide stations considered in this study in (red rectangle). North point station is not remarked in this map, whose location is in the left of and very close to Quarry Bay station.

Frierson ***et al***[152]. The model resolution is about 6 km in horizontal, with 44 levels in vertical. The vertical grid is stretched so that the spacing between levels increases from 50m at the bottom to 500m at the top of the domain ($\sim$50 hPa).

The domain in use can be found in Fig. 2.5, with coverage over a large America land area starting from eastern edge of the Rocky Mountains and also reaching Canada to the north, so as to make sure that the full decay of TCs in the simulations can be covered after landfall. The open ocean area is also large enough for full development of the seeded storms before landfall .

In order to investigate the decay process of Atlantic landfall TCs and their responses to global warming, a series of vortices are seeded and simulated near southeastern US coastline. The Rainkine vortex insertion technique is described in Appendix A, while the initial and boundary data are from National Centers for Environmental Prediction-

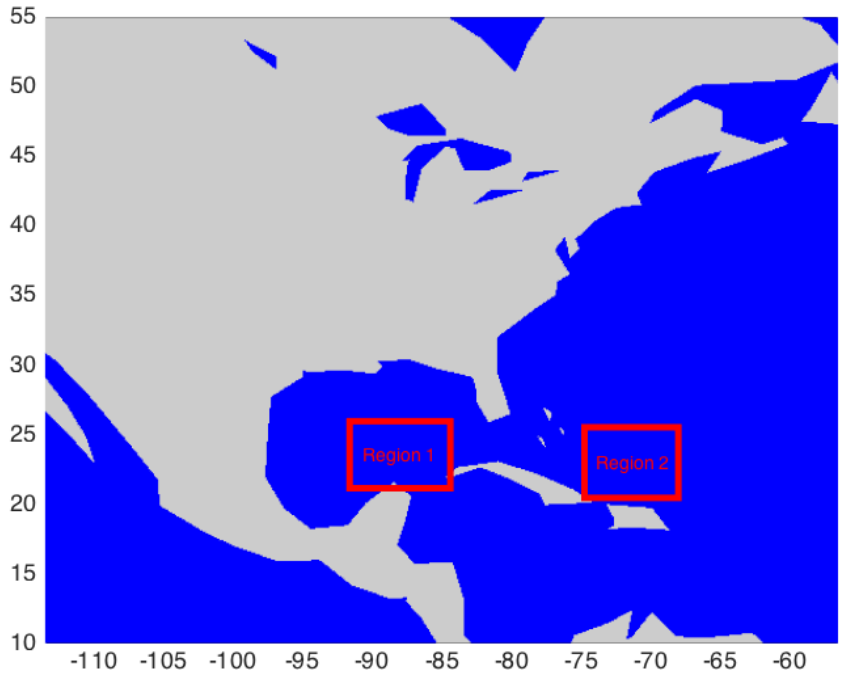

Figure 2.5: Integration domain of ZETAC. Vortex seeding is carried out in the two red regions in Gulf of Mexico and Caribbean Sea.

Department of Environment (NCEP-DOE) reanalysis 2 (see Chapter 2.3). The seeding locations are based on observed genesis clusters of Atlantic TCs making landfall over the US east coast. Kossin ***et al.***[4] analysed the modulation of climate on Atlantic hurricanes and found those made landfall are mainly generated at Gulf of Mexico and Caribbean Sea (see cluster 2 in Fig. 2.6). Based the analysed results, two regions, Gulf of Mexico and Caribbean Sea, are selected. To improve simulation efficiency, two vortices are inserted

into the two concerned regions at the same time. The distance between the two inserted vortices is farther than 1000 km to reduce the interaction between them. The initial dates for the vortices are randomly chosen from 1980 to 2016 in the TC season of August to October. However, to improve the landfall frequency of the inserted vortices, the 4-days mean steering flow for the inserted vortices have to be in the in-shore direction. Thus, the initial dates are selected only when the steering V- wind (mean of 800-600 hPa) in Gulf of Mexico is larger than 1 m/s, and at the same time the steering U- wind is less than -3 m/s. Also, the steering V- wind is larger than 1 m/s in Caribbean sea. There are more than 300 initial dates that satisfy the steering conditions. 30 of them are randomly chosen as initial conditions and 2 vortices are seeded. These 60 inserted systems, with 30 of them in Mexico Gulf and 30 in Caribbean sea, are then integrated by 8 days in ZETAC model.

After successfully simulating the 60 TCs in the historical runs, PGW is then applied to the same cases. Comparing the decay processes in the PGW experiments and those in the historical runs, the impacts of global warming on TCs after landfall can be investigated.

2.3 Observations and Earth System models data

IBTrACS

The International Best Track Archive for Climate Stewardship (IBTrACS) dataset provides a collection of currently available best track data from agencies worldwide[153], including all available Regional Specialized Meteorological Centers (RSMCs), as well as

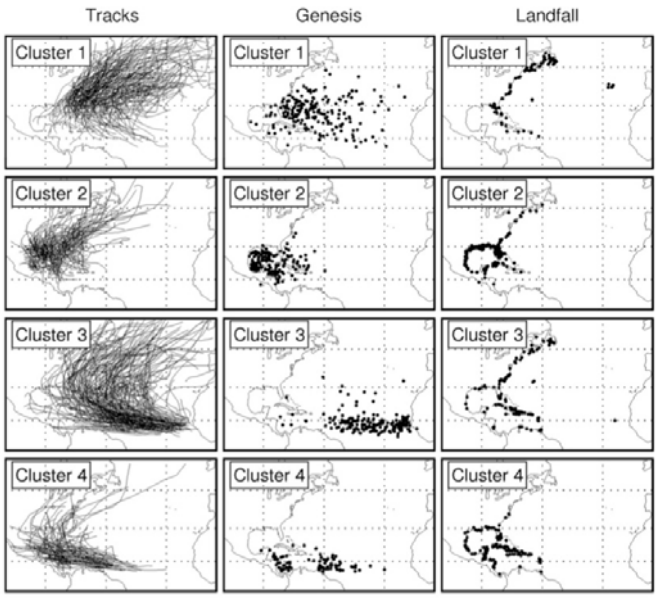

Figure 2.6: North Atlantic tropical storm and hurricane tracks, genesis locations, and landfall locations during the period 1950-2007, as separated by the cluster analysis. Figure from Kossin ***et al.***[4].

the US Department of Defense Joint Typhoon Warning Center (JTWC), the China Meteorological Administration's Shanghai Typhoon Institute (CMA/STI) and the HKO. Each agency in IBTrACS project forecasts and monitors storms for a specific region and annually archives best-track data, which consist of information on a storm's position, intensity and other related parameters. However, different agencies use different ways to estimate TC's position and intensity. For example, there is an inherent difference in the definition of maximum sustained wind between various agencies. According to WMO[154], the maximum sustained wind (MSW) is the 10-min average wind speed at 10-m height above ground level. However, the JTWC uses the 1-min average, and the CMA uses 2-min average. To combine and compare the best track data from different datasets, MSW values are

converted to a 10-min period in IBTrACS[153]. In the mean time, IBTrACS also provides original data from different agencies.

ECMWF datasets

The initial and boundary conditions for simulating the 20 selected TC cases in Chapter 2.2.3 are obtained from the European Centre for Medium-Range Weather Forecasts (ECMWF) datasets. The mainly used data are the ERA-Interim reanalysis data[155], whose spatial resolution is approximately 80 km (T255 spectral) with 60 levels in the vertical, from 1979 continuously up to the present. For TC cases before 1979, the ERA 20C reanalysis data are used[156]. The time coverage is from 1900 to 2010, and the horizontal resolution with an approximately 125 km (spectral truncation T159) with 37 pressure levels. Both EAR-interim and ERA-20C data are in 6-hourly.

NCEP-DOE Reanalysis-2 data

The National Centers for Environmental Prediction-Department of Energy (NCEP-DOE) Atmospheric Model Intercomparison Project (AMIP)-II Reanalysis project is an improved version of NCEP-National Center for Atmospheric Research (NCAR) reanalysis 1 (R-1) data. R-1 data are derived from a state-of-the-art analysis/forecast system to perform data assimilation (DA) using past data from 1948 to the present involving the recovery of land surface, ship, rawinsonde, pibal, aircraft, satellite, and other data. The model in use was identical to the NCEP global operational model in T62 resolution (about 210 km) with 28 vertical levels, based on one-way coupled ocean model 4D assimila-

tion[157]. Spectral statistical interpolation analysis and other parameter average methods were also applied for data assimilation. The model used for R-2 data was the same with R-1 data but some errors were fixed. The output of R2 data are 4 times daily from 1979 continuously to the present.

JRA-55

The Japanese 55-year Reanalysis (JRA-55) project carried out by the Japan Meteorological Agency (JMA) uses a sophisticated constant state-of-the-art DA system to provide high-quality climate data from 1958, with continuous update 4 times daily. The DA system is based on the operational system as of December 2009, whose spatial resolution was TL319 (60 km) with 60 vertical layers up to 0.1 hPa[158, 159].

COBE-SST

The centennial in-situ observation-based estimates SST (COBE-SST) is a spatially complete, interpolated $1^o \times 1^o$ SST product from 1891 to the present. It combines SST from International Comprehensive Ocean-Atmosphere Data Set (ICOADS) release 2.0, the Japanese Kobe collection, and reports from ships and buoys[160]. It is also used as input for JRA-55.

2.4 Methods in modelling

2.4.1 Selection of 20 intense TCs affecting PRD

In order to investigate the response of WNP landfall TCs to global warming, 20 intense historical TCs that brought the highest storm surges to the PRD region (mostly to Hong Kong) are selected. The names and years of the selected TCs are listed in Table 2.1, and their tracks based on the HKO data are shown in Fig. 2.7. All 20 TCs are of the Typhoon class or above. For instance, Super Typhoon Hope in 1979, with minimum SLP as low as 900 hPa and maximum wind speed of 240 km/h at the peak time, brought a maximum storm surge of 3.23m above astronomical tide at Tai Po Kou. Super Typhoon Hato's peak intensity was 185 km/h, and it caused 2.42m storm surge height at Tsim Bei Tsui in 2017. More storm surge data can be found at `https://www.hko.gov.hk/wservice/tsheet/pms/stormsurgedb_e.htm`.

Table 2.1: 20 selected TCs for WRF simulations.

Year	1962	1964	1965	1968	1973	1974	1979	1983	1989	1993
Name	Wanda	Ida	Freda	Shirley	Dot	Bess	Hope	Ellen	Gordon	Koryn
Year	1993	1997	1999	2001	2003	2003	2008	2009	2009	2017
Name	Becky	Victor	Sam	Utor	Imbudo	Dujuan	Hagupit	Molave	Koppu	Hato

2.4.2 PGW method

The PGW method is applied to model experiments by the WRF and the ZETAC model. Slightly different ways of using PGW are adopted due to the different experiment designs

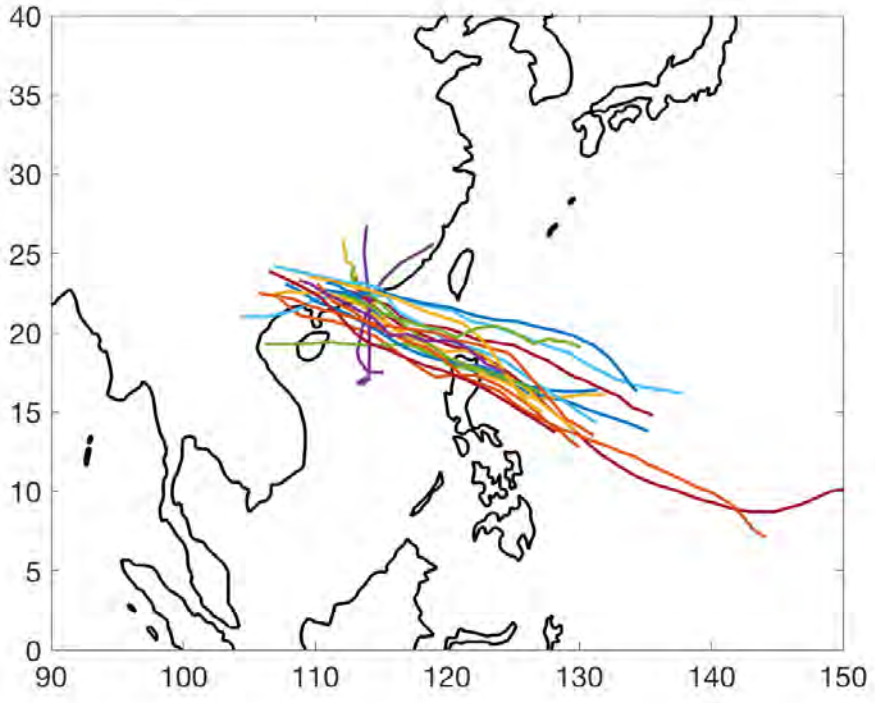

Figure 2.7: Trajectories of the 20 selected historical TCs making landfall in PRD region.

when using these two models.

PGW in the WRF-simulated experiments

In order to test the response of the 20 TCs to anthropogenic warming, anomalies of projected monthly averaged SST, vertical atmospheric temperature and humidity in the 2075-2099 period, relative to those for the historical climate in 1975-1999 based on the ensemble-mean future projections from 31 CMIP5 models[105] according to RCP 8.5 scenario, are superimposed onto the 20 selected historical experiments' initial and boundary conditions. Details of the 31 CMIP5 models are listed in Appendix B. The change of the

three factors in 2075-2099, relative to the period of 1975-1999 in August based on RCP 8.5 scenario are shown in Fig. 2.8. In this study, the change of the wind field is not added to the model environments due to reasons below. (1) The wind field near South China Sea and western part of WNP is not projected to change much in the future climate-it is because the circulation change is much more variable in the CMIP5 projections, while the other two factors changes, namely temperature and humidity, are always the most robust. Therefore, it should be mentioned that the MME average may not sample the full range of possible circulation change signals due to global warming. As seen in Fig. 2.8(b), the surface wind in WNP in the warmer future (2075-2099) is only projected to decrease by $\sim$0.5 m/s compared to the present period (1975-1999). The vertical wind shear over WNP may remain steady or decrease slightly within 1 m/s. Based on the results from Fig. 5.8(a), 1 m/s decrease of vertical wind shear corresponds to only $\sim$0.2 m/s change of peak intensity's intensification in the PGW experiments, indicating such veritical vertical wind shear change may not affect the TC intensity in the warmer future. (3) Storm surge is very sensitive to TC tracks, which can be largely affected by change of background wind field. Practically the same TCs tracks are expected to be reproduced in the future climate. In this way, how global warming might modulate TCs can be inferred.

Some adjustments should be done for when adding "warming" anomalies in the model environment inputs before pseudo global warming is applied. This is because: (1) Different global models have different abilities in simulating various aspects of the condition,

for example, some models can simulate humidity flux transportation better than others. When the 31 models average is done, imbalance in the anomalous fields might be introduced to WRF. (2) Global models and WRF are different in both resolution and physics parameterizations, and there might be a systematic bias or difference between GCMs and WRF. (3) The response of different TCs to global warming might be different due to their different background circulations. Spin up time is needed to merge the added anomalies with the specific background flow environment.

The pre-pseudo global warming adjustment is used as a way to calculate a new set of adjusted anomalies for the 3 concerned variables (SST, vertical air temperature and humidity profile). For every specific TC case, two sets of 11-day WRF integrations, control run and pre-pseudo global warming run, are conducted starting from four days before the initial time in the previous historical runs. The spin up time is chosen because it takes about four days for the boundary layer humidity to reach steady static, after adding the anomalies for most TC cases. Taking TC Hato (2017) as an example (see Fig. 2.9a), although the vertical air temperature remains very steady (Fig. 2.9b), the specific humidity experiences a sharp drop during the first 50 hours at the top of the boundary layer at around 2 km of height, and the decrease gradually vanishes after around t=100 hours. Here the model settings are the same as the historical runs, except that nudging and bogus are not need in these pre-PGW simulations. It should be noted that CO_2 concentration is also changed to 820 ppm based on the RCP8.5 scenario, in order to simulate a more reasonable

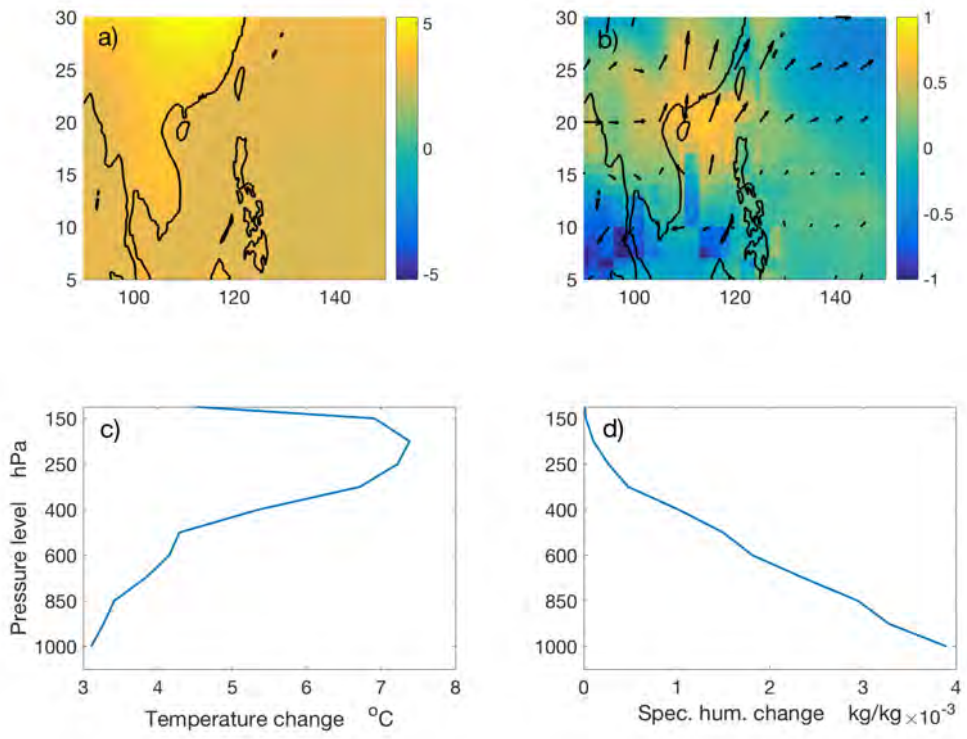

Figure 2.8: The monthly mean anomalies in 2075-2099 period compared to 1975-1999 in August based on 31 CMIP models average according to the RCP 8.5 scenario. (a) surface temperature (Units: K); (b) 1000 hPa wind field (Units: m/s); (c) Vertical temperature (Units: K) and (d) Specific humidity (Units: kg/kg).

radiative transfer in the warmer future. For the last 7 days of the WRF simulations, SST, air temperature and humidity outputs are temporally averaged. By subtracting the corresponding control run values from the temporally averaged variables in pre-pseudo global warming runs, the adjusted anomalies can be obtained and used in the PGW experiments.

PGW experiments in ZETAC model

PGW experiments based on the ZETAC model are conducted to evaluate the responses

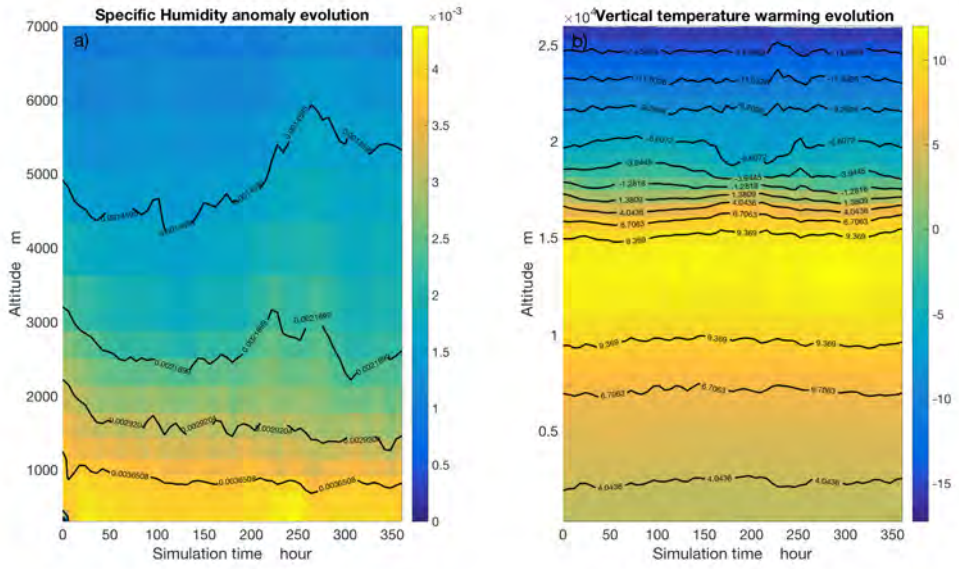

Figure 2.9: Evolution of the added (a) humidity anomaly (Units: kg/kg) and (b) warm temperature (Units: K) in domain horizontal-average.

of Atlantic landfall hurricanes to global warming (Chapter 6). The anomalous fields are computed based on the linear trend of 100-year monthly averaged SST, vertical atmospheric temperature, humidity and wind field in 1999-2099 GFDL-CM4 simulations[161], which are then incorporated to the ZETAC initial and boundary conditions based on the averaged future projections from GFDL-CM4 data[161]. PGW experiments are compared with the historical runs, and the impacts of global warming on Atlantic landfall hurricanes can be inferred.

Chapter 3

Recent variations of WNP TC landfall intensity and impacts on land area

3.1 Data evaluation and TC selection

In this chapter, changes of WNP intensities from 1970 to 2016 are examined. We focus on WNP landfall TCs making landfall from 10^o N to 30^o N, as shown in Fig. 3.4a, in order to exclude extratropical cyclones. The landfall processes in East Asia are considered, but not those in Taiwan and the Philippines, for the reason that TCs making landfall in these islands will return back to the ocean. Also, only intense TCs whose peak intensities reaching Typhoon class or above (>34 m/s in MSSW) are considered, following previous works[3].

IBTrACS uses 10-min sustained surface wind as TC's intensity, according to WMO

standard[153]. However, when the 10-min maximum surface wind was employed, the annual number of the landfalling TCs that can pass the criteria are quite few, about 3-4 TCs a year, and there was even no TC passing the limitations in some specific years, for example, the year of 1978 in HKO best track dataset (see Fig. 3.1). In order to obtain more qualified TCs, the 10-min surface wind is changed to 1-min mean using the suggested relation $V_{10} = 0.88 \times V_1$[153], where V_{10} is the 10-min surface wind and V_1 is in 1-min. After readjusting wind speed, the annual landfalling intense TC number increased to $\sim$5 (see red lines in Fig. 3.1). Overall, there are 4-6 intense landfalling TCs every year (Fig. 3.2). And the landfall frequency was steady since 1970. The landfall place, calculated by annual mean of landfall latitude and longitude, showed a decadal change in the past few decades, while there is no obvious trend for the change of the landfall location (see Fig. 3.3). Based on above analysis, 1-min average maximum surface wind is used as TC intensity.

Two datasets are considered, namely JTWC and HKO best track data from IBtrACS (see Chapter 2.3). The annual mean landfall intensity variations are displayed in Fig. 3.4b. It is seen that TC landfall intensity can be decomposed into a low-frequency component with an increase trend (see the 10-year moving average), and another high-frequency component with obvious inter-annual variability. The inter-annual variability and long-term change of the landfall intensity will be further discussed in Sections 3.2 and 3.3, and the impacts of the increasing landfall intensity on East Asia land area will be analysed in

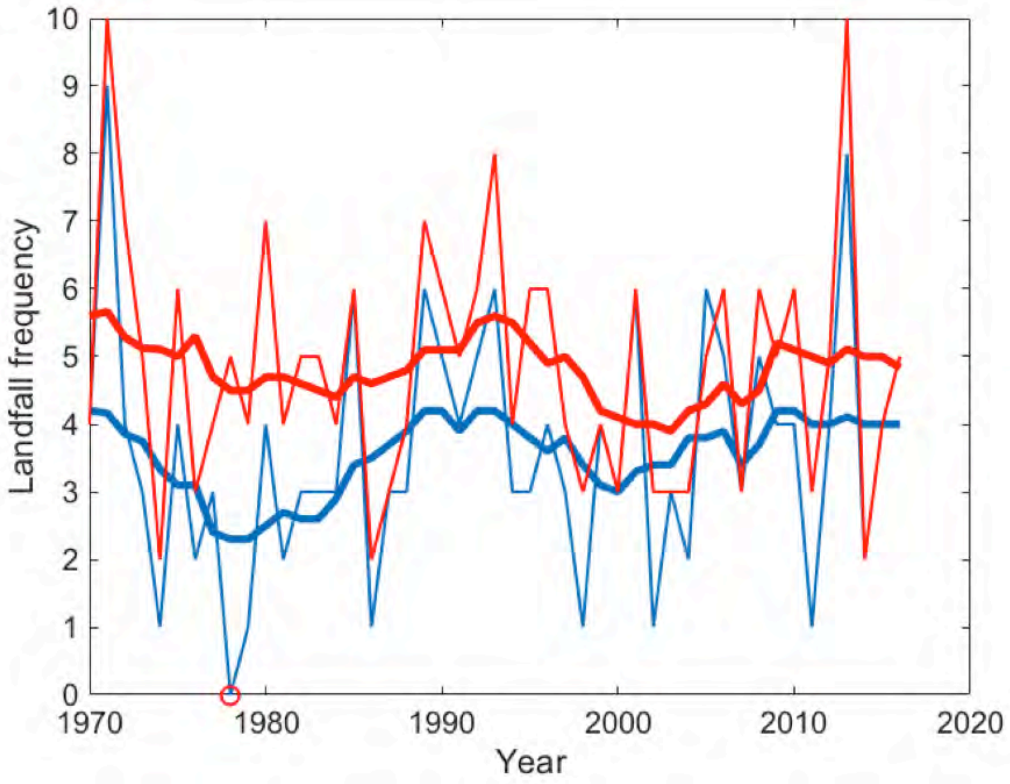

Figure 3.1: Comparison of landfall frequency (Units: year^{-1}) between the criteria in using of 10-min (Blue line) and 1-min average surface wind(Red line) in HKO best track data. The thick lines in the same colors are the changes in 10-year moving average. The red circle shows the year without qualified landfalling TC.

section 3.4 and 3.5.

3.2 Inter-annual variation of WNP TC landfall intensity

The inter-annual TC activity is known to be strongly infulenced by various climate modes on the inter-annual timescale, such as ENSO[63]. To test the response of the landfall intensity to inter-annual oceanic changes, the inter-annual landfall intensity (see Fig. 3.4b,

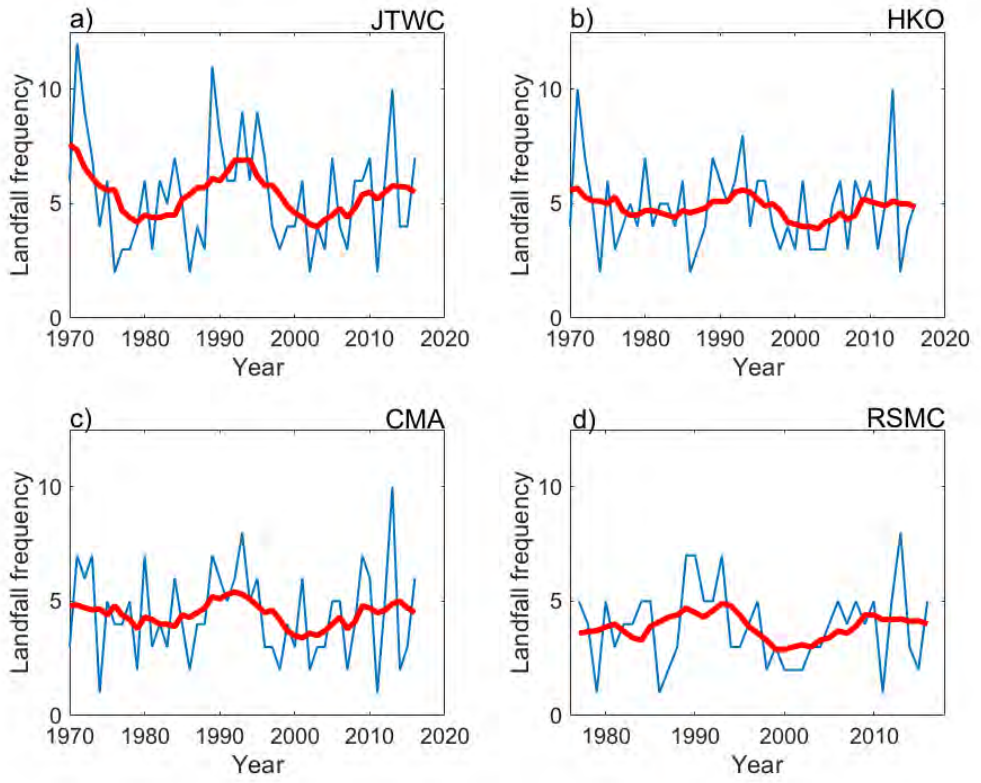

Figure 3.2: Landfall frequency of the selected TCs (Units: year^{-1}) in (a) JTWC; (b) HKO; (c) CMA and (d) RSMC. Red thick lines represent the changes in 10-years moving average.

defined as total with the long-term variation subtracted) is correlated with the Pacific SST based on the 1970-2015 COBE SST dataset, for the MJJASO season. Results are shown in Fig 3.5. It is striking that the correlation maps based on both HKO and JTWC data give a pattern that strongly resemble that associated with CP El Niño.

To further examine the relation between CP El Niño and the inter-annual TC landfall intensity, the MJJASO values of the El Niño Modoki index (EMI) are compared with the later. It can be seen from Fig. 3.6 that, indeed, CP El Niño activity in the TC season is

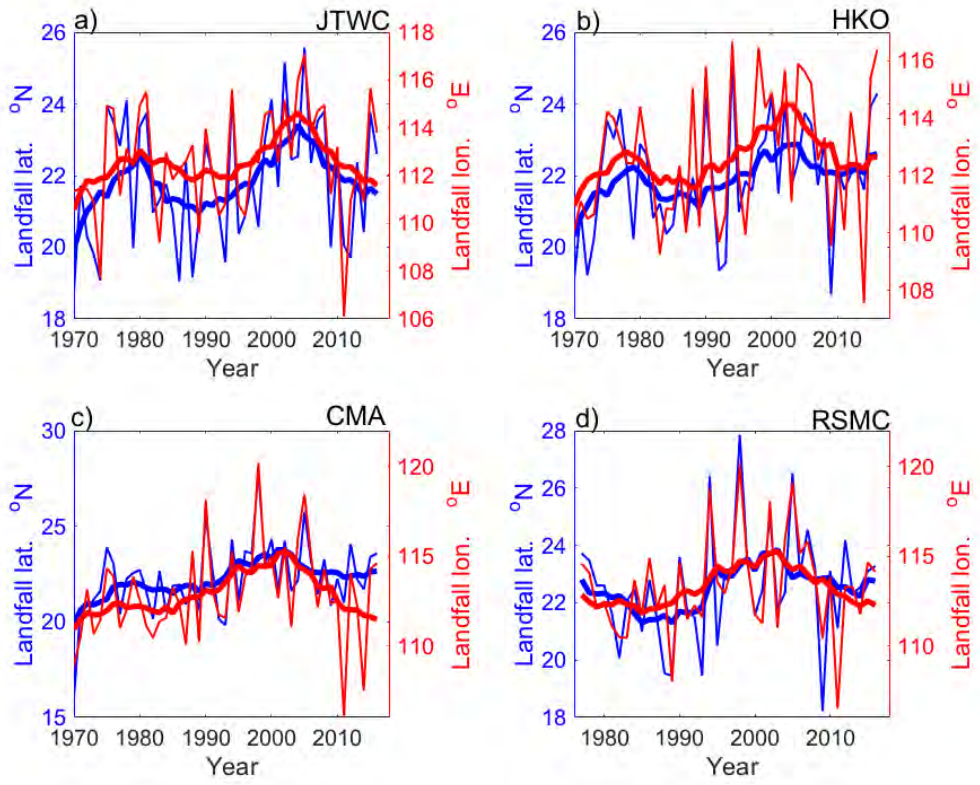

Figure 3.3: Annual change of landfall latitude (blue lines) and longitude (red lines). Thick lines in the same colors are the variations in 10-years moving average. Data from (a) JTWC; (b) HKO; (c) CMA and (d) RSMC

highly correlated with TC landfall intensity (with correlation of 0.36 and 0.45, for HKO and JTWC data, respectively). The result implies that 1^oC in CP warming is associated with $\sim$4 m/s increase of landfall intensity (see Fig. 3.6b).

Chen and Tam[63] examined the impacts of CP El Niño on TC genesis frequency. They found that a large-scale low-level cyclonic anomaly forms over the WNP during CP El Niño, which plays an essential role in determining WNP TC activities. Here four meteorological factors important for TC intensity change, namely potential intensity (PI),

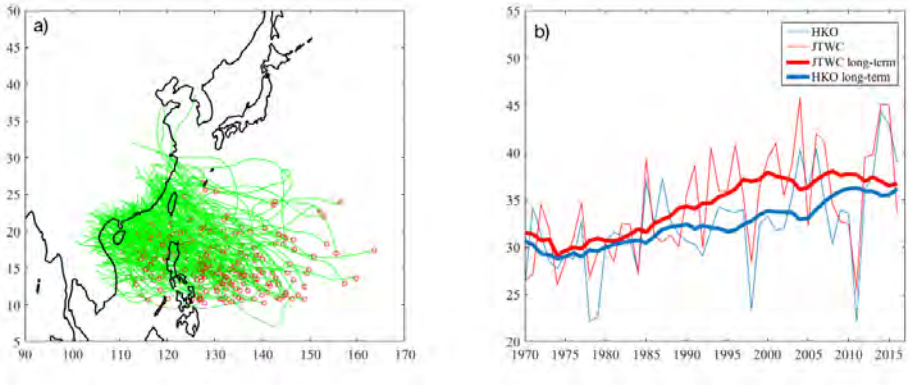

Figure 3.4: Tracks and landfall intensity of the historical TCs making landfall in East Asian cast from 1970 to 2016 in the whole WNP TC season. a) Tracks that make landfall from 10^o N to 30^o N in JTWC; b) Annual mean variation of landfall intensity for the considered land-falling TCs.

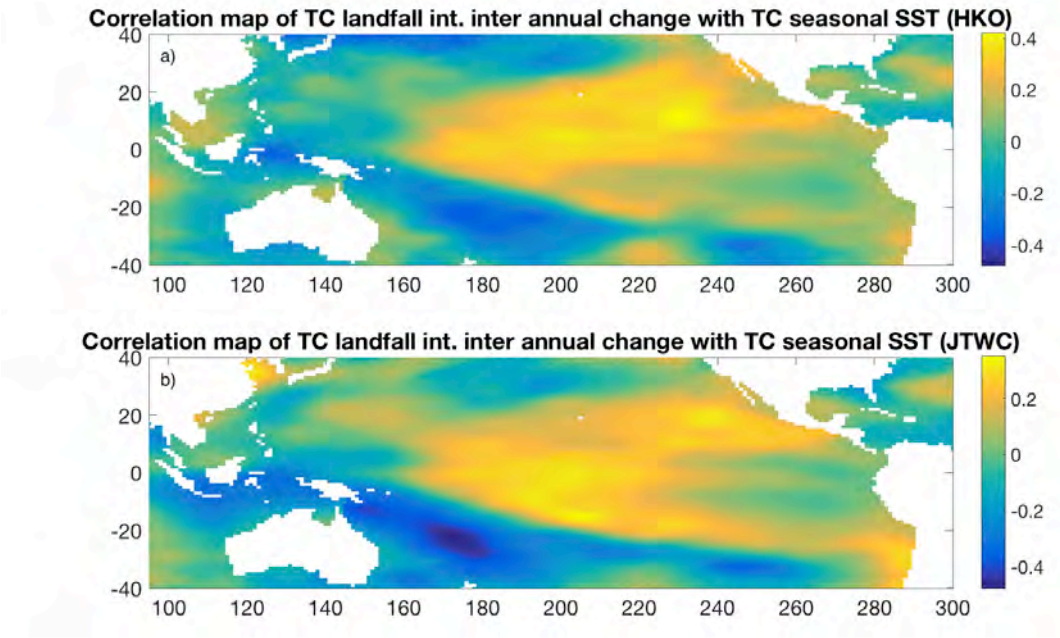

Figure 3.5: Correlation of the inter annual component of TC landfall intensity with SST averaged over MJJASO based on a) HKO and b) JTWC data.

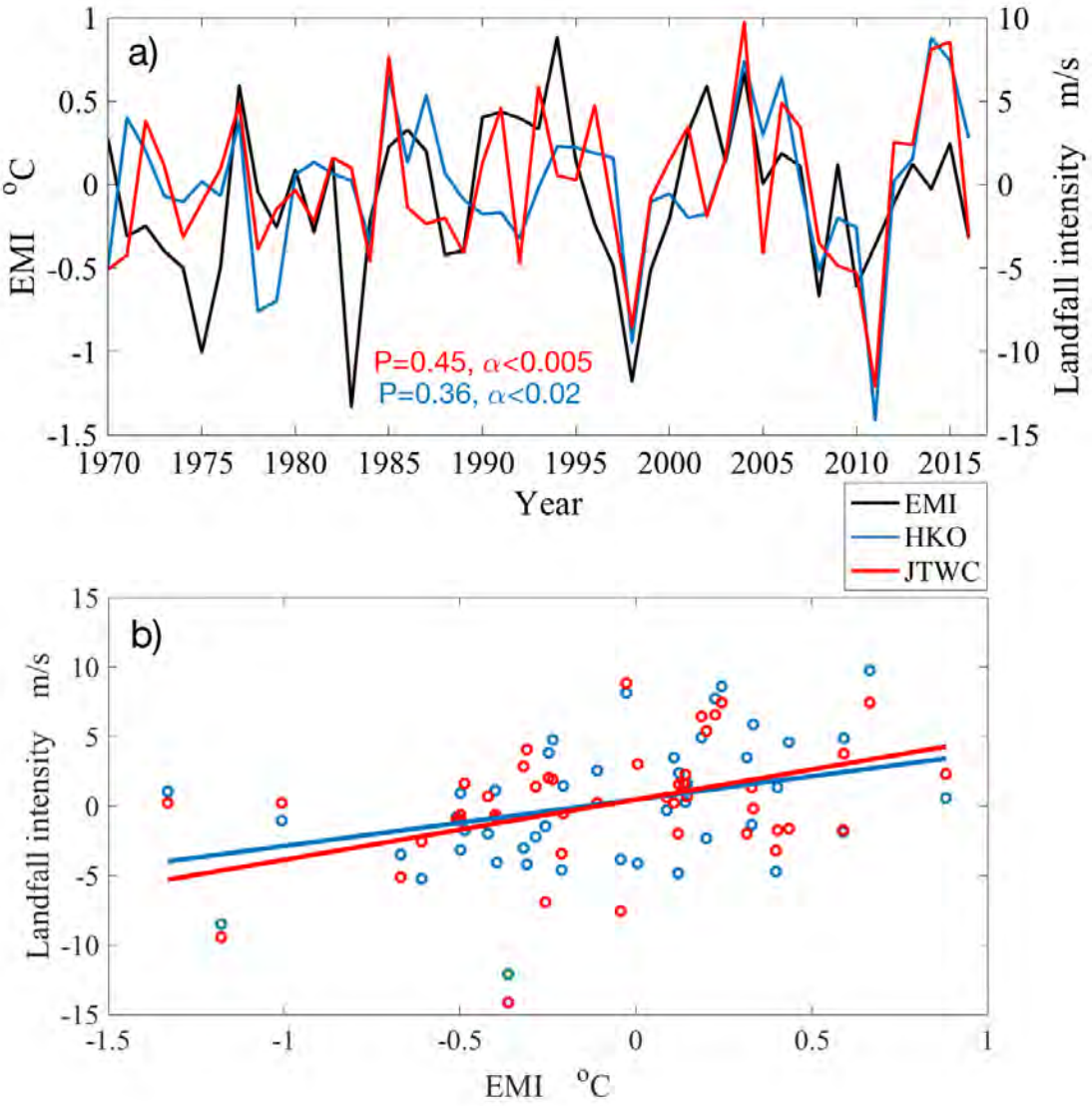

Figure 3.6: Comparison between the MJJASO inter annual component of TC landfall intensity (Units: m/s) and EMI (Units: ^oC) (a) for the period of 1970 to 2015 and (b) in the form of scatter plot.

850 hPa vorticity, vertical wind shear ($\sqrt{(U_{200} - U_{850})^2 + (V_{200} - V_{850})^2}$) and 600 hPa RH are examined. The PI calculation is based on Emanuel's theory[162], which assumes

a TC to be a Carnot cycle. The correlation between EMI and the four meteorological factors, based on NCEP re-analysis 1, are shown in Fig. 3.7. Results from JRA-55 and ERA-Interim are similar (figures not shown). It can be seen from Fig. 3.7 that when CP El Niño occurs, the induced sinking motion in WNP near the Philippines[63] drives a drier atmosphere in the middle level (Fig. 3.7c) while cooler SST leading to weaker PI (Fig. 3.7d) over South China Sea near the Philippines. At the same time, stronger low level vorticity (Fig. 3.7a) and weaker vertical wind shear (Fig. 3.7b) over WNP and East Asia coastline are observed. As most of the active WNP landfalling TCs appear in the above regions, the changes in the two factors are beneficial to the intensification of these storms.

To understand the change of low level vorticity and vertical wind shear, 850 hPa wind field is regressed onto EMI. From Fig. 3.8, stronger zonal wind is found in the South China Sea / the Philippines area (see red box in figure) during CP El Niño years. There is thus more eastward intrusion of summer monsoon trough and stronger low level (850 hPa) vorticity near the Philippines, which coincides with the climatological genesis location of WNP landfall TCs (see Fig. 3.9).

The weakening of vertical wind shear near South China Sea is also caused by the weakening of circulation induced by the cyclonic anomaly. The V- wind could be reduced near south China sea (see Fig. 3.8b) when CP El Niño occurs.

The changes of low level vorticity and wind shear shifted by CP El Niño can also affect

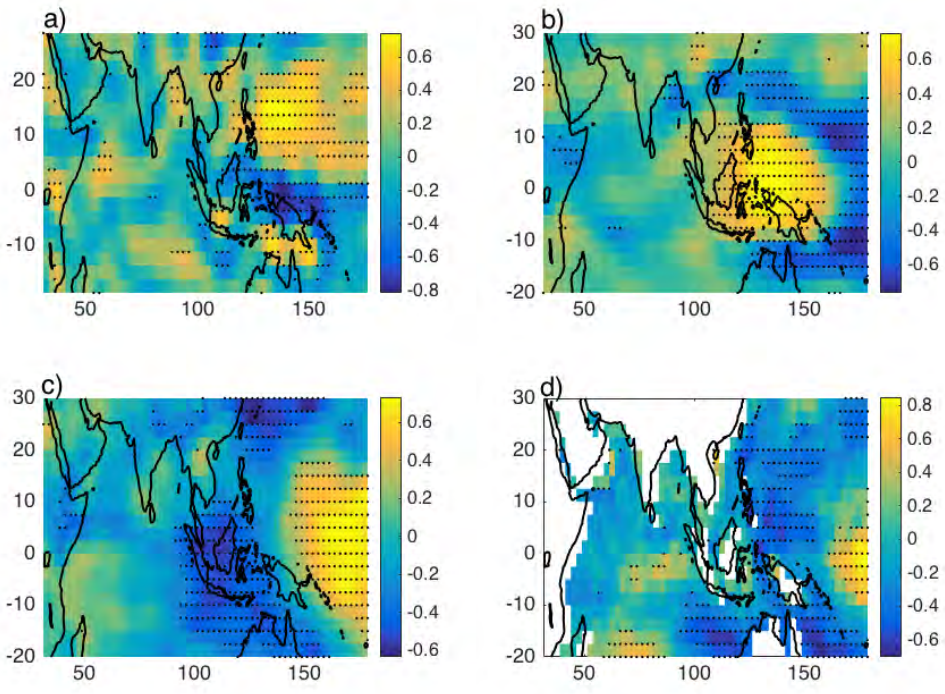

Figure 3.7: Correlation between MJJASO EMI and a) 850 hPa vorticity; b) vertical wind shear; c) 600 hPa RH and d) PI from 1970 to 2015. Black dots indicate locations over which the correlation passes the 90% confidence level. Data from NCEP Reanalysis 1 are used.

WNP TC landfall intensity. Fig. 3.10 shows the regression map of inter-annually varying landfall intensity from JTWC onto the four meteorological factors. It could be inferred that low level vorticity and vertical wind shear are closely associated with WNP TCs landfall intensity, right in the region over which landfall TC genesis and tracks are found. These regression maps of low level vorticity and vertical wind shear are very similar to the correlation maps in Fig. 3.8, suggesting the idea that circulation anomalies during CP El Niño are conclusive on intensifying landfall TCs. In other words, CP El Niño appears

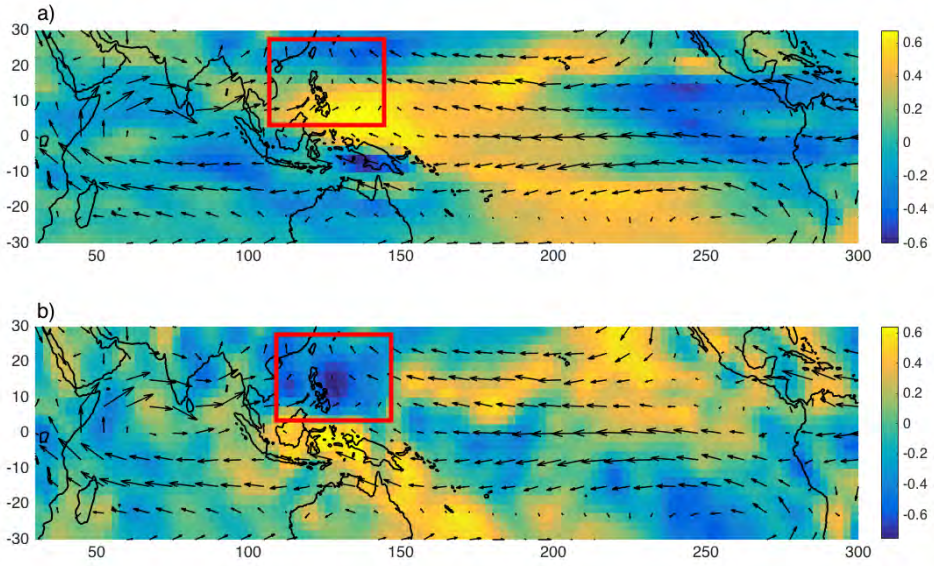

Figure 3.8: Correlation (shading) between MJJASO EMI and a) 850 hPa U- wind and b) 850 hPa V- wind from 1970 to 2015. Shown in the same maps are climatological 850 hPa wind field vectors. Red boxes indicate regions where WNP landfall TCs pass by. Data from NCEP Reanalysis 1 are used.

to affect WNP TCs landfall intensity by increasing WNP low level vorticity and reducing vertical wind shear in the regions of landfall locations.

3.3 Long-term increase of WNP landfall intensity in long term change

Apart from the large inter-annual variability, WNP TC's landfall intensity shows a positive long-term trend in Fig. 3.4. To investigate whether the intensity change is a response of global warming or part of decadal variability, the relation between the long term change

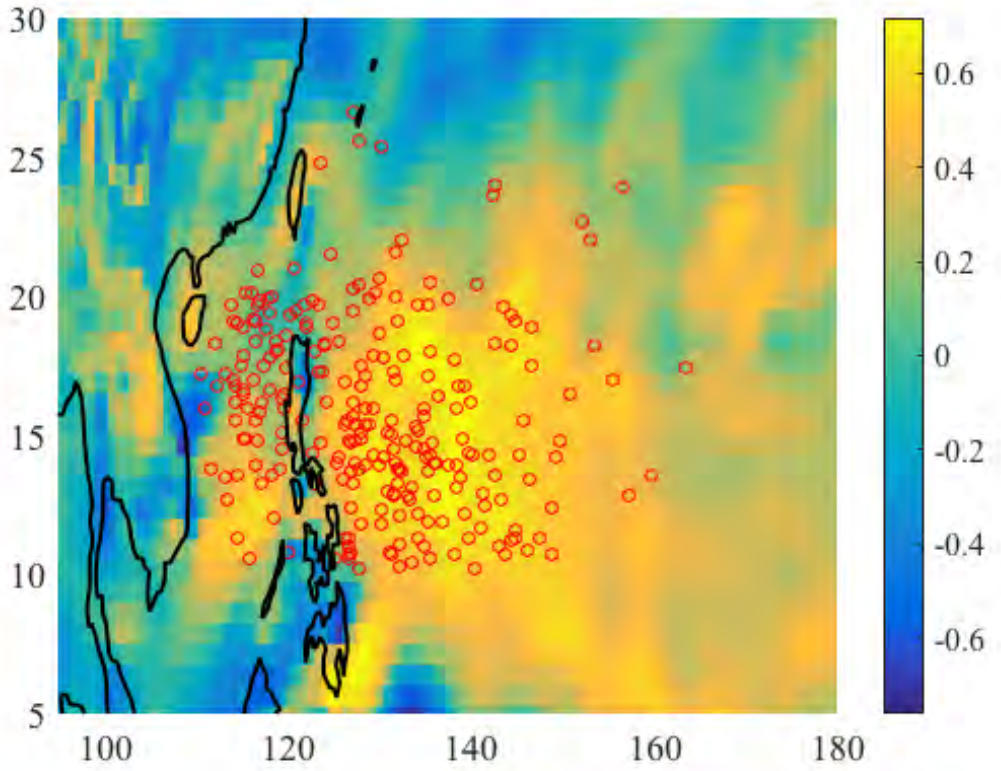

Figure 3.9: Correlation between EMI and 850 hPa vorticity (shading, same as 3.7a) together with WNP landfall TCs genesis location (red circles).

(based on 10-year moving average) of landfall intensity and the four environmental factors (PI, low-level (850 hPa) vorticity, vertical wind shear and 600 hPa RH in ten-year moving average) are examined.

The landfall intensity used is taken from the JTWC best track data, and the four environmental factors are computed from ERA-Interim. The other two datasets, JRA-55 and NCEP-NCAR reanalysis I, were also used and the results are similar to those using ERA-Interim. First, stepwise-regression of landfall intensity onto the four factors are carried

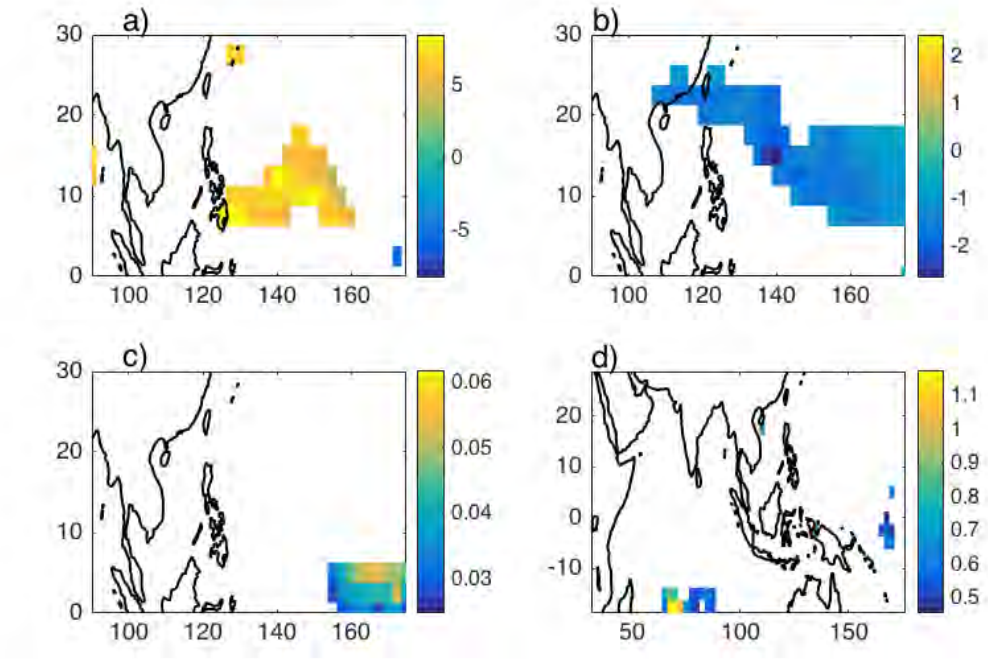

Figure 3.10: Stepwise regression coefficient between the inter-annual component of TC landfall intensity and a) 850 hPa vorticity (Units: m/s per rad); b) vertical wind shear (Units: m/s per m/s); c) 600 hPa RH (Units: m/s per 1%) and d) PI (m/s per m/s) from 1970 to 2016 in MJJASO mean. Only regions above the 90% confidence level are shown.

out, and the results are shown in Fig. 3.11. It can be seen that long-term change of PI and vertical wind shear over WNP are highly related to the increase of landfall intensity during the last few decades. PI is positively related with landfall intensity (Fig. 3.11d), while the relation with vertical wind shear is negative (Fig. 3.11b). Long-term changes of the four environmental factors, average over 110-145^oE, 15-27.5^oN, are shown in Fig. 3.12. All datasets show an increase of PI and weakening of vertical wind shear, consistent with TC's landfall intensity change.

Change of PI is also related with SST and atmospheric stability variations. Based on

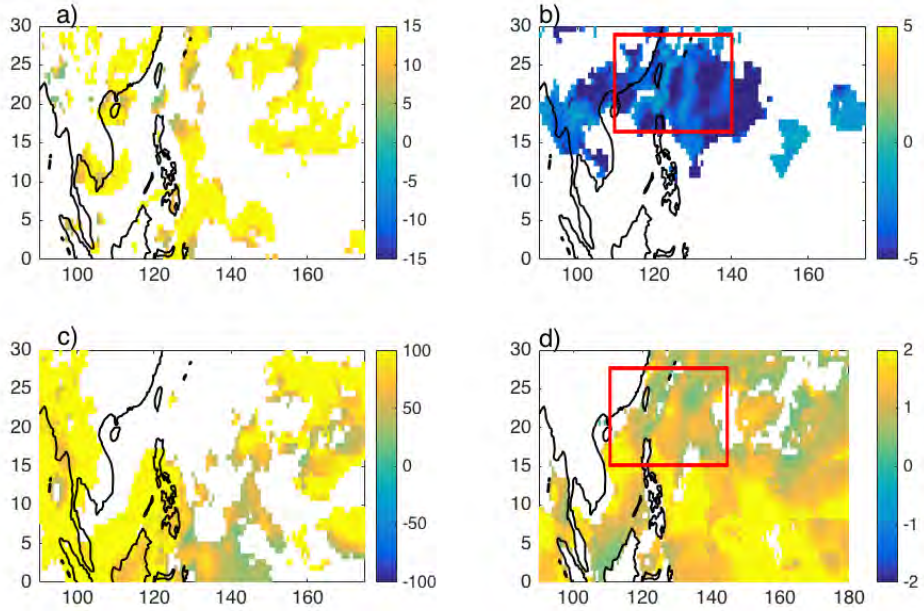

Figure 3.11: Stepwise regression coefficient that of 10-year moving average of TC landfall intensity and (a) 850 hPa vorticity (Units: m/s per 10^{-5} rad); (b) vertical wind shear (Units: m/s per m/s); (c) 600 hPa RH (Units: m/s per 1%) and (d) PI (m/s per m/s) from 1979 to 2016 in MJJASO mean. Shading denotes locations where signals pass the 90% confidence level. The red box covers the region where WNP landfall TCs passed by.

a simplified TC model[162], PI can be calculated as,

$$V_s^2 \simeq \frac{C_k}{C_D}\epsilon(k_0^* - k_a)|_m \tag{3.1}$$

Where V_s is PI, while C_k the enthalpy transfer coefficient and and C_D drag coefficient. ϵ is the thermodynamic efficiency of the Carnot cycle $\epsilon = \frac{T_s - T_o}{T_s}$, in which T_s is the surface temperature and T_o is the temperature at which pressure level heat is exported from the storm system. T_o is strongly controlled by the atmospheric stability and can affect ϵ of

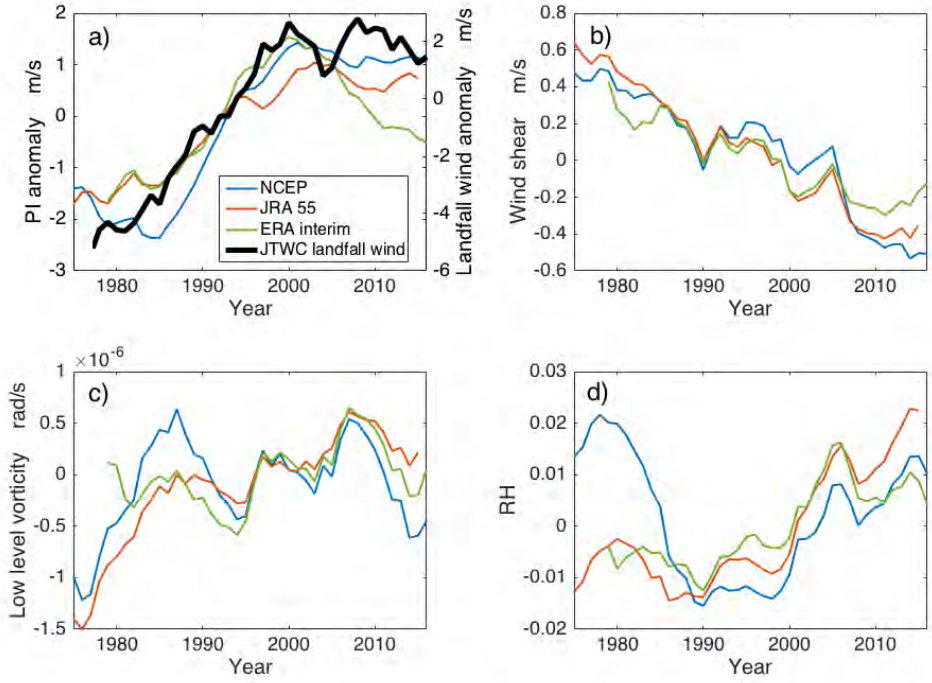

Figure 3.12: The long-term change of a) PI; b) vertical wind shear; c) 850 hPa vorticity; d) 600 hPa RH, averaged in MJJASO and over the considered WNP area (see red box in Fig. 3.11).

the storm. A more stable atmosphere tends to suppress convection in the storm, causing a larger T_o and lower ϵ. k_0^* and k_a are enthalpies of the ocean surface and the atmosphere near the surface, respectively. k_0^* is controlled by SST; warmer SST can provide stronger enthalpies and cause a stronger PI. $|_m$ means that all the quantities are evaluated near the RMW. In summary, SST warming enhances PI of TCs, while a more stable atmosphere can reduce PI.

To test the relationship between SST, atmospheric stability, and PI, their area-averaged values (see red box in Fig. 3.11) are calculated. The atmospheric stability is calculated

as $-\frac{\Delta\theta}{\Delta p}$ and between the nearest two pressure level and then the vertical level from 1000 hPa to 300 hPa are averaged. The results are shown in Fig. 3.13, in which both JRA-55 and and ERA-Interim data are used (NCEP re-analysis data gives a vertical temperature structure in the upper levels which is not consistent with the other 2 datasets, and hence the results are not considered). The area-averaged SST was seen to increase rapidly during the last few decades (Fig. 3.13 a & d), while the atmosphere was also becoming more and more stable (Fig. 3.13 b & e). The combined effects due to changes in these two factors can be seen in determining the change of PI during the same period (see Fig. 3.13 c & f). Red lines in Fig. 3.13 c & f are the PI values fitted from SST and atmospheric stability. The fitted PI matches the observed values well, supporting the notion that local SST and static stability change strongly affect PI variations.

Local SST warming and a more stable environment are in line with the influence of global warming in the past few decades. Note that other variabilities, such as so-called warming hiatus after around 2000 (Figs. 3.13 a,d), which was arguably part of natural climate variability, due to a La-Niña-like decadal cooling, might also affect these two environmental factors[163]. Nevertheless, SST change in relation to global warming is still the dominant signal, suggesting the increase of PI can be attributed to a warmer climate.

Besides local SST, weakening of wind shear over South China Sea and WNP also contributed to the enhancement of landfall intensity (see Fig. 3.12b). To relate this to changes in the general circulation, upper- (200 hPa) and low-level (850 hPa) wind in the

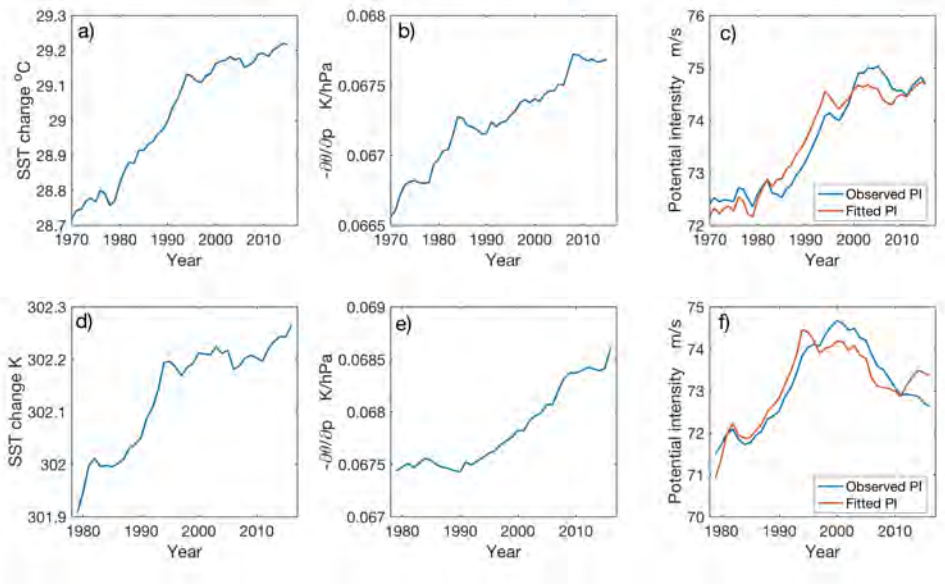

Figure 3.13: The MJJASO mean long-term change of (a,d) SST (Units: K), (b,e) static stability (Units: K/hPa) and (c,f) PI (Units: m/s) averaged over the WNP area of 110-145^oE, 15-27.5^oN (see red box in Fig. 3.11). Results (a,b,c) are based on JRA-55 data, and (d,e,f) ERA-Interim data.

MJJASO season are examined. The long-term variations of the wind fields are shown in Fig. 3.14, calculated by taking 10-year moving averages. It is seen that the NCEP-NCAR reanalysis, JRA-55 and ERA-Interim all show a consistent weakening of 200 hPa U- wind, which is the main reason for reduced vertical wind shear in typhoon season. ERA-Interim shows a stronger 200 hPa U- wind may because only JJA are considered, and the circulation is stronger in JJA season than that in May to October.

In order to examine the weakening of the 200 hPa U- wind, the 200 hPa wind field change in Euro-Asia area are calculated by subtracting the difference between the MJJASO mean of 1989-2016 and 1961-1988. The results starting from 1961 are similar to

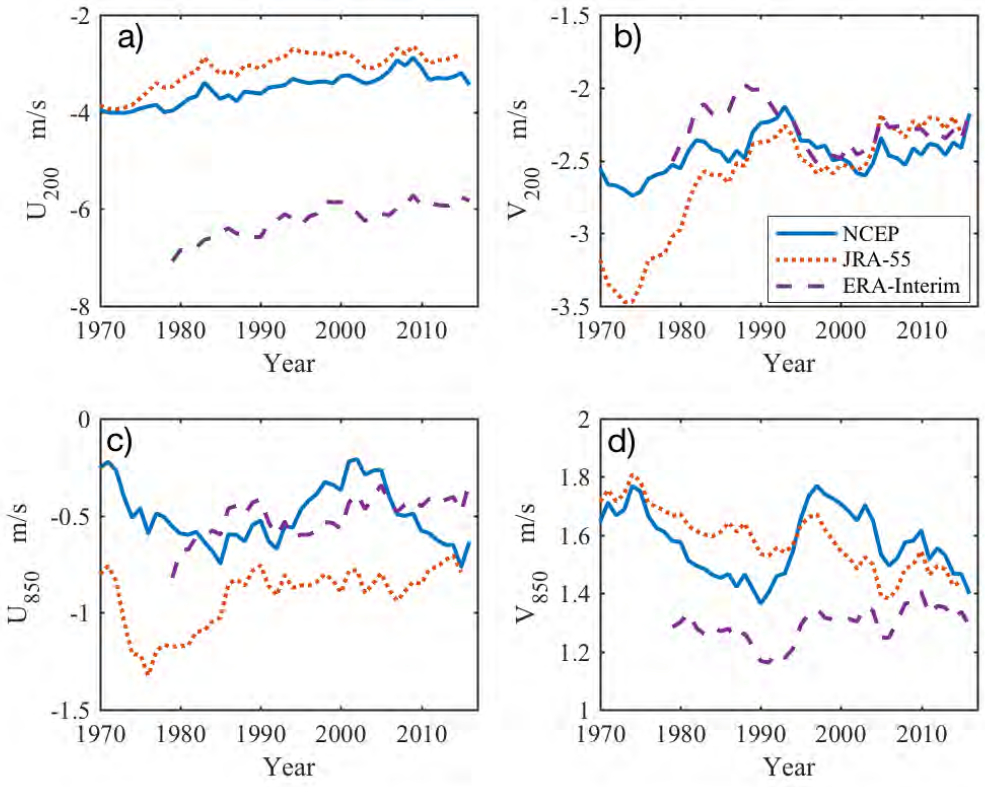

Figure 3.14: The long-term change of the MJJASO mean (a) 200 hPa U- wind; (b) 200 hPa V- wind; (c) 850 hPa U- wind and (d) 850 hPa V- wind from NCEP Reanalysis 1, JRA-55 and ERA-Interim datasets averaged over the considered WNP area (see red box in Fig. 3.11). The wind field derived from ERA-Interim is calculated in JJA.

those from 1970, but more stable and obvious. The 200 hPa wind field change from different datasets are shown in Fig. 3.15. The background wind field near South China Sea is north-easterly due to the anti-cyclonic wind field induced by South Asia High, while all the three datasets show the south-westerly wind anomaly in the later period (see Fig. 3.15b-d), indicating a weakening of the north-easterly. The wind field change from NCEP (Fig. 3.15b) is similar with that from JRA-55 (Fig. 3.15b), with a cyclonic wind anomaly

in central east China ($115^oE, 30^oN$). ERA-Interim started the reanalysis data from 1979, so the difference are calculated by the periods of 1979-1997 and 1998-2016. Although the weakening signal in ERA-Interim dataset is not as strong as the other two datasets, the cyclonic wind anomaly can also be seen near south China ($110^oE, 20^oN$).

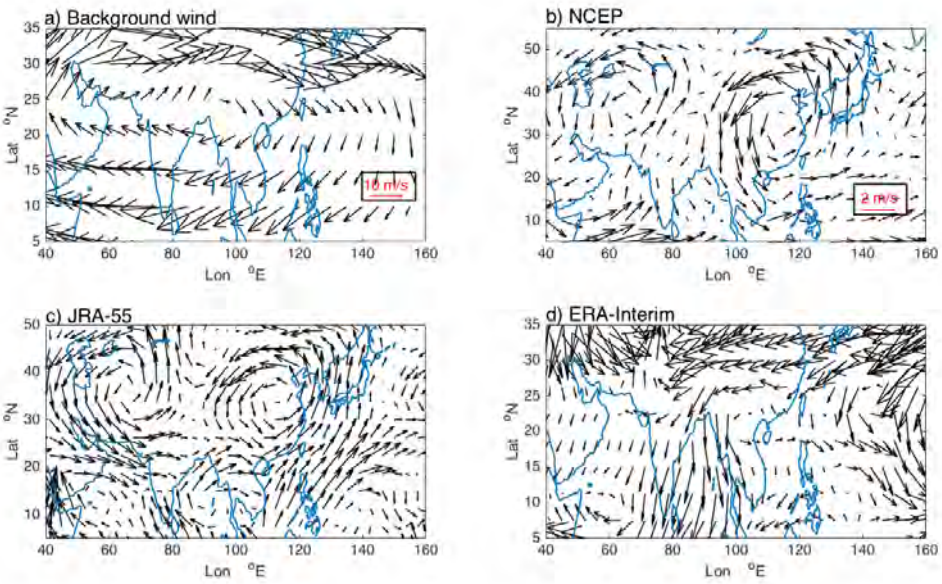

Figure 3.15: The wind field change in MJJASO from 3 datasets. (a) 200 hPa background wind field based on NCEP Reanalysis I; (b) NCEP Reanalysis I 200 hPa wind anomaly, using mean of wind field in 1989-2016 minus that in 1961-1988; (c) JRA-55 200 hPa wind anomaly, using mean of wind field in 1989-2015 minus that in 1961-1988 and (d) ERA-Interim 200 hPa wind anomaly, using mean of wind field in 1997-2016 minus that in 1979-1996. The wind field derived from ERA-Interim is calculated in JJA.

The weakening of the 200 hPa wind field is highly related to the change of 200 hPa geopotential height. Fig. 3.16 compares the geopotential height change in the two different periods which is the same periods in Fig. 3.15 for the same dataset (For ERA-20C, the periods are 1961-1985 and 1986-2010). It can be seen from Fig. 3.16 that all the

four datasets show a decrease of South Asian High (SAH), which reduced the geopotential height in 200 hPa level near South China Sea. The reduced geopotential hight could weaken the 200 hPa anti-cyclonic wind field above South China Sea. Due to the short data period, the weakening of SAH and geopotential height above South China Sea in the ERA-Interim data is not strong, but the decrease signal can still be detected ($\sim$ 2m, see Fig. 3.16)e-f). To get a longer record from ECMWF datasets, ERA-20C is applied to check the change of geopotential height in the period from 1961 to 2010. And the change of geopotential height in ERA-20C shows a weakening of SAH and a decrease of geopotential height near South China Sea, which is very similar to the results from NCEP and JRA-55 (see Fig. 3.16 g,h).

Applied the later periods deducted by the earliers, the geopotential height change is shown in Fig. 3.17. It can be seen that the 200 hPa geopotential height decreased 2-10m near South China Sea. Except ERA-Interim, all the other 3 datasets show a similar pattern with a low pressure anomaly near central east China, where is the exact area the cyclonic wind anomaly appears in Fig. 3.15.

From the above analysis, it can be concluded that the long term change of WNP landfall intensity in the period of 1970-2016 was highly related to the increase of local potential intensity and weakening of vertical wind shear in the area of the genesis and trajectories of WNP landfalling TCs.

The increase of local potential intensity was strongly affected by the local warming

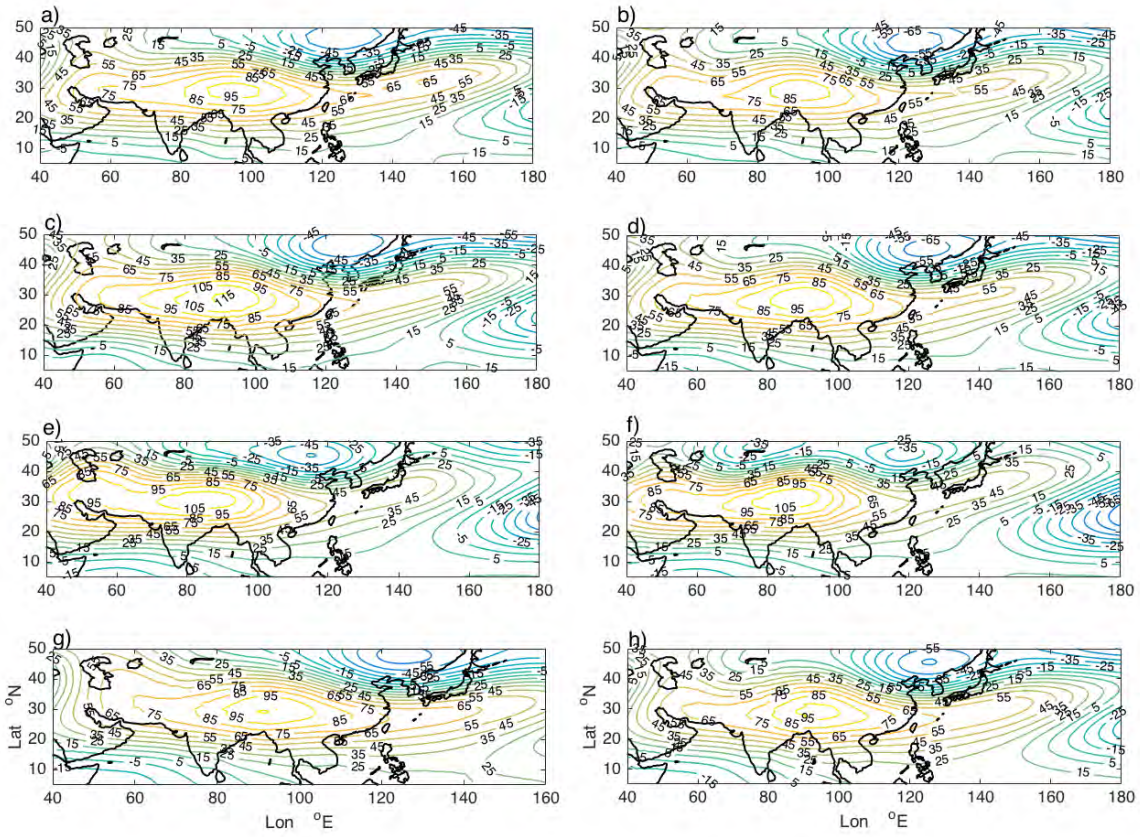

Figure 3.16: Comparison of geopotential height (Units: m) in MJJASO in two different periods from 4 reanalysis datasets. (a), (c), (e), (g) are the mean geopotential heights in earlier periods from NCEP, JRA-55, ERA-Interim and ERA-20C respectively. (b), (d), (f), (h) are the mean geopotential heights in later periods from NCEP, JRA-55, ERA-Interim and ERA-20C respectively. The earlier and later periods are the same with those in Fig. 3.15, and the two periods for ERA-20C are 1961-1985 and 1986-2010. The zonal mean of geopotential height is removed from the field.

of SST (positive effect) and the more stable atmosphere (negative effect) under the rapid global warming condition from 1960s. The weakening of the wind shear near South China Sea is highly related to the 200 hPa U- wind due to a weakening of SAH system. Ding ***et al.***[164] suggested the weakening of SAH was closely related to some natural factors.

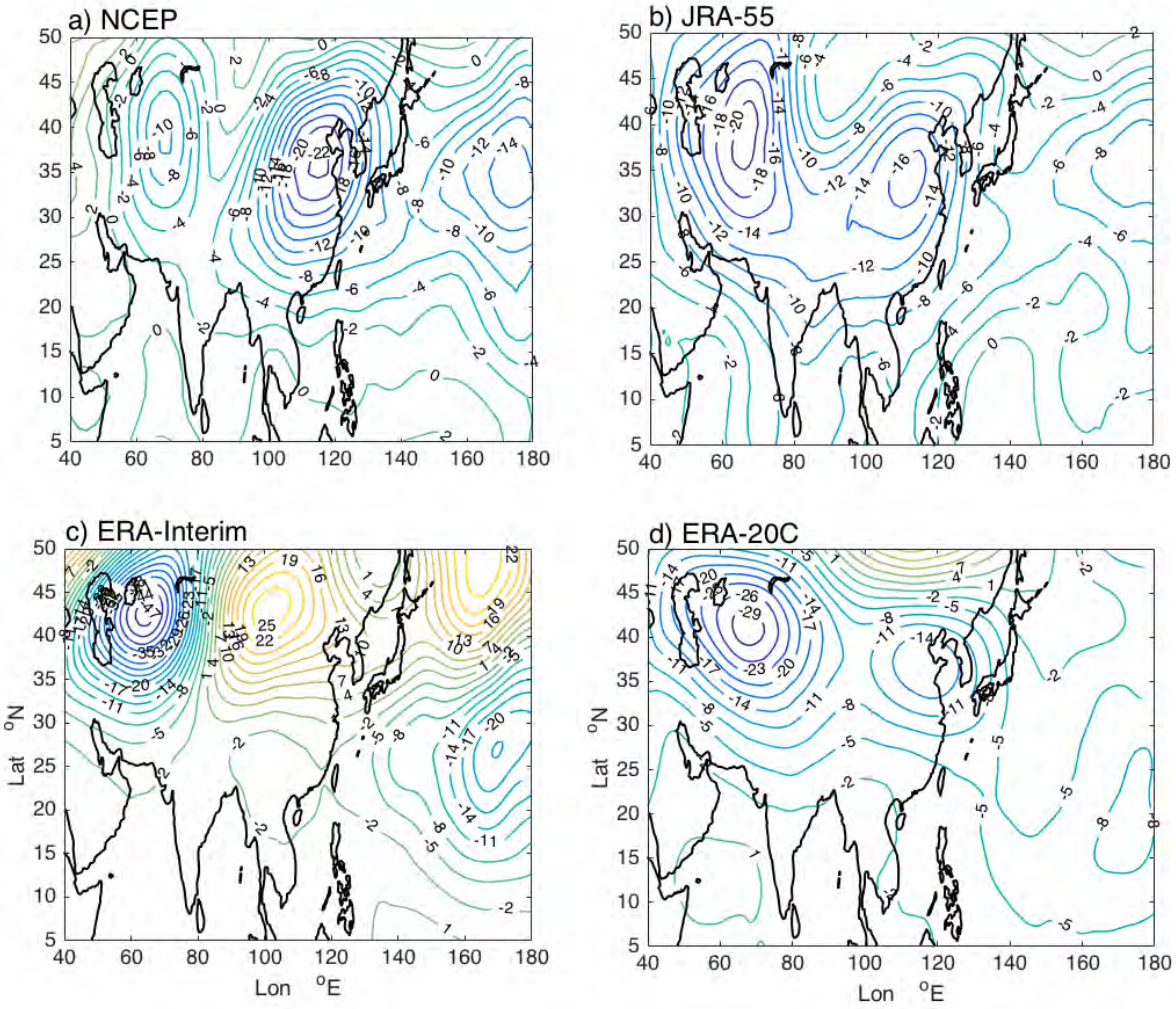

Figure 3.17: The 200 hPa geopotential height change in MJJASO from 4 reanalysis datasets. (a) NCEP 200 hPa geopotential height anomaly, using mean of geopotential height in 1989-2016 minus that in 1961-1988; (b) JRA-55 200 hPa geopotential height anomaly, using mean of geopotential height in 1989-2015 minus that in 1961-1988 and (c) ERA-Interim 200 hPa geopotential height anomaly, using mean of geopotential height in 1997-2016 minus that in 1979-1996; (d) ERA-20C 200 hPa geopotential height anomaly, using mean of geopotential height in 1986-2010 minus that in 1961-1985. The wind field derived from ERA-Interim is calculated in JJA.

One reason for the decrease of SAH is that Tibetan Plateau (TP) underwent abrupt increase in the winter and spring snow over the TP since around 1977, which reduced the surface sensible heat flux into the atmosphere and subsequent cooling over the TP and its surrounding atmosphere. Mean while, three phases of significant inter-decadal warming of the SST in the tropical central and eastern Pacific, which occurred in the mid-1960s, the late 1970s and the early 1990s, respectively, have been found. The above inter-decadal variabilities over land area in the Asia and the WNP have consistently reduced the land-sea thermal contrast in summer in the Asian monsoon region. Based on the two reasons above, the weakening of wind shear may be related to some natural factors. But some other researches argued the anthropogenic aerosols emissions in India and Asia reduced local incoming radiation and induced a slowdown of the tropical meridional overturning circulation, and eventually weakened the South Asia summer monsoon[165]. Based on the two different explanations, the reason of weakening of SAH system is still not clear.

3.4 Stronger influences on inland areas

Stronger TC landfall intensity may lead to longer sustaining time and distance travelled by storms over inland areas.To test the relation between landfall intensity and the sustaining time, in this section, considered TCs must dissipate over land without re-entering to the ocean, to avoid re-intensification. Also, the decay process is considered to be completed when TC intensity is less than 17 m/s. One reason is that technologies for detecting weaker

intensity in earlier times were not as accurate as the present, such as the development of Radar and satellite in observing the activity of a storm is much improved in nowadays. Taking the HKO data as an example, Fig. 3.18 shows a clear change of the final intensity at which the HKO stops the announcement service since 1970. Each blue circle represents the final intensity of a TC issued by the HKO. It can be seen that there was a huge difference for the terminal intensity between before and after 1979, indicating the observed TC decay process may have larger uncertainty in the early years (before 1979) in HKO best track dataset.

After stopping the decay process at 17 m/s, all the four best track datasets show well consistency with each other. Fig. 3.19 shows the final places that the TCs can travel to at 17 m/s from the four datasets, and it is found that the farthest region the TCs can reach are similar in all four datasets, indicating the reported decay process from four dataset are consistent when limiting the considered storms stronger than 17 m/s.

The change of translation speed of the landfall TCs also suggests that stopping the decay process at 17 m/s is reasonable. It was reported that the translation speed was getting slower during the past decades[166], but when the TC's lifetime is divided into periods of stronger and weaker than 17 m/s, the slowdown of translation speed only happens when the TC's intensity is weaker than 17 m/s, while there is no trend for the translation speed when the intensity is stronger than 17 m/s (see Fig. 3.20). This suggests that the translation speed is in consistent during the considered period.

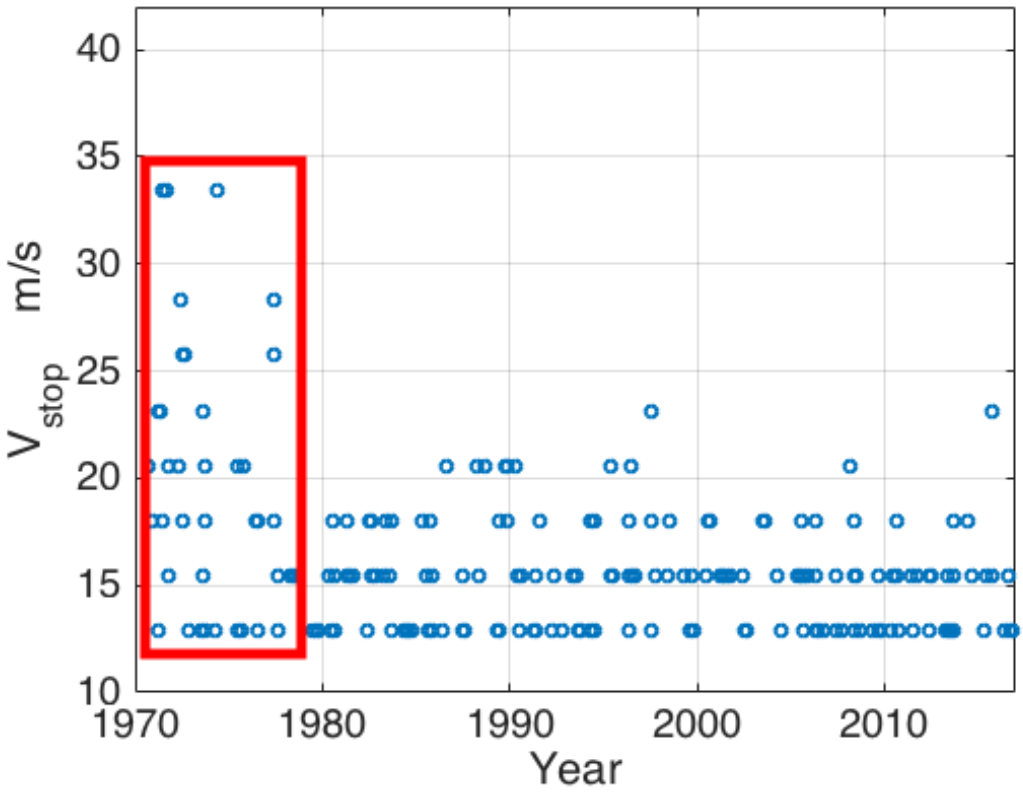

Figure 3.18: TCs' final intensity issued by HKO. Every blue circle represents one landfalling TC. Blue circles in the red rectangle are the TCs' terminal intensities announced before 1978.

Taking the annual average of TC intensity and time over land, the relationship between the mean TC landfall intensity and sustaining time over land can be studied. As illustrated in Fig. 3.21, these two parameters are positively correlated for all the 4 best track datasets (passing the 99% confidence level). This indicates that stronger landfall intensity can lead longer decay after TC landfall. For an increase of 1 m/s of landfall intensity, the sustaining time could be extended by about 0.59 hour.

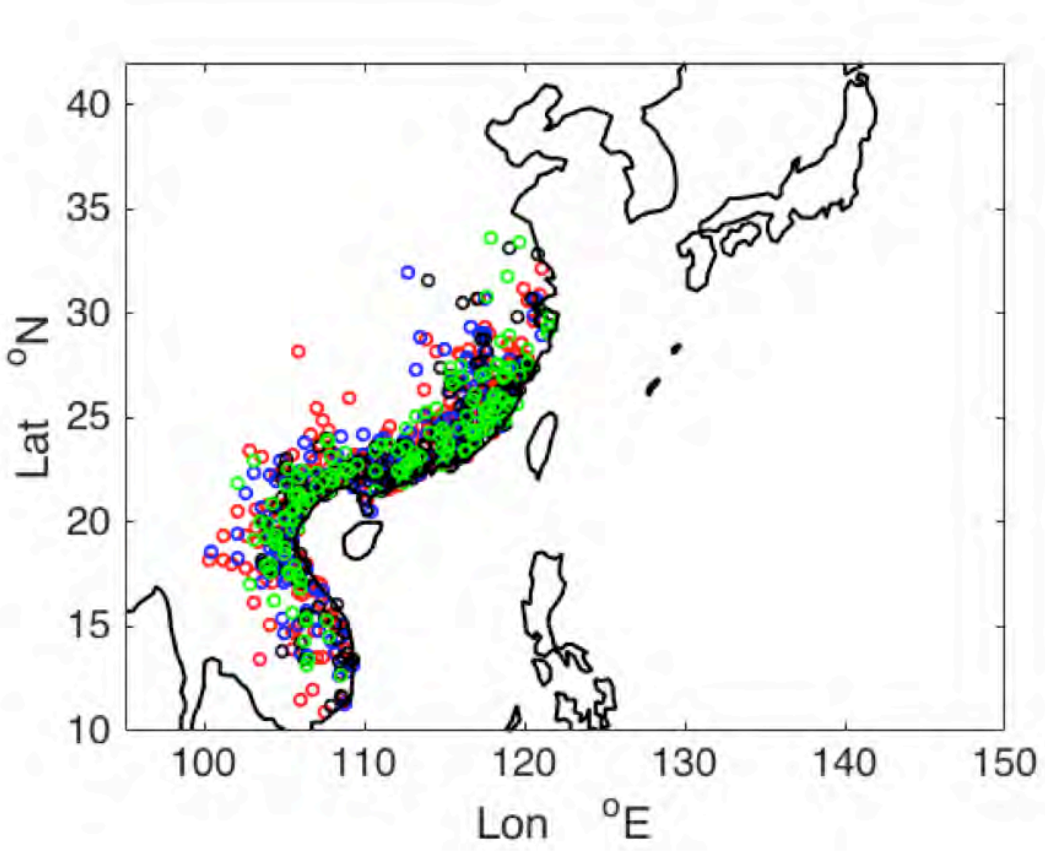

Figure 3.19: Terminal places the TCs can reach when cutting the minimum intensity at 17 m/s. Circles in red, blue, black and green represent results from JTWC, HKO, CMA and RSMC, respectively.

The increase of landfall intensity (see Fig. 3.4b) can therefore lead to TCs surviving longer and affect larger inland areas. Here the sustaining time, distance travelled and PDI over land are considered. Translating distance is the sum of distance between the adjunct two track locations during the decay process. And PDI is the integration of v^3 of all the time steps during the decay. The annual mean of these three variables are shown in Fig. 3.22. All three factors show a strong increase trend during the last few decades. Sustaining

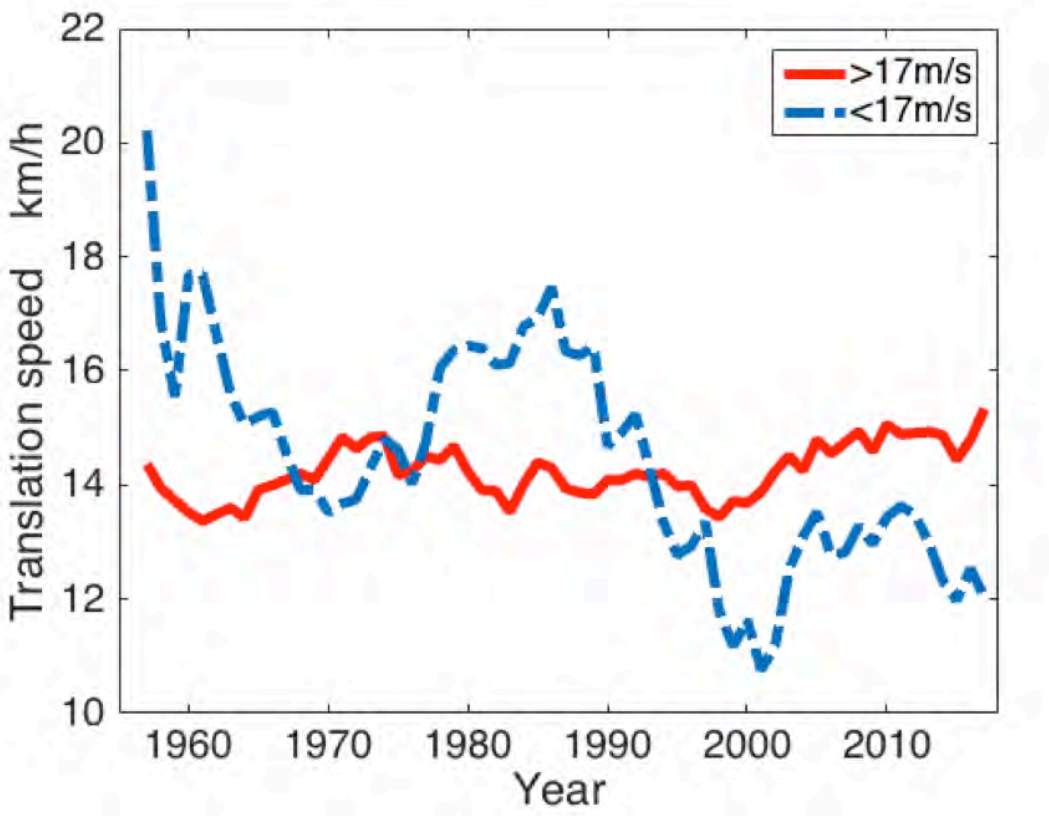

Figure 3.20: The translation speed of the selected TCs when their intensities are stronger than (red solid line) and weaker than (blue dash-dot line) 17 m/s. The results are in 10-year moving average. Data is from HKO.

time after landfall was doubled from 1970 (∼7 hours) to 2016 (∼13 hours), and travelling distance was also increased in the same period by 67%, from 150 km to 250 km. PDI over land area was also doubled.

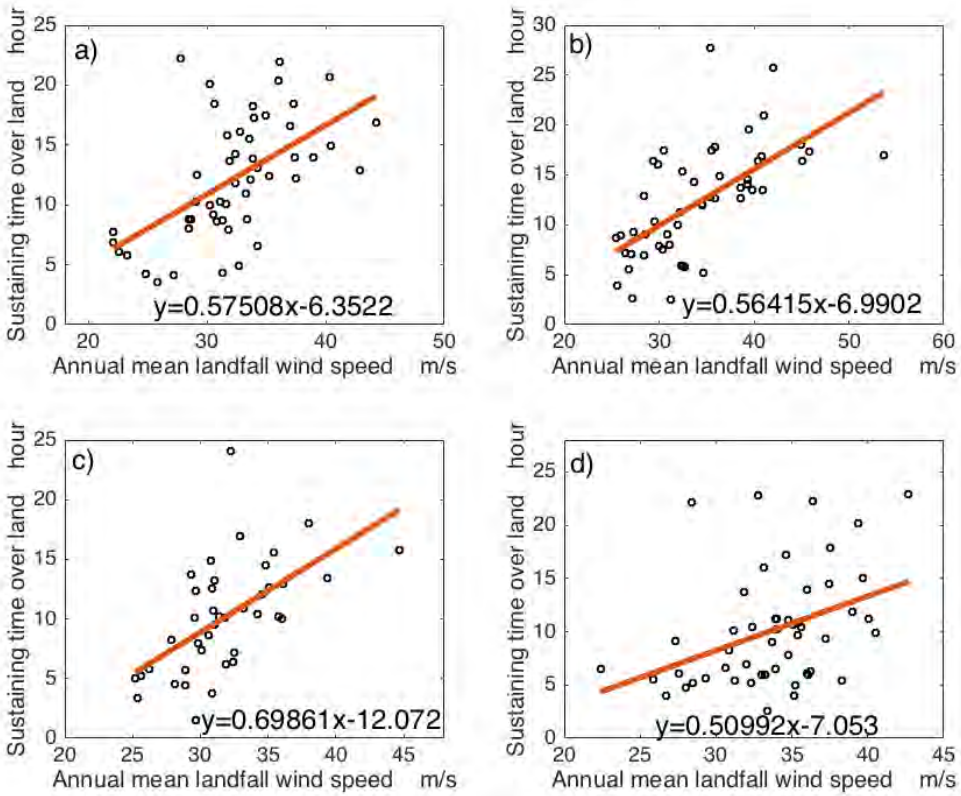

Figure 3.21: Relationship between WNP TC landfall wind speed and sustaining time after landfall. Data are taken from (a) HKO; (b) JTWC; (c) RSMC and (d) HKO.

3.5 Typhoons impacts on coastal regions vs inland areas

In Chapter 3.4, it has shown that relation between landfall intensity and the sustaining time over land seems to be linear according to JTWC, RSMC and HKO best track data; however, it is not the case for the CMA dataset (see Fig. 3.21). At the same time, PDI over land is expected to be proportional to cube of landfall intensity ($PDI = \int v^3 dt$). Interestingly, PDI over land shows a strong positive linear relation with landfall intensity,

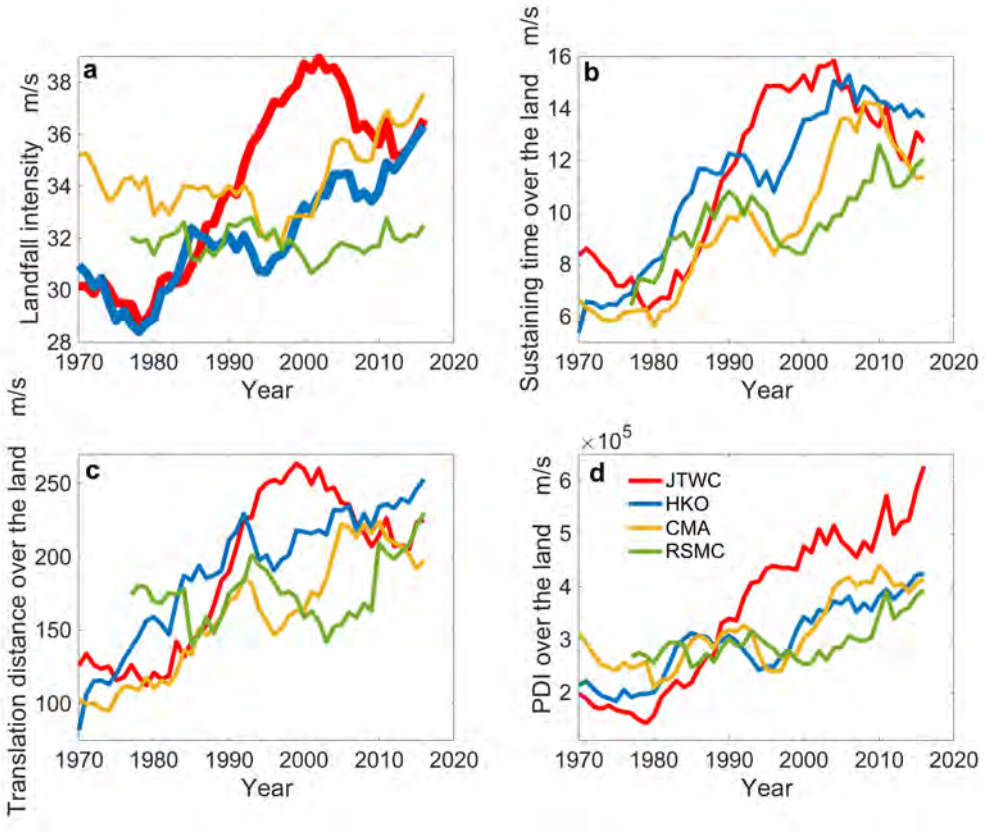

Figure 3.22: Variations of (a) TC landfall intensity; (b) sustaining time over land; (c) translating distance over land and (d) PDI over land.

as seen in Fig 3.23. The correlation coefficient is more than 0.8 for JTWC, HKO and RSMC data, and 0.63 for CMA.

To further understand the link between landfall intensity and PDI after landfall, the landfall intensity and sustaining time over land for all landfall TCs are compared in Fig. 3.24. The methods of calculating landfall intensity and sustaining time over land are the same with those in Chapter 3.4. It can be seen that the envelope of the sustaining time over land does not always increase with the landfall wind speed. The longest sustaining time

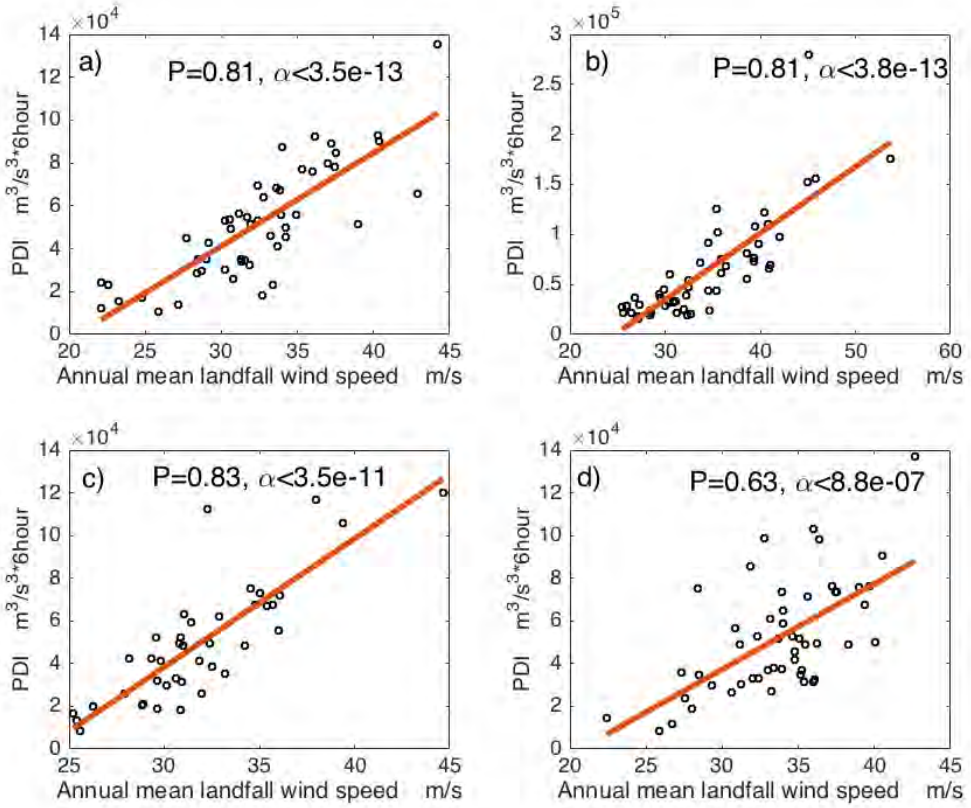

Figure 3.23: Relationship between WNP TCs landfall wind and PDI over land. Results derived from (a) HKO; (b) JTWC; (c) RSMC and (d) CMA dataset.

that TC can reach at one specific landfall wind speed increases with V_0 before a critical wind speed value, and when the V_0 is stronger than the critical value, the outmost number of sustaining time will not increase versus V_0 or even decrease, which can be seen in all the best track datasets except JTWC (see Fig. 3.24). The red lines in Fig. 3.24 are the mean sustaining time after landfall. For small values of V_0, TCs can sustain longer as a function of V_0; however, beyond some critical value of V_0 (for example 35 m/s in RSMC dataset), the time TC can sustain over land decreases or stays steady as V_0 increases. Thus

suggests that the relation between landfall intensity and sustaining time after landfall is not linear.

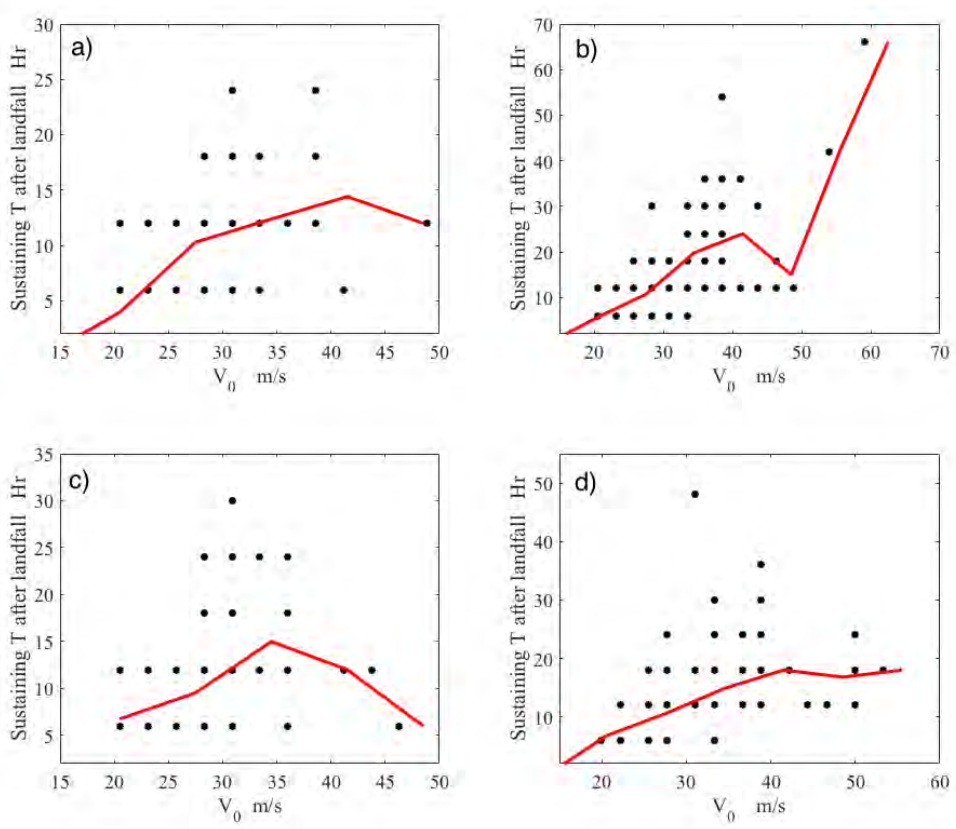

Figure 3.24: The observed relation between TC landfall intensity and sustaining time after landfall. Data derived from (a) HKO; (b) JTWC; (c) RSMC and (d) CMA. Black dots are the scatterings of all the selected TCs, and the red lines are the bin average of sustaining time over land in a V_0 bin, with the bin window of 7 m/s.

It should be mentioned that, in the analysis of Fig. 3.24, all best track data are in 6-hour interval, which makes it difficult to determine the lifetime of TC up to the moment when the wind speed is 17 m/s exactly. One way to find out the exact time corresponding

to 17 m/s of wind speed is to apply an empirical model to fit the TC decay process. Such an empirical decay model is described in Chapter 2.2.1. To get more accurate and robust results, only WNP landfalling TCs after 1979 are selected. Moreover, the landfalling TC must stay at least 12 hours over land, such that there are at least 3 data records for the use of fitting. Also, the TC considered must not recurve back to the ocean after landfall. The tracks of these TCs over land are illustrated in Fig 3.25. From 1979, there are 97 TCs satisfying these criteria in the JTWC dataset, 94 in the CMA; the numbers in the HKO and RSMC data are relatively low, being with 67 and 36, respectively. This may be related to the relative weak intensity in the HKO data, due to the use of 10-min wind for the maximum surface sustaining wind speed (1-min and 2-min winds are adopted by JTWC and CMA, respectively). RSMC also makes use of the 10-min wind, also, the observation period starts from around 1985.

Based on the empirical model, a time scale factor τ (see Eq. 2.4) can be fitted for every selected TC. τ reflects how fast the TC will dissipate. Fig. 3.26 gives the variation of τ vs landfall intensity. It can be seen that τ decreases with stronger landfall intensity, implying faster decay rate for stronger TCs. Previous studies also show similar findings[124, 167, 168]. The phenomenon may be related to the increase of friction, from ocean to land surface[168, 169]. Other studies argued the reduction of evaporation plays the most important role in the TC decay over land[170]. When the evaporation is suppressed, the storm eventually weakens whether the surface roughness is increased or

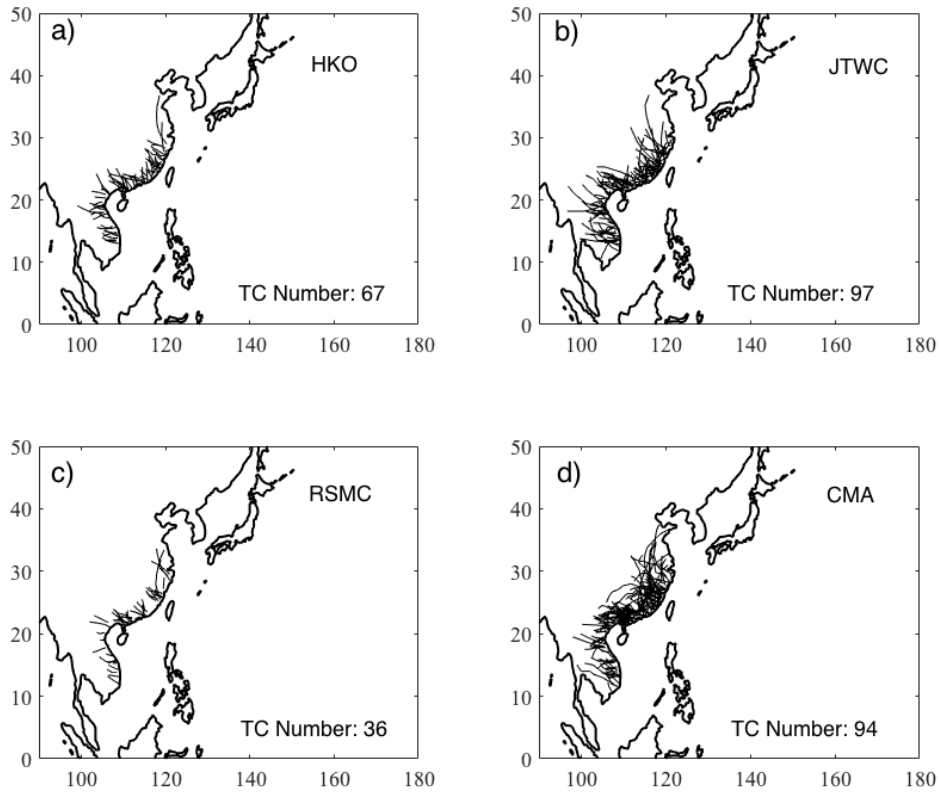

Figure 3.25: Tracks of selected WNP landfall TCs over land based on data from (a) HKO; (b) JTWC; (c) RSMC and (d) CMA.

not[171]. But it is also indicated that surface roughness and reduced relative wetness do enhance decay at landfall[168].

According to the above, TCs with stronger landfall intensity may not prolong the decay process too much compared to those with weaker intensity. With the help of the fitted τ, better estimation of sustaining time and PDI over land can be calculated. From Eqs. 2.6 and 2.7, TC sustaining time is a log function of landfall intensity V_0, while PDI over land

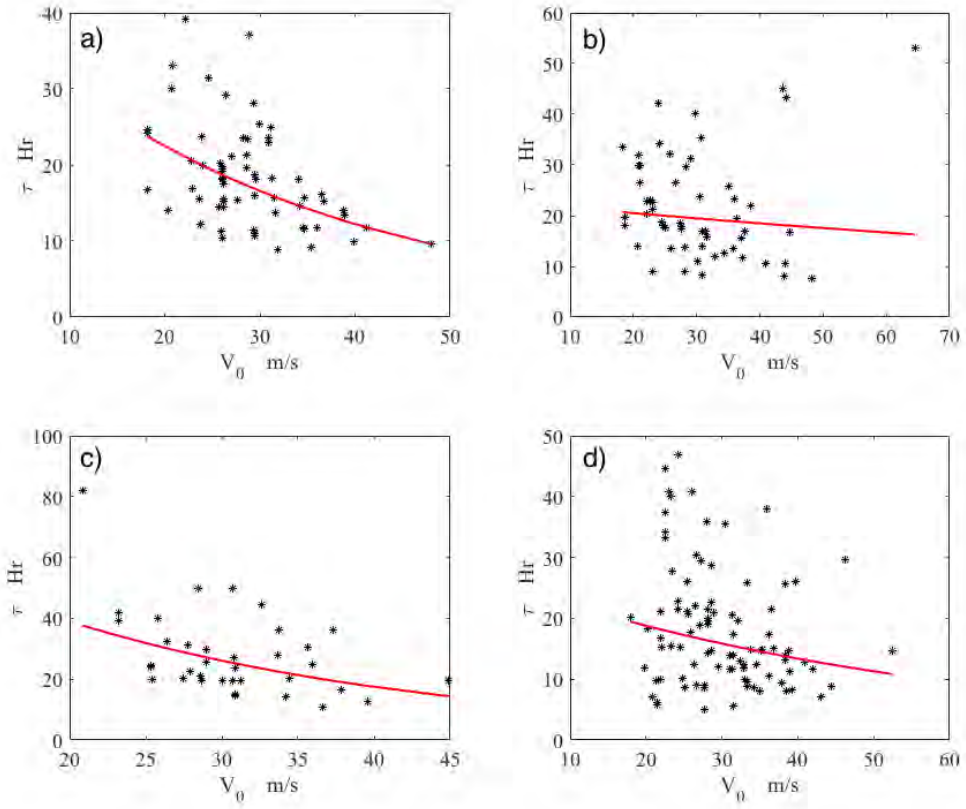

Figure 3.26: The relationship of time scale factor τ with TC landfall intensity. Results derived based on (a) HKO; (b) JTWC; (c) RSMC and (d) CMA data.

is almost in v^3, if τ is a constant. But τ decreases with V_0, leading to even slower increase of sustaining time and PDI over land. The fitted relationship between sustaining time and landfall intensity is shown in Fig. 3.27. The estimated observed sustaining time-landfall intensity relation is in line with that shown in Fig. 3.24. The red curves in Fig. 3.27 are the quadratic fits. Except JTWC, all other datasets show that the sustaining time reaches a maximum at some landfall intensity value (of about 30-40 m/s), above which the

sustaining time no longer increases (or even decreases). JTWC data do not give a slowing down of sustaining time (see Fig. 3.27b), which is a result of weak τ-V_0 relation (Fig. 3.26b). Note that, if the three strongest landfalling TCs are excluded, JTWC will give the same behaviour as in other datasets.

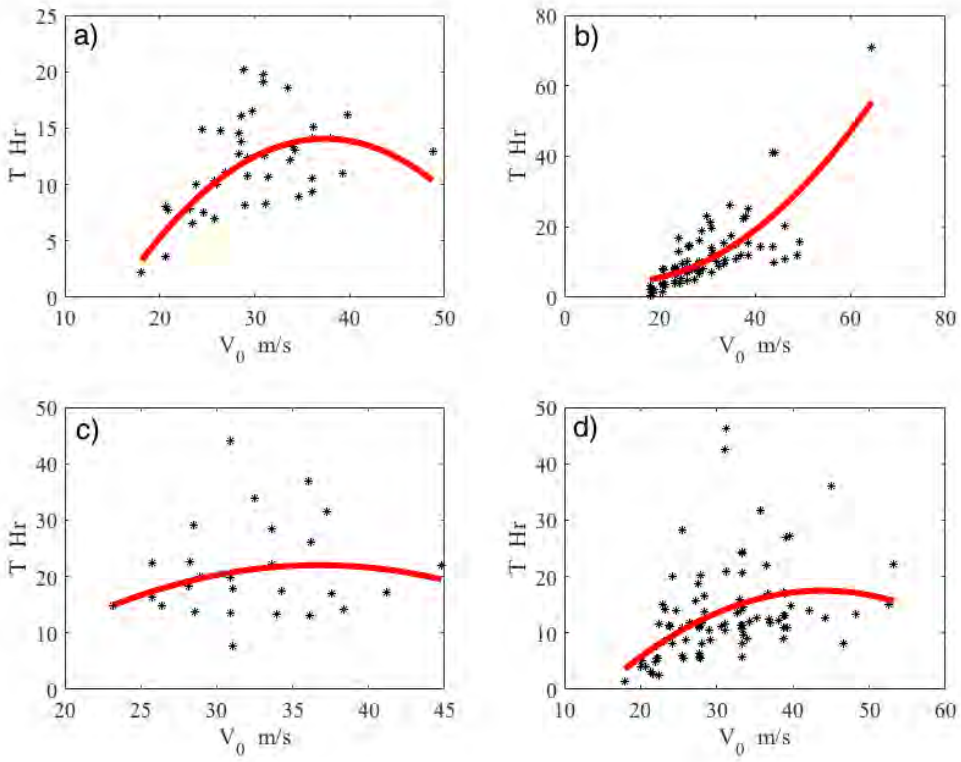

Figure 3.27: Fitted relations between TC landfall intensity and sustaining time after landfall. Results based on data from (a) HKO; (b) JTWC; (c) RSMC and (d) CMA. Black asterisks denote those for are the scatterings of all the selected TCs, and the red solid lines are the best fit results based on quadratic fits.

The PDI values over land, with the new estimates, is shown in Fig. 3.28. The red lines denote the best cubic fits. HKO and RSMC show relationships being close to linear,

because τ decreases faster with V_0 (see Figs. 3.26a and 3.26c). For JTWC and CMA, PDI increase faster than the first power of V_0, as a result of weaker τ-V_0 relation (see Figs. 3.26b and 3.26d). This is especially clear for JTWC, which shows a dramatic increase of PDI with very strong landfall intensity. Again, by removing the the three strongest landfalling TCs, the PDI-V_0 relation will become more linear.

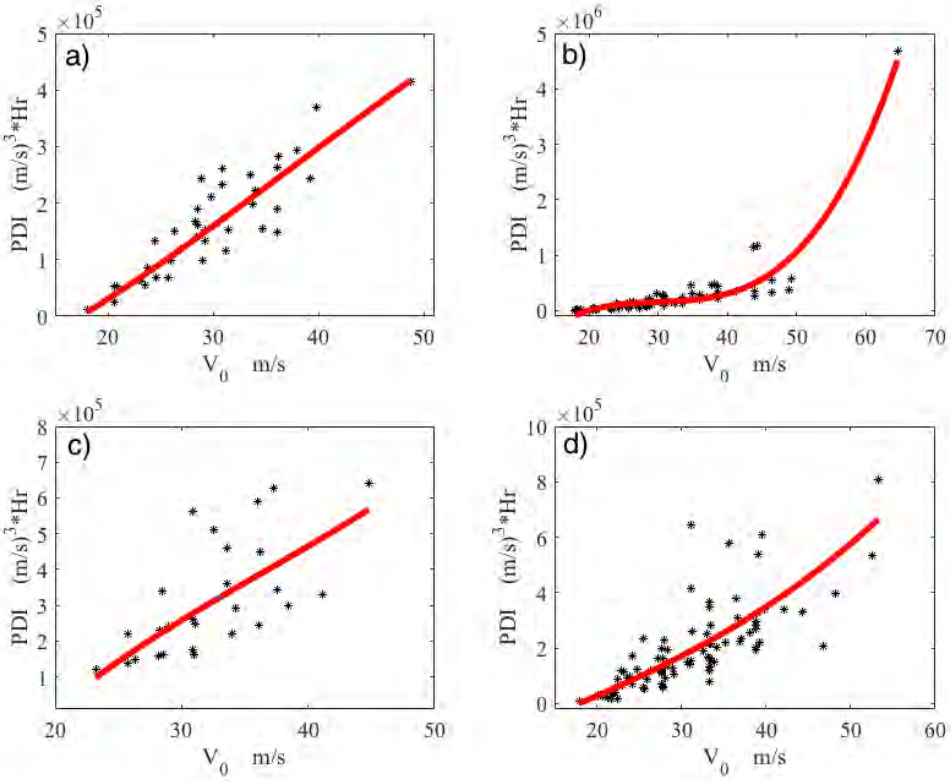

Figure 3.28: Relationship between PDI over land and TC landfall intensity based on data from (a) HKO; (b) JTWC; (c) RSMC and (d) CMA. Black asterisks denote those for are the scatterings of all the selected TCs, and the red solid lines are the best fit results based on cubic fits.

To summarize, TCs with stronger landfall intensity may decay faster per unit time,

compared with weaker storms. As such stronger TCs may not sustain substantially longer over land. On the other hand, PDI over land increase linearly. Combining these results, strong TCs may have much stronger influences on coastal regions as their intensity increases (say due to global warming), but these systems may not travel (and influence) much farther into more inland locations.

One consideration of the discussed relations may be important in the future climate. As the supposed stronger landfall intensities under global warming condition, more TCs could pass some critical landfall intensity with stronger PDI but shorter sustaining time or just similar with historical cases, which cannot go as far as expected, and these shorter sustaining TCs with stronger PDI will make stronger influences on coastal regions than expected.

Chapter 4

Future projections of WNP TC activities and influences on East Asia coastal regions based on AGCM

As indicated in Chapter 3.4, stronger landfall intensity can lead to longer life time and stronger influences of TCs over inland areas. The last 50 years have seen an increase of TC landfall intensity and more serious threats to East Asia inland locations. It is therefore essential to understand how TC, will change under global warming, as well as the influences of storms on the East Asian coast.

This Chapter makes use of the MRI-AGCM3.2s to evaluate the change of WNP TCs and the impacts on land areas in a warmer future. As described in Chapter 2.2.4, MRI-

AGCM3.2s is a 20 km global model, and it can reproduce realistic East Asian summer monsoon and precipitation features around the tropical Western Pacific and the global distribution of TCs in its model environment[131]. The future climate in 2075-2099 were projected, based on forcing due to future SST changes projected by the CMIP3 multi-model dataset for A1B scenario, superimposed onto observed climatological SST.

4.1 TC tracking algorithm

The algorithm for the detection of TCs from the 6-hourly AGCM outputs is similar to that used by Murakami ***et al.***[172]. A TC-like system in the model is identified whenever: (1) the local maximum 850 hPa vorticity exceeds $2.0 \times 10^{-4} s^{-1}$; (2) the local maximum wind speed at 850 hPa is greater than $17.0 m/s$; (3) the sum of maximum temperature deviations at 300, 500 and 700 hPa exceeds $2.0K$, with the deviation defined as the departure from temperature averaged over a $10^o \times 10^o$ box centered at the position of maximum 850 hPa vorticity; (4) the maximum 850 hPa wind speed is larger than that at 300 hPa; and (5) the lifetime of the system must be 36 hours or more and the genesis must happen over the ocean.

4.2 Model evaluation

4.2.1 TC genesis and development

Comparing the TC-like systems in this model with observations, it is found that the MRI-AGCM3.2s gives the annual mean tropical-cyclone genesis number of 26.6 in WNP, which is close to the observed value 26.1[131]. It is worth noticing that the model output used is confined to the domain of $0^o - 60^oN$, $60^oE - 150^oE$, and temporally from May to September. Some TCs can be generated east of 150^oE, or in April or after October, so the number of TCs can be less than that throughout the year in WNP. Compared to JTWC best track data, MRI-AGCM3.2s can reproduce WNP TC genesis locations well. Lue et al. found that the MRI-AGCSM model can reproduce TC frequency in WNP during MJJAS season, though the genesis frequency in the South China Sea is underestimated[173]. For instance, result for the 1979-2003 is shown in Fig. 4.1b, in which the genesis frequency is calculated over $5^o \times 5^o$ grid boxes per TC season, the same as in Fig. 4.1a. Compared with the observations, MRI-AGCM3.2s can well replicate the genesis near the Philippines, albeit with a slight eastward shift. However, the TC number in South China Sea is underestimated, as can be seen from Fig. 4.1b.

The MRI-AGCM3.2s simulated TC intensity was reported to be weaker than the observed[131]. Fig. 4.2 shows the PDF of TC life-time peak intensity from observation (solid black line) and MRI-AGCM3.2s (dashed red line). The model gives two peaks in probability, namely at 20 m/s and at 65 m/s. This is in contrast with the observed PDF,

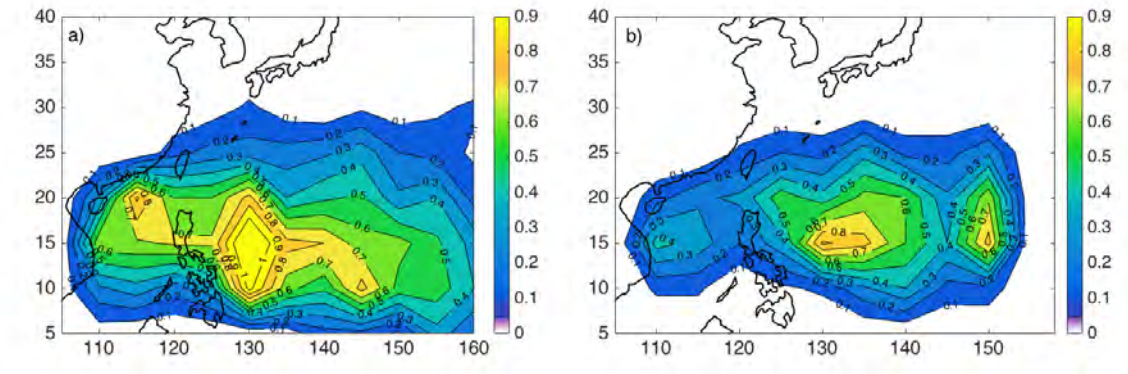

Figure 4.1: Spatial distribution of TC genesis over each $5^o \times 5^o$ grid box frequency in WNP from 1979 to 2003 (Units: number of TCs per year) based on data from (a) JTWC; (b) MRI-AGCM3.2s.

which gives a single maximum probability at about 25 m/s. This suggests that this model tends to over produce weak and strong TCs, under producing storms of moderate strength in WNP.

4.2.2 Decay process after landfall

As indicated in Chapter 3.5, stronger WNP TCs are observed to decay faster than weaker ones after landfall. The simulated WNP landfalling TCs in MRI-AGCM3.2s also show similar results. Applying the same criteria as in Chapter 3.5, 22 WNP landfalling TCs are selected in the period of 1979-2003 (see Fig. 4.3(a)). The time scale (τ) of these 22 TCs decreases as landfall intensity increases, using the empirical decay model (see Fig. 4.3(b)). There is also a quasi-linear relationship between PDI over land (Fig. 4.3(c)) and the landfall intensity (Fig. 4.3(d)).

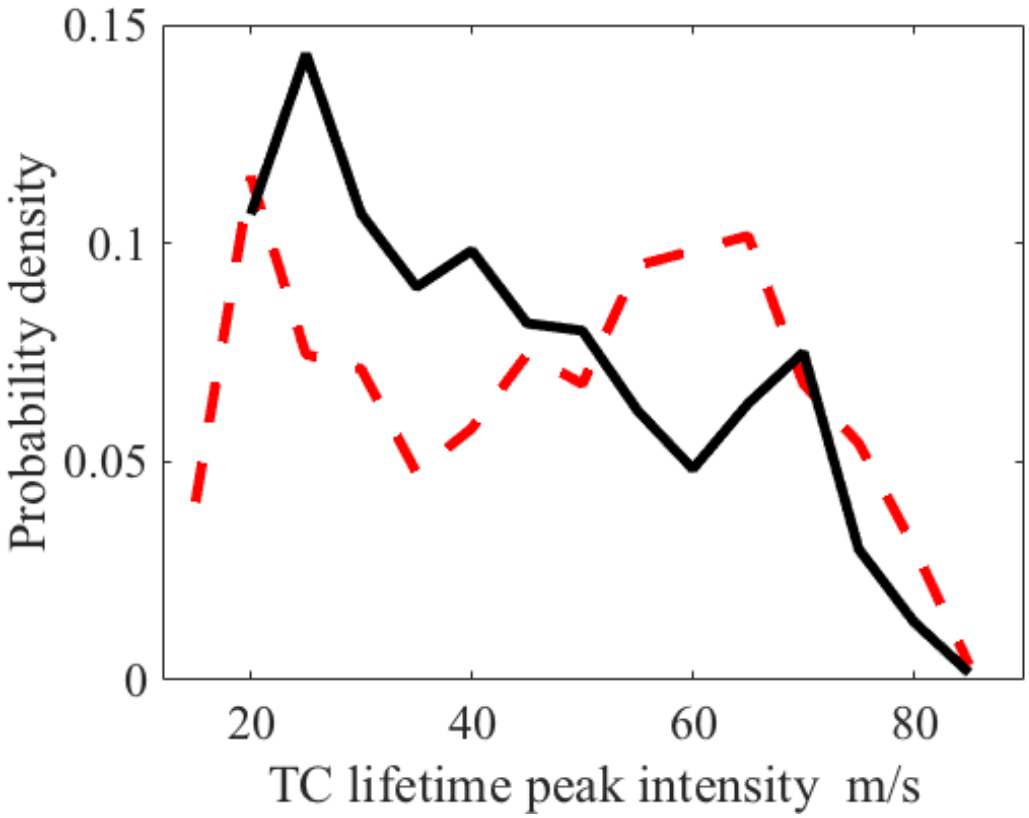

Figure 4.2: PDF of WNP TC lifetime peak intensity (Units: m/s) in JTWC (solid line) and MRI-AGCM3.2s simulations (dashed line).

However, in the future period of 2075-2099, the relationships discussed before seems to be changed when compared to the 1979-2003 period. In the future, the previous observed negative relationship between time scale and landfall intensity is not obvious (see Fig. 4.4(b)). Sustaining time after landfall (Fig. 4.4(c)) might even increase slightly as V_0 increase.Moreover, the fitted relation between landfall intensity and PDI over the land becomes non-linear(Fig. 4.4(d)).

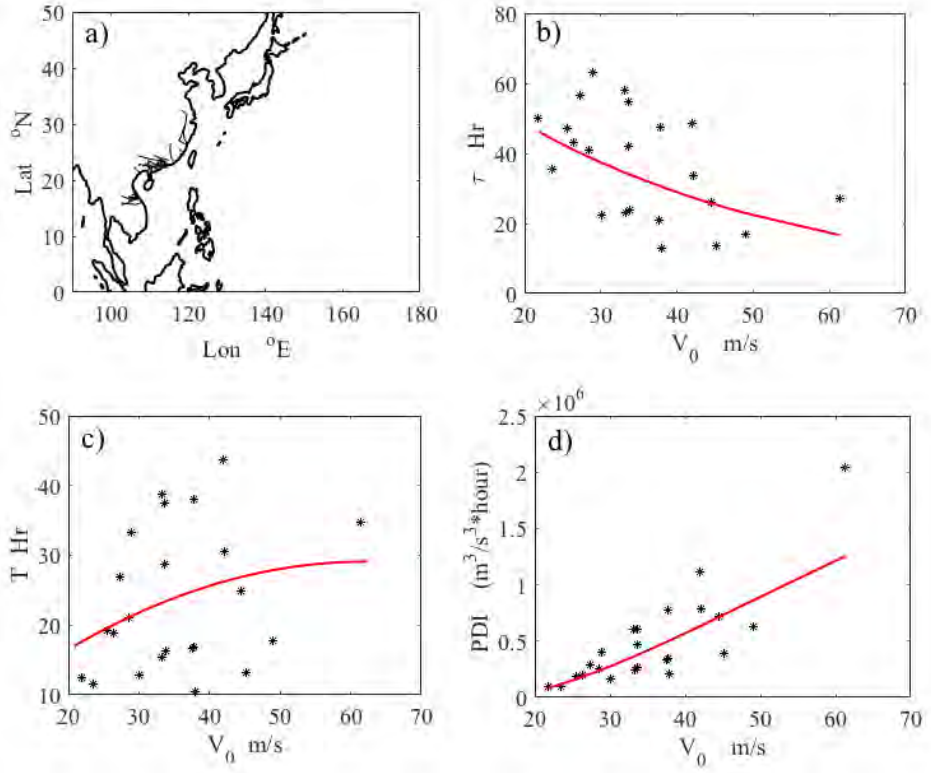

Figure 4.3: Fitted decay process for the WNP landfalling TCs in MRI-AGCM3.2s in the period of 1979-2003. (a) Track information of selected WNP landfalling TCs. (b), (c) and (d) are the fitted relationships between TC landfall intensity and time scale factor τ, sustaining time after landfall and PDI over the land, respectively.

4.3 Projected influences of WNP landfall TCs over inland area

Comparing the 2075-2099 and 1979-2003, MJJAS mean SST is projected to increase by about 2-2.5 ^oC in WNP according to the SRES A1B scenario CMIP3 model results (Fig. 4.5). Land surface is warming more than the ocean, with the strongest temperature increase reaching about 5 ^oC over the western part of Asia. Focusing on the WNP region where

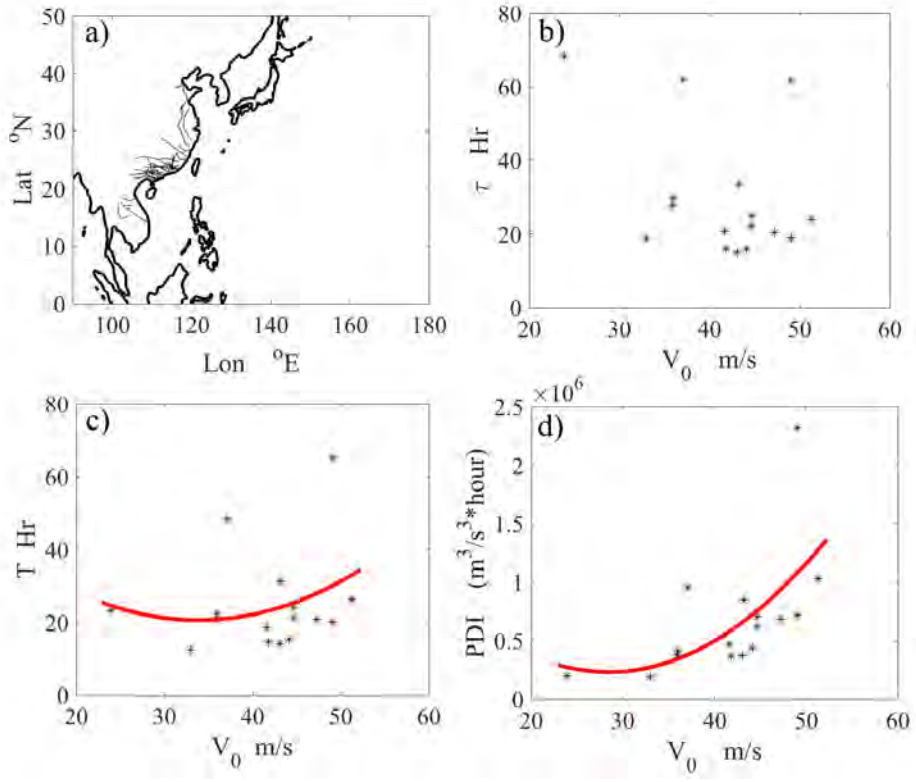

Figure 4.4: Same with Fig. 4.3, but in 2075-2099 period.

TCs are active (see the dashed grey box), the area averaged increase of SST is expected to be about 2.2 ^oC.

In the response to the 2-5 ^oC warming, the behaviour of WNP TCs is changed. First, the TC number is reduced, from 11.8 per year in the historical experiment to 8.8 in the future. Fig. 4.6 shows the genesis frequency per year in the historical run (Fig. 4.6a) and future projections (Fig. 4.6b). It is clear that TC genesis frequency is reduced in almost everywhere in the basin.

To further understand this, Lui et al.[173] suggested the reduction of the TC frequency

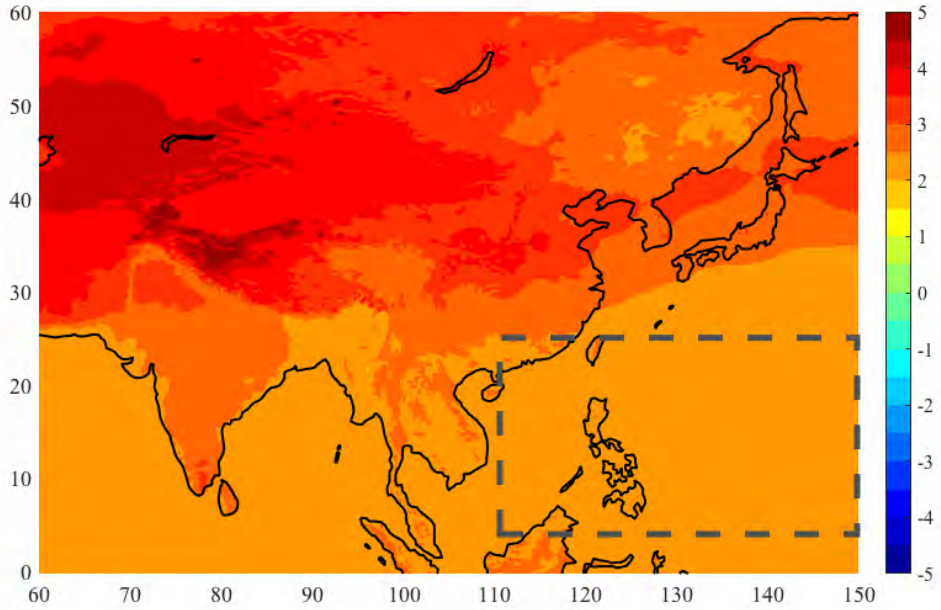

Figure 4.5: Surface temperature change (Units: K) between the periods of 2075-2099 and 1979-2003, based on CMIP3 multi-model MJJAS mean for the SRES A1B scenario.

is related to the sinking motion and low- level anticyclonic circulation over South China Sea and east of the Philippines. Applying the difference of the MJJAS mean of 850 hPa vorticity and the vertical wind shear between the 2079-2099 and 1979-2003 simulations, it can be seen from Fig. 4.7b that the wind shear is slightly reduced over the region of $135^oE - 150^oE$. On the other hand, the 850 hPa vorticity is also largely reduced near the Philippines (Fig. 4.7a), where a strong reduction of TC genesis frequency is also found (Fig. 4.6c). A clear anti-cyclonic wind anomaly can be seen in the area of vorticity reduction.

Although the TC frequency is projected to decrease, the landfall intensity of WNP TC

is found to increase by about 3 m/s, by comparing the future projection and historical run (see Fig. 4.8d). However, it is noteworthy that this increase of landfall intensity didn't pass student test at 0.1 significance level.

The influence of global warming on WNP TCs making landfall in East Asia coastline is then examined. Here the TC selection criteria is similar to that used in Chapter 3.2, but without the limitation of peak intensity greater than 34 m/s. After the storm selection, TCs' landfall intensity, sustaining time over the land, translating distance over the land and PDI over the land are calculated. Results are shown in Fig. 4.8. The sustaining time over land is projected to increase by 6 more hours (or increment of 25.8%), passing the 5% significance level. TCs also travel 130 km longer (or 35% fractional increase) over the land, while the PDI over the land can increase $3 \times 10^4 (m/s)^3 * hour$ (42% fractional increase) in the globally warmed future.

In addition, we have also computed the TC frequency passing each $2^o \times 2^o$ grid box over the WNP/East Asian domain. The difference between 2079-2099 and 1979-2003 simulations is shown in Fig. 4.9. It can be seen that TC frequency is reduced almost everywhere in WNP due to the remarkable suppression of TC genesis (see Fig. 4.6). TC frequency along the Asia coastline also shows a depletion in the warming future. However, the occurrence is enhanced over more inland areas in East Asia, especially in inland Eastern China. The increase in frequency means that there will be approximately 1 more storm found in inland areas every 2 to 3 years, due to the longer lifetime or distance trav-

eled by these systems over land.

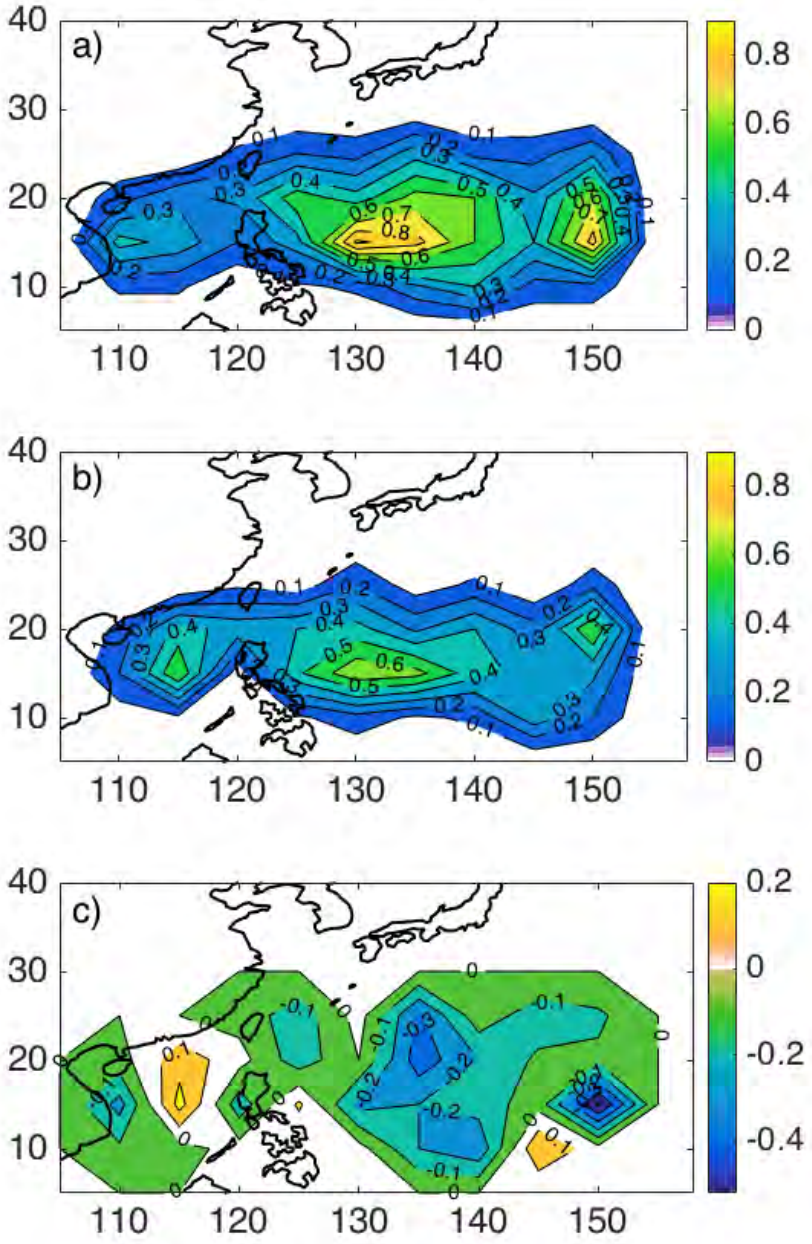

Figure 4.6: Spatial distribution of TC genesis over each $5^o \times 5^o$ grid box frequency in WNP in (a) historical run and (b) global warming run and (c) the frequency difference between the two sets of experiments.

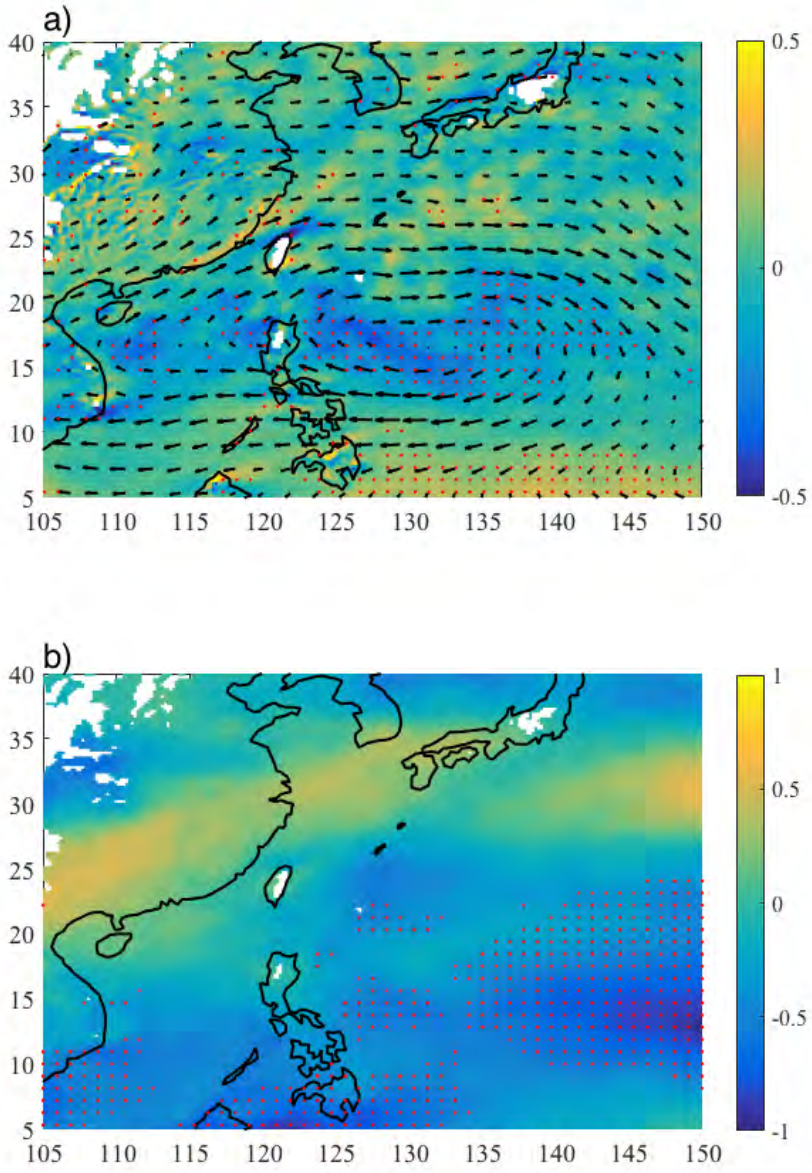

Figure 4.7: The difference of (a) 850 hPa vorticity (Units: S^{-1}) and (b) wind shear (m/s) between 2075-2099 and 1979-2003 in MJJAS mean based on the simulations of MRI-AGCM3.2s. The red dots are the 0.05 significance level, and the vectors in (a) are wind anomaly between global warming experiments and historical runs in MRI-AGCM3.2s.

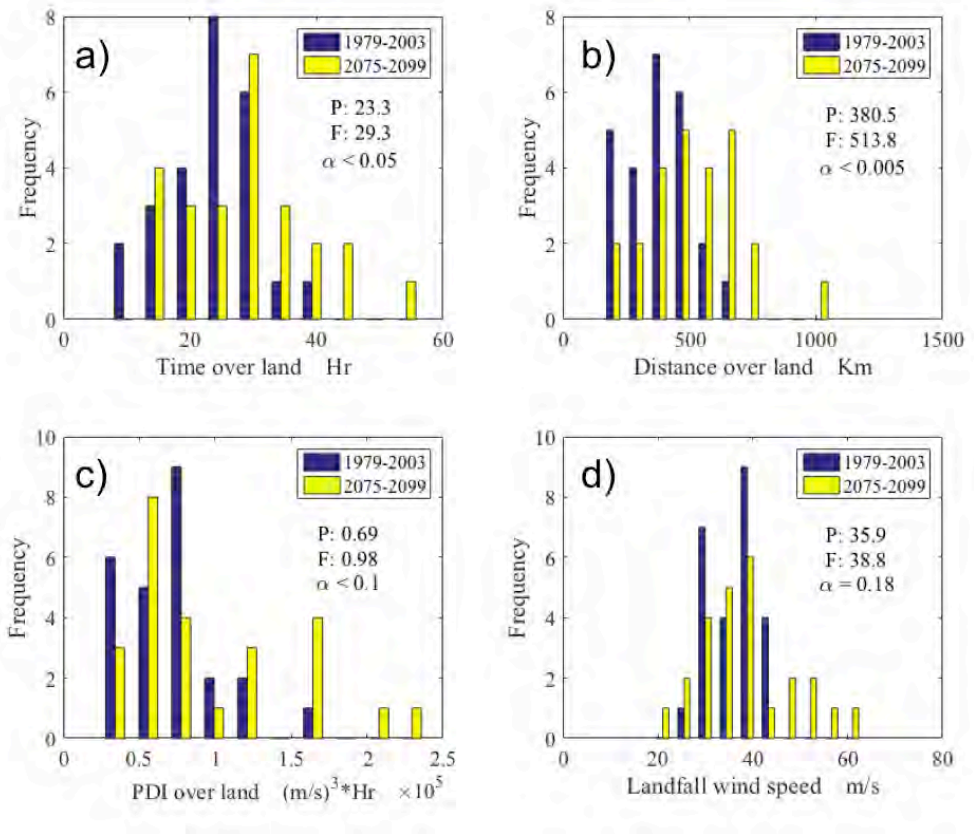

Figure 4.8: Frequency distributions of four TC landfall indices in 2075-2099 (yellow bars) and 1979-2003 (blue bars) from MRI-AGCM3.2s model outputs. (a) Time over the land; (b) Distance over the land; (c) PDI over the land and (d) Landfall wind speed.

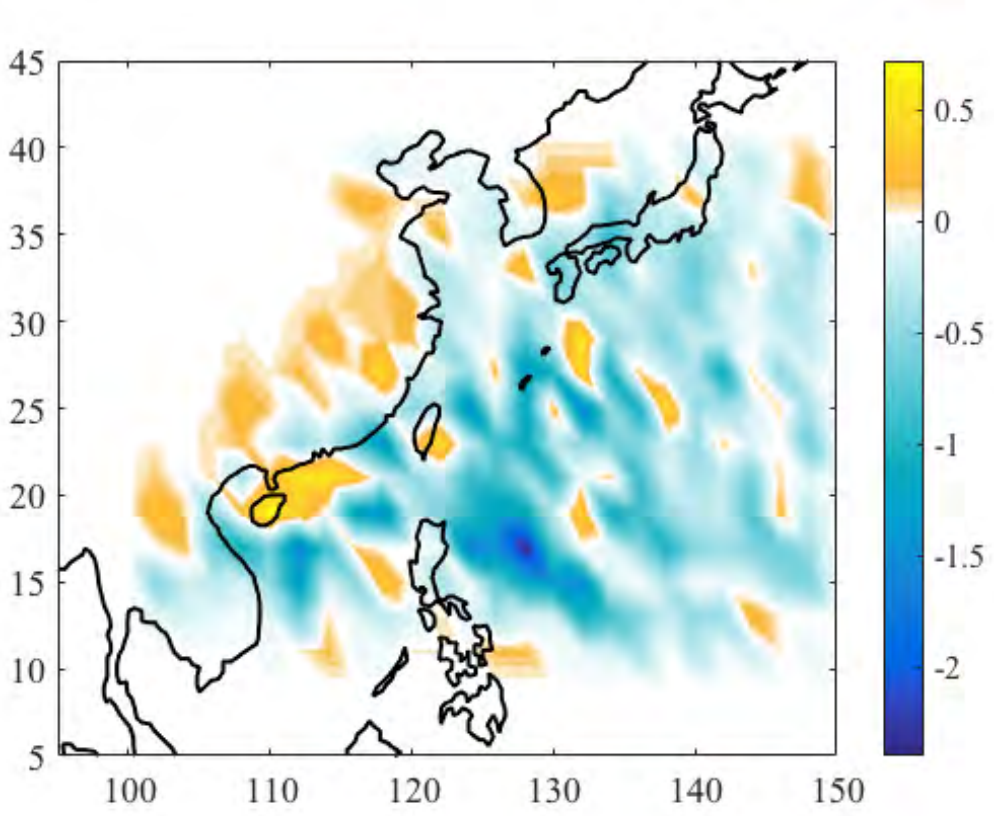

Figure 4.9: Spatial distribution of TC frequency change over each $2^o \times 2^o$ grid box frequency in WNP between the two sets of experiments.

Chapter 5

Future Projections of WNP landfalling TCs and their influences on the PRD region based on PGW method

WNP TCs projections in the 2075-2099 period according to the SRES A1B scenario have been examined in Chapter 4. It was found that WNP TC landfall intensity might be enhanced by about 3 m/s under a warmer climate, based on projections by the MRI-AGCM3.2s model. However, the 20 km global model's resolution is still too coarse to resolve detailed structure of TCs, such as TC eyewall, rainband distribution and mesoscale circulations (see Chapter 1.3). In this chapter, the PGW method (see Chapter 2.4.2) is applied to evaluate the impacts of global warming on WNP landfall TCs and the induced

storm surges, using the high resolution (15-3 km) WRF (Chapter 2.2.3) and SLOSH model (Chapter 2.2.4). Here the focus is on the PRD region. 20 intense tropical storms that brought the highest storm surges in Hong Kong waters are selected, and changes in maximum wind speed, storm size, rainfall and induced storm surge are examined.

5.1 Simulated historical TCs and storm surges

This section focuses on WRF and SLOSH model evaluations. To test the performance of the two models, the simulated and observed TC structures, tracks, intensities and induced storm surges are compared.

5.1.1 WRF simulations of 20 historical TCs

In general, it is found that WRF can reasonably capture the structure of a TC. The WRF-simulated circulation for TC Hato (2017) is shown in Fig. 5.1. Typical features such as the low minimum surface pressure at the TC center, as well as a warm core which is about 8 ^oC warmer than the surrounding from 850 hPa to 200 hPa (Fig. 5.1a), are well reproduced. Fig. 5.1b shows the vertical distribution of the wind speed, with the strongest wind occurring at around 50 km , which is the RMW, from the TC center. Note that the wind to the right part of TC center is stronger than the that in the left, because large scale background low-level flow is to the northwest. It can be inferred that humidity (see Fig. 5.1b) converges and rises to the upper levels near the RMW, with deeper convection to the

left part of the TC center. Due to the southerly monsoon flow, which brings moisture to the storm, the southwest quadrant is wetter and with stronger moisture convergence. Fig. 5.1c shows the near surface wind of the storm, with cyclonic flow at a relatively low wind speed near the TC center, and strongest wind speed at RMW. From Fig. 5.1d, it can be seen that the typical eye structure and rain band are also well captured.

To make a further investigation, simulated biases of TC tracks and intensities, are considered. The intensity is measured in TC's 10-meter maximum wind speed. The track bias is calculated by taking the average of perpendicular distance between the WRF simulated track and the HKO best track over the ocean (see Appendix C.1). The intensity bias is defined as the difference between the storm lifetime peak intensities from WRF and the HKO data. As shown in Fig. 5.2, WRF can capture the TC tracks very well, with track a bias of 40.4 km, based on average over those 20 TCs. TC cases after 1979 tend to give a smaller track bias (34.7 km) than those before 1979 (53.8 km) (Fig. 5.2a). It can also be seen from Fig. 5.2b that WRF can simulate TC's peak intensity with fractional error of about -13.8% to 20.7% based on two standard deviation of model bias. Overall, the model gives an 3.5% overestimation of TC intensity. It can be said that WRF can well simulate the 20 historical TCs, with reasonable TC structures, accurate tracks and slightly overestimated intensities.

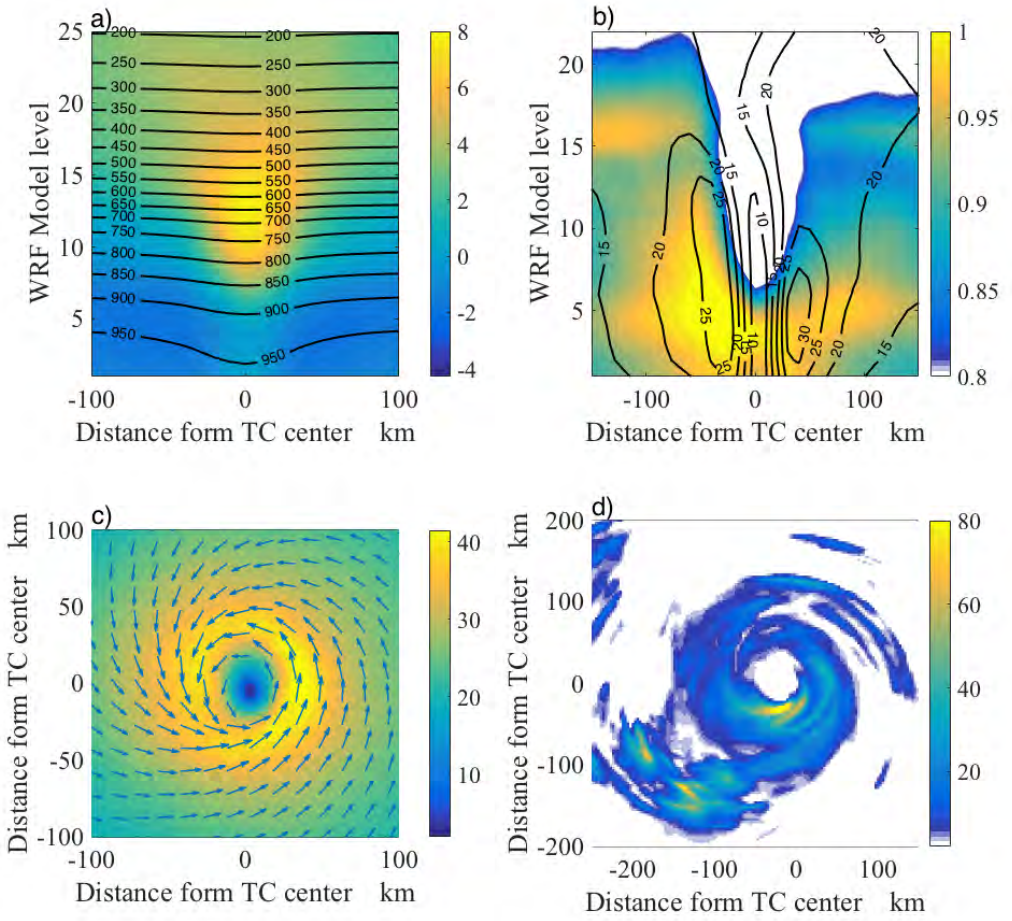

Figure 5.1: TC Hato (2017) based on WRF simulation. Vertical cross section of (a) pressure (contours, Units: hPa) and temperature anomalies (shading, Units: K); (b) wind speed (contours, Units: m/s) and RH (shading); (c) near surface wind(Units: m/s) and d) hourly mean precipitation (mm/hour).

5.1.2 Evaluation of SLOSH simulations of historical storm surges

Storm surges reproduced by SLOSH are also evaluated. Observations from six tide stations in Hong Kong, namely Tai Po Kau, North Point, Quarry Bay, Tsim Bei Tsui, Waglan Island and Shek Pik are used for this purpose. The locations of those stations are shown

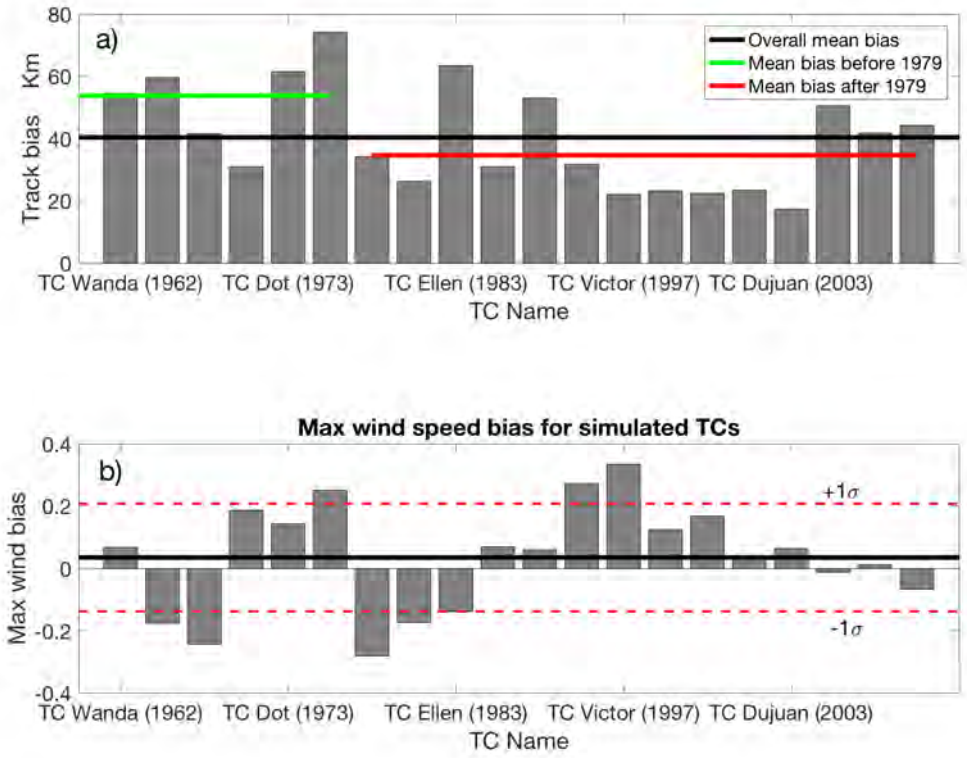

Figure 5.2: Model bias in TC simulations, relative to HKO best track data, for (a) TC track bias, with black line denoting the overall mean, while green and red lines the averages before and after 1979, respectively and (b) TC lifetime peak intensity bias, with the black line denoting the mean bias, together with ± 1 sigma uncertainty enclosed by the dashed red lines.

in Fig. 2.4b. Table 5.1 gives the observed and SLOSH simulated storm surge magnitudes. It can be seen that surges associated with less than 4 TCs were recorded by Waglan Island station and Shek Pik station, which is not enough for statistics analysis. For the other 4 stations, SLOSH could simulate the surges heights with -20% to $+10\%$ of relative error.

Table 5.1: Observed and simulated storm surges at tide stations in Hong Kong. Individual storms are represented by TC numbers. The observed and simulated height at one station are computed from averaged storm surge magnitude induced by all the recorded TCs. S/O represents the ratio of SLOSH simulated heights to observed heights

Station	TC number	Observed height (m)	Simulated height (m)	S/O
Tai Po Kau	19	1.62	1.79	1.11
North Point	7	1.22	1.32	1.08
Quarry Bay	12	0.99	0.88	0.89
Tsim Bei Tsui	9	1.21	0.97	0.80
Waglan Island	2	1.05	0.83	0.79
Shek Pik	3	0.85	0.55	0.64

5.2 Changes of TCs and induced storm surges in PGW experiments

5.2.1 Intensified TC winds

The change of TCs peak intensity during 2075-2099 period can be inferred by comparing PGW experiments with the historical runs, and the results are shown in Fig. 5.3. It is found that almost all 20 historical TCs are intensified, with a systematic increase of 7.5% (9.4%) in the parent (daughter) WRF domain. Landfall intensity is enhanced by as much as 11.4% in the daughter domain (Fig. 5.3b). A ratio of intensification, defined as $(In_{pgw} - In_{his})/In_{his}$ for each individual TC, where In_{pgw} is the intensity in the warming experiments, and In_{his} is the Intensity in the historical runs, can be computed. The SST is projected to increase by 2.76 K in WNP, based on the CMIP5 multi-model average according to the RCP 8.5 scenario. This implies $\sim 3.4\%$ peak intensity change per degree K

of SST warming, which is consistent with previous studies[174]. Despite the systematic intensification, different TC can response to the PGW rather differently. Some TCs can be intensified greatly, while others are not obviously strengthened. This large fluctuation in response to PGW might be related to individual TC's background vertical wind shear, as will be demonstrated later. When the background vertical wind shear is weaker, the storm also tends to be intensified more in the PGW experiment. This will be shown in Chapter 5.3.

5.2.2 RMW and storm size

Two kinds of storm sizes are considered, namely RMW and the area where TC wind is stronger than 17 m/s (A17). Here we just consider the parent domain results, because the daughter domain just spans about 1200 km in the south-north direction, which is comparable to the typical size of a TC. It can be seen from Fig. 5.4a that RMW is reduced by 7.4% on average in the PGW experiments, making the eyes of TCs become smaller in the warmer future. On the other hand, the A17 is found to increase by about 10% when TCs are close to the coastline (3 to 12 hours before landfall, seeing Fig. 5.4b). Finally, TC potential dissipating power within A17, calculated by integrating v^3 in all A17 ($\int_{A17} v^3 dA$), is found to increase 18.4% near landfall (Fig. 5.4c) in a warming climate.

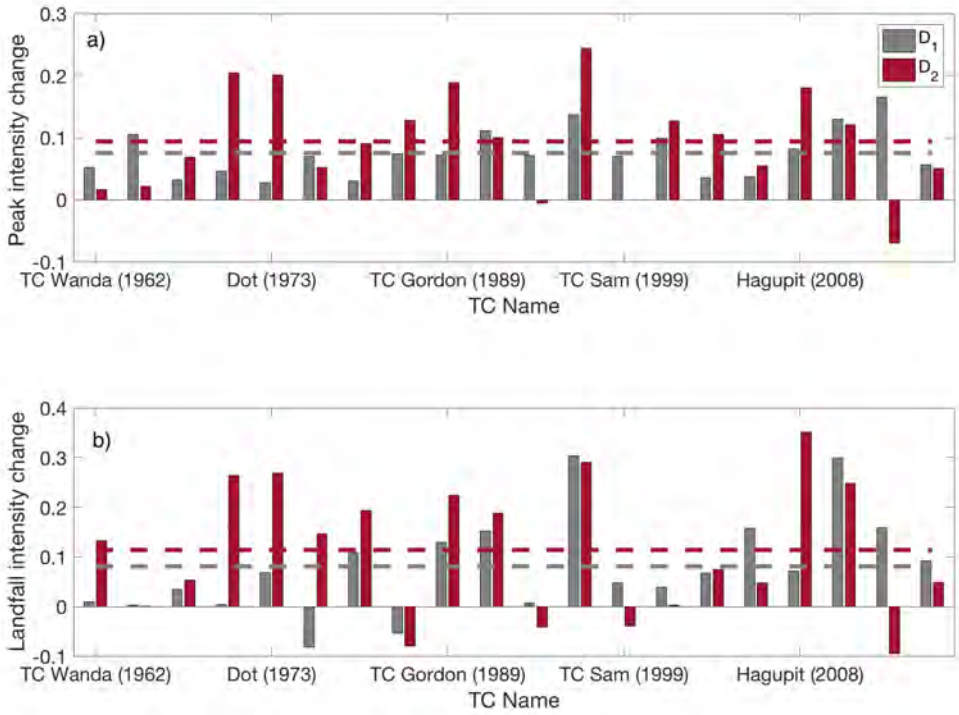

Figure 5.3: Projected rate change of (a) TC peak intensity and (b) landfall intensity in 2075-2099 according to the RCP 8.5 scenario, relative to those in the present climate. Grey bars represent the parent domain results and red bars represent those from daughter domain. Dashed lines indicate the mean increasing rate for the corresponding domains.

5.2.3 TC precipitation

TC related extreme rainfall is also expected to become heavier with a warmer background climate. The 3-km resolution experiments reveal substantial increase in storm-induced rainfall, with 19 of the 20 TCs' rainfall rate in the PGW experiments being higher than that in the historical runs (Fig. 5.6b). Fig. 5.5a shows the PDF of the TC rainfall from the PGW and historical runs. Probability of heavy precipitation related to TCwill be enhanced,

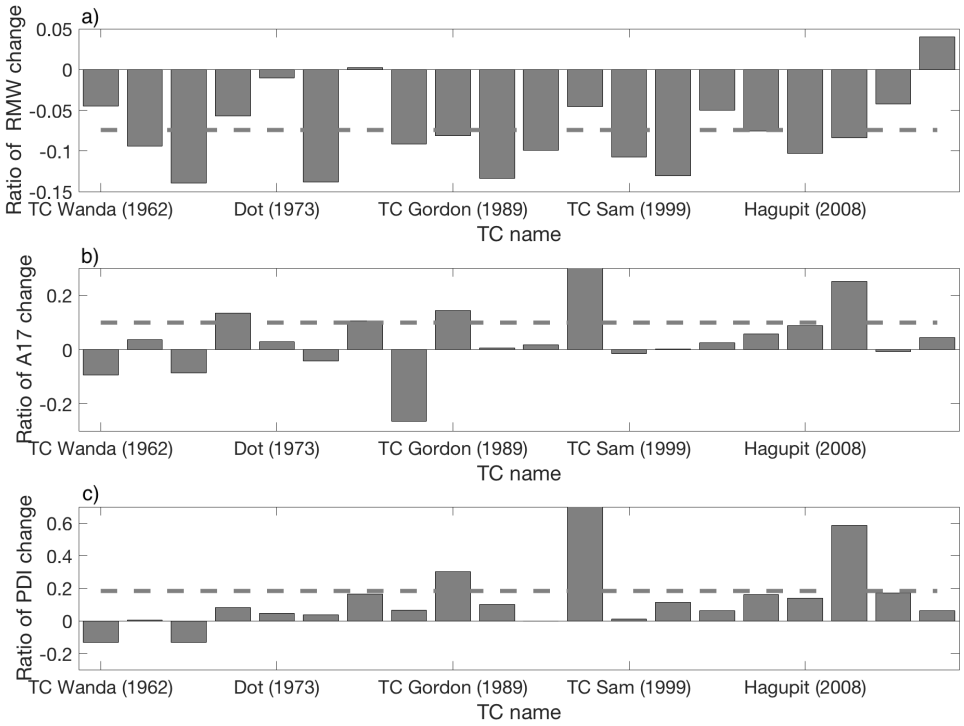

Figure 5.4: Same as Fig. 5.3 except for a) RMW; b) A17 and c) Potential dissipation within A17.

while that of precipitation less than 10 mm/hr will be largely reduced. There is also robust increase of probability for rain rate above the 95^{th} percentile. Fig. 5.6a displays the 20 TCs average rainfall change in due to global warming. TC rainfall is largely increased in most of the storm area, with the largest increase near RMW. Precipitation change in this region near RMW, for each storm, is further shown in Fig. 5.6b. There is an increase of about 22% of extreme precipitation under the warming climate, which is comparable to projections from the IPCC AR5 report[56]. Based on the 2.76 K increase of SST, the sensitivity of extreme precipitation rate to SST warming is 7.97% $/^oC$, which is close to the 7% increase

per degree of warming as expected from the Clausius-Clapeyron relation[174, 175].

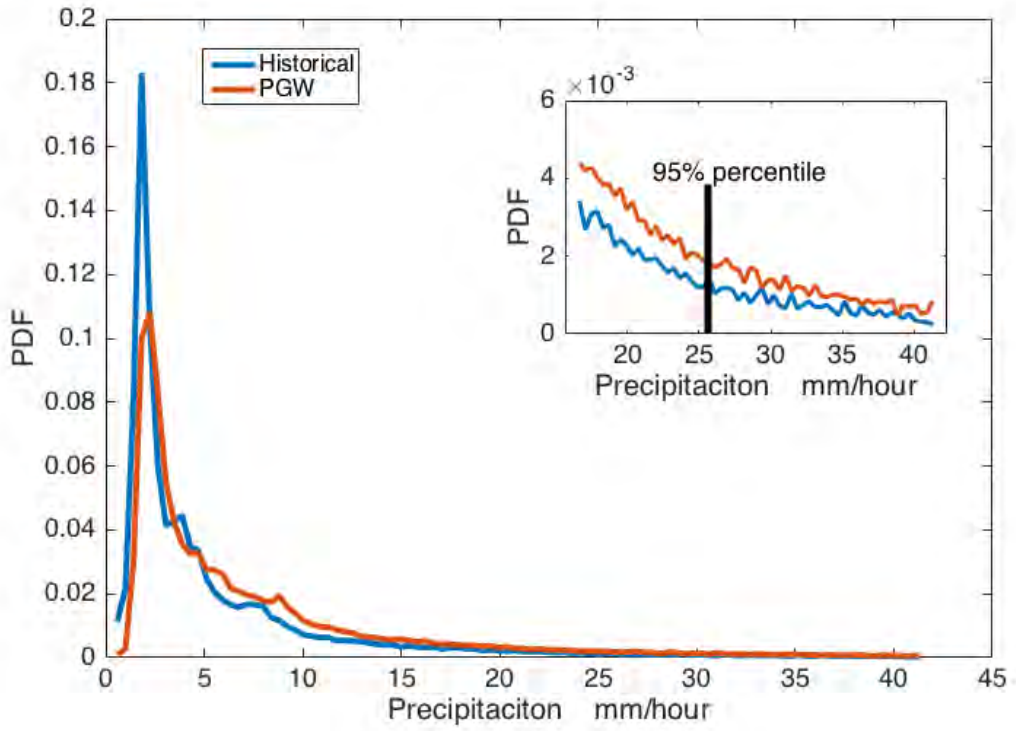

Figure 5.5: PDF of composite TC hourly precipitation (mm/hr) in the historical simulation and that in the PGW runs. Smaller box is the PDF illusion focusing on 95% percentile precipitation based on historical experiments.

5.2.4 Induced storm surges

The storm surge change related to the 20 TCs in PGW experiments is now considered. Surge heights of four stations in Hong Kong, namely Tai Po Kau, North Point, Quarry Bay and Tsim Bei Tsui are examined. For Waglan Island and Shek Pik, are excluded for the reason that not enough TCs cases recorded (see Table 5.1). It should be noted that there

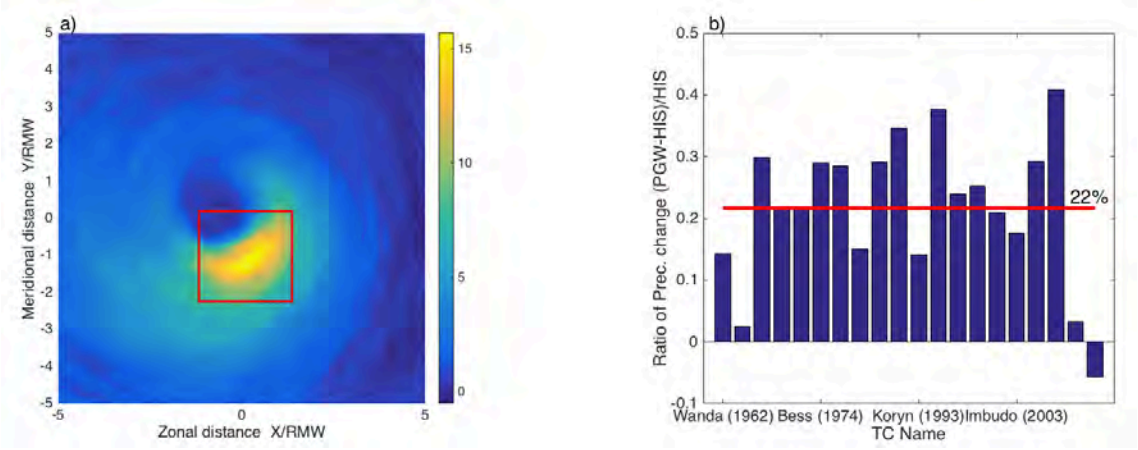

Figure 5.6: (a) Difference between TC rain rates in the PGW runs and those in the historical simulations (mm/hr). (b) Rate difference in precipitation near RMW for each TC.

is a systematic bias between SLOSH simulated and observed storm surge height (see Table 5.1 S/O ratio); projected change of storm surge magnitude by SLOSH, therefore, might not be the best way to project surge changes realistically. Here the projected change of the storm surge height is computed by first calculating the fractional change of surge height in SLOSH. Such a fraction is then multiplied by the observed historical surge amplitude, in order to project the future surge value for a particular storm. To project the storm surge change, the fractional surge height change between PGW and historical simulations by SLOSH is calculated as $S_{rate} = (S_{pgw} - S_{his})/S_{his}$, where S_{rate} represents the fractional change of surge simulated by SLOSH, while S_{pgw} is the surge amplitude in PGW run, and S_{his} is the surge height in the historical run. The storm surge change projection can then be estimated by $S = S_{obs} \times S_{rate}$. Fig. 5.7 shows the surge changes at the four selected stations. All the four stations will experience higher storm surges in the late of 21 century

under a warmer climate. In particular, the storm surge will increase by 14.7 cm, 15.6 cm, 9.4 cm and 38.5 cm at Tai Po Kau, North Point, Quarry Bay and Tsim Bei Tsui station, respectively, based on the average over all the TC cases. Although the mean increase of maximum storm surges is not strong, large increments can be found in some cases. In fact, for more than 20% of the storms, the surge height can increase by 40 cm or more at all stations (except Quarry Bay). For Super Typhoon Hope (1979), the increase could be more than 1 m (Fig. 5.7a). For TC Molave (2009), the increase can be more than 2 m in the Tsim Bei Tsui station (see Fig. 5.7d).

5.3 Responses of TCs to various background conditions

In spite of the overall change of TCs intensity, storm size, rainfall distribution and storm surge, it can also be seen that different TCs can response to global warming very differently. Specifically, changes of TC lifetime peak intensities in the PGW experiments can fluctuate greatly (see Fig. 5.3). Since all the TC cases are experiencing similar PGW signals, the large fluctuation is likely related to the different background conditions for each TC. Four factors, namely background SST, 850 hPa vorticity, environmental vertical wind shear and background 600 hPa relative humidity (RH) are examined so as to better understand such a variation.

Stepwise regression analysis is applied to test the importance of these four factors on the response of TCs to PGW.The method is expected to shed light on how TC responds

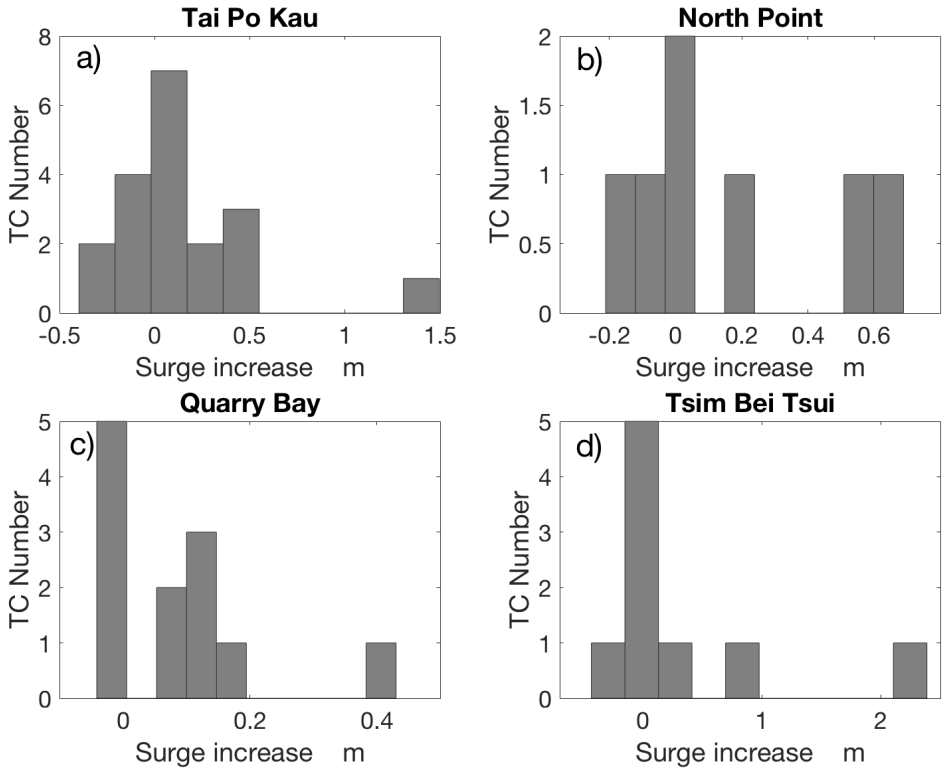

Figure 5.7: Frequency distribution of projected storm surge change (m/s) in the PGW relative to the historical simulations at (a) Tai Po Kau; (b) North Point; (c) Quarry Bay and (d) Tsim Bei Tsui staton.

to those background environmental factors individually. In this method, the 20-points intensity intensification series shown in Fig. 5.3, in which changes of intensity of 20 TCs are first recorded. The lifetime temporal mean of background SST, 850 hPa large scale vorticity, vertical wind shear and 600 hPa RH field are then calculated, for each of the 20 TCs. Stepwise regression maps of the 4 environmental factors onto TC intensification are shown in Fig. 5.8. It is noteworthy that for the vorticity, wind shear and RH, TC-related signals are removed with a 500 km-radius disk around the TC center. Shading in Fig. 5.8

indicates signals within the 0.1 significance level. It can be seen that TC's background vertical wind shear plays the most important role, for the reason that significant regression is found along the storm tracks and over locations with the strongest TC intensities (red circles in Fig. 5.8a). Background SST and 600 hPa RH also play important roles. The above results highlight that intensifications of TCs under PGW is sensitive to various background environmental factors, with background vertical wind shear being the most important one. TCs under a weaker vertical shear background tend to be more intensified than others.

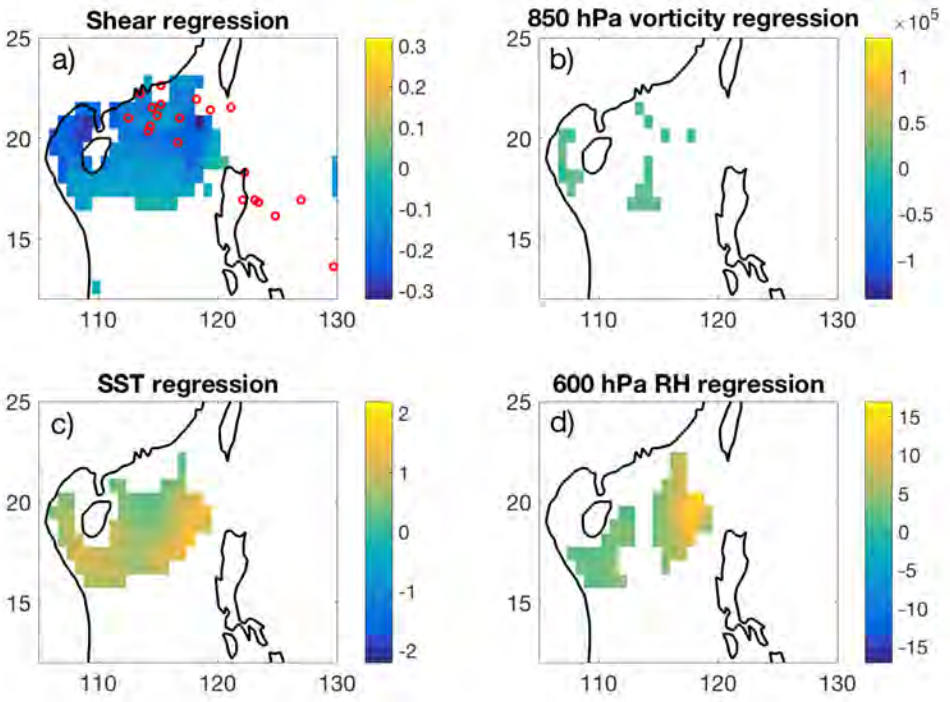

Figure 5.8: Stepwise regression map of (a) background wind shear (Units: m/s); (b) background 850 hPa vorticity (Units: S^{-1}); c) background SST (Units: K) and d) 600 hPa RH (Units: %) onto the TCs' peak intensity change in the PGW runs relative to the historical simulations. Shading denotes the regression values above 90% confidence level, and red circles in (a) are the locations where TCs achieve their peak intensities.

Chapter 6

Future projections of Atlantic landfalling TC characteristics

As indicated in Chapters 4 and 5, the landfall intensity of WNP TCs is projected to increase, implying stronger threats to East Asia inland locations under global warming. In order to find out whether similar phenomenon might happen in other regions, responses of Atlantic TCs to global warming is also investigated. In this chapter, Rankine vortices are seeded near eastern US coastlines. TCs developed from these vortices are studied, and their responses to global warming can be tested by PGW technique. Details of the experiment design is described in Chapter 2.2.5.

6.1 Simulating landfalling TCs in the Atlantic based on GFDL regional model

Fig. 6.1 shows the wind speed related to two inserted vortices in August,1985 as the initial condition of the GFDL regional model. It can be seen that the two Rainkine vortices are separated in Gulf of Mexico and Caribbean Sea, and more than 1000 km far away from each other. The far distance is to avoid interactions between the two seeded vortices.

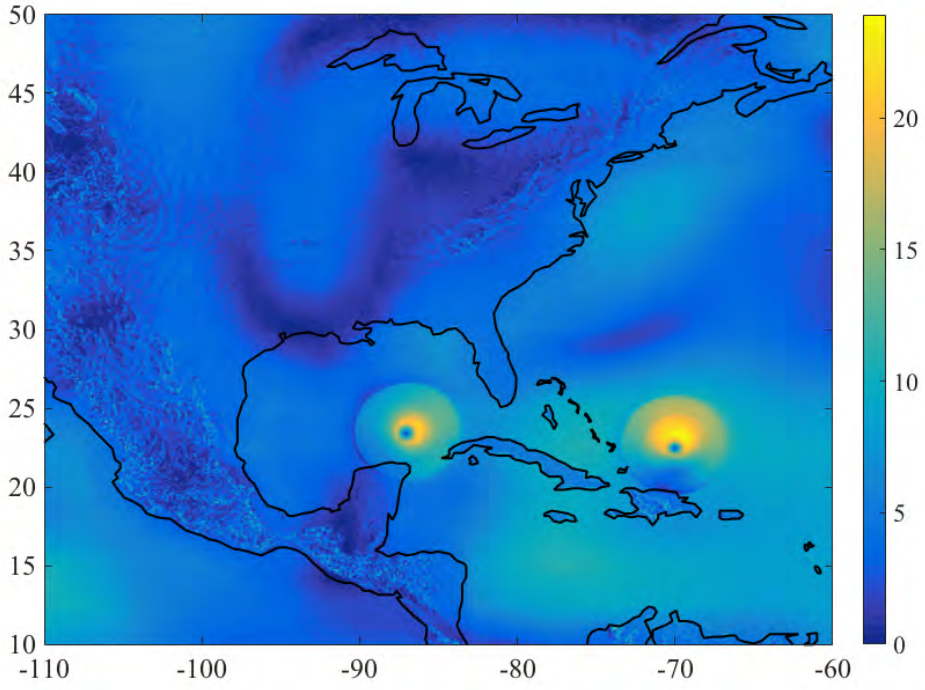

Figure 6.1: The 10-m wind speed (Units: m/s) of two seeded TC-like systems over Gulf of Mexico and the Caribbean Sea in the GFDL regional model.

In order to investigate the spin up of the inserted vortices, the system in the Caribbean Sea is examined. As shown in Fig. 6.2, the maximum wind speed is found to be around 20 m/s with a large and symmetric structure at first (at t=1 hour). The vortex then undergoes intensification and becomes more compact and asymmetric during next 6 hours. The asymmetric core is then re-adjusted to a symmetric system again after 12 hours, after which the system reaches to a steady state over the ocean.

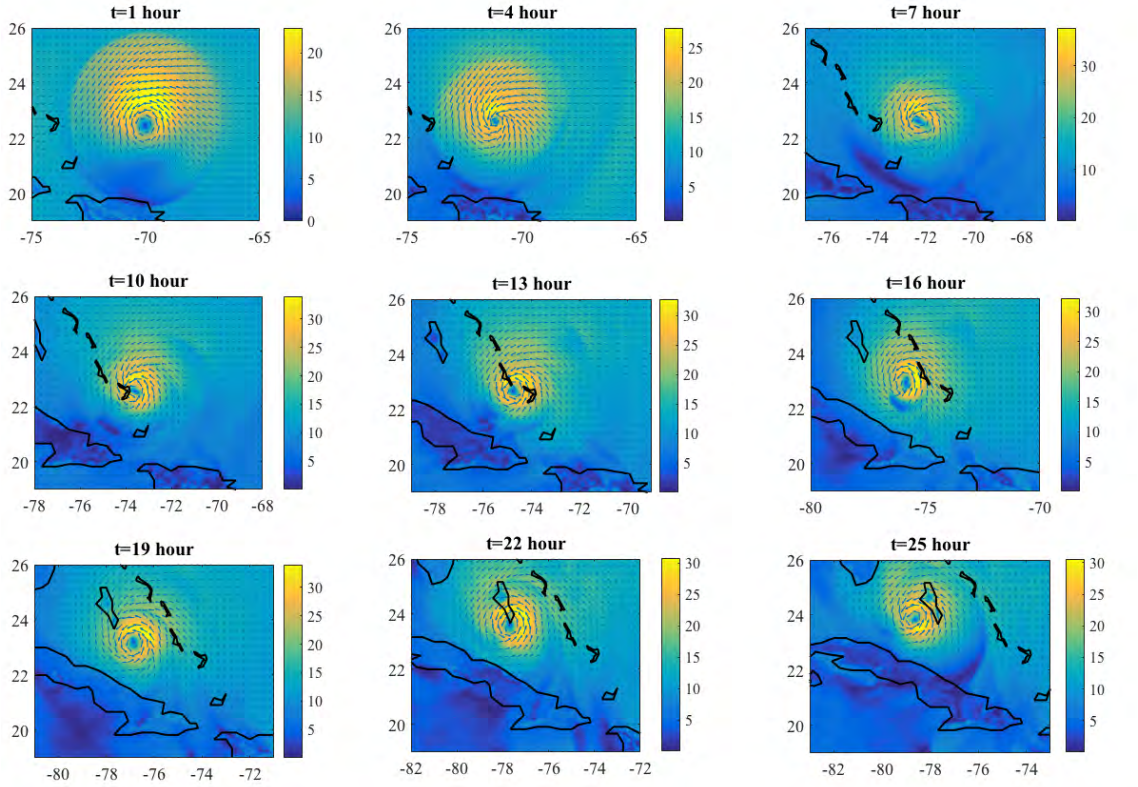

Figure 6.2: Near surface wind field evolution of the seeded vortex. Shading represents the 10-meter wind speed, and vectors showing the wind direction (Units: m/s).

The evolution of the vortex-induced rainfall, shown in Fig. 6.3, can also describe the spin up of the system. There is strong precipitation at the center of the vortex initially,

caused by the artificially introduced humid air that is saturated. After about t=4 hour, a clear eye is seen in the vortex center. In general, the spin up time of the system is about 12-16 hours.

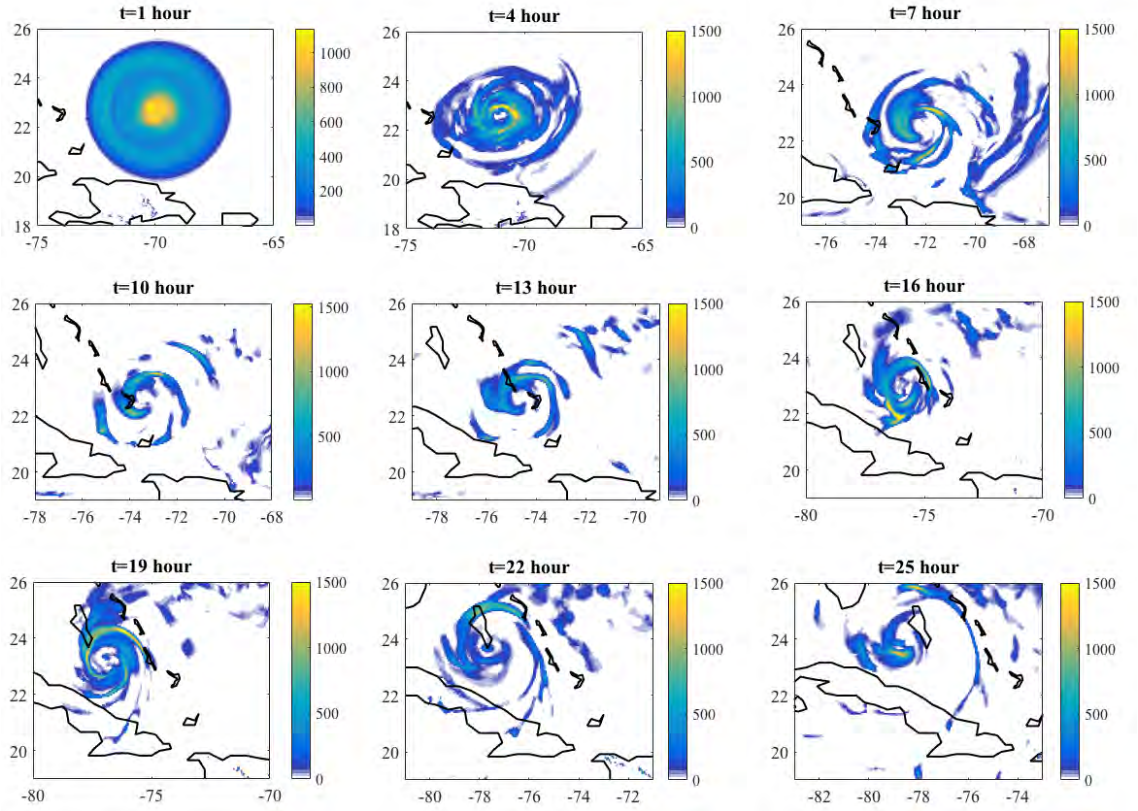

Figure 6.3: Rainfall evolution of the seeded vortex (Units: mm/day).

The TC tracks are detected by identifying the SLP/vorticity center, whenever the surface vorticity exceeds $2 \times 10^{-4} S^{-1}$, with a low pressure center and maximum surface wind speed greater than 13 m/s.

As described in Chapter 2.2.5, 60 Rainkine vortices are seeded and simulated in the ZETAC model. Fig. 6.4 shows the tracks of the 60 systems. 54 of them survived, with

42 making landfall successfully. Two regions, Gulf of Mexico (Region 1) and Caribbean Sea (Region 2) are focused on, from which 25 and 17 landfalling TCs are generated respectively.

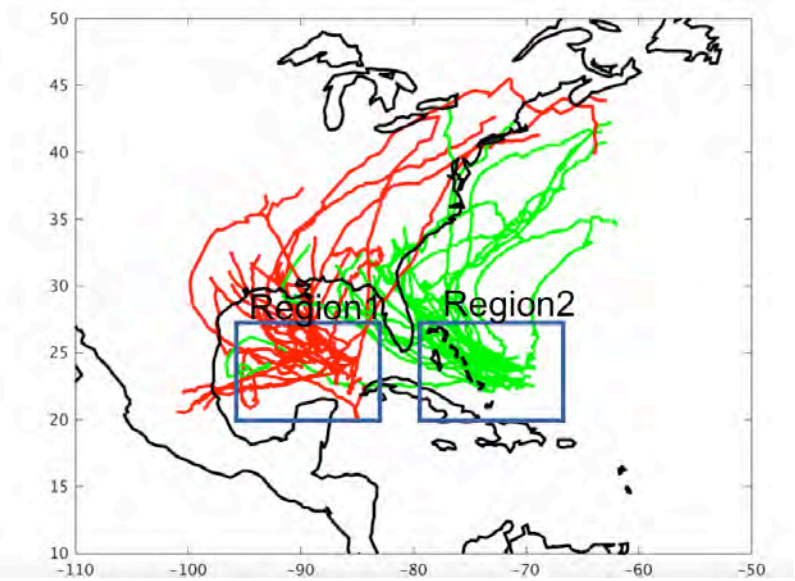

Figure 6.4: Tracks of the seeded Atlantic TCs in the model experiments. Rainkine vortices are seeded in two regions, with tracks in red (green) demonstrating origin from Gulf of Mexico (Caribbean Sea).

6.2 An increase of landfall intensity

Landfall intensity is analysed based on the well simulated TCs as shown in Fig. 6.4. Through the PGW method, the landfall intensities in 2075-2099 period are calculated based on GFDL CM4 warming conditions according to RCP 8.5 scenario (Chapter 2.2.5). Comparison to that from the historical run (1980-2015) are shown in Fig. 6.5. The av-

erage of landfall intensity in the historical runs is 26.9 m/s, while that from PGW runs is 29.6 m/s, with an increase of 2.7 m/s, above the 99% confidence level. The simulated landfall intensity from Region 1 (Fig. 6.5b) is stronger than Region 2 (Fig. 6.5c), and the enhancement under PGW in Region 1 is also stronger than Region 2.

Besides the absolute change of TC landfall intensity, its fractional change is also examined. It is inferred from Fig. 6.6 that the overall landfall intensity can be intensified by about 10.8% (Fig. 6.6a), with increase in Gulf of Mexico of about 11.9% (Fig. 6.6b) and 9.2% in Caribbean Sea.

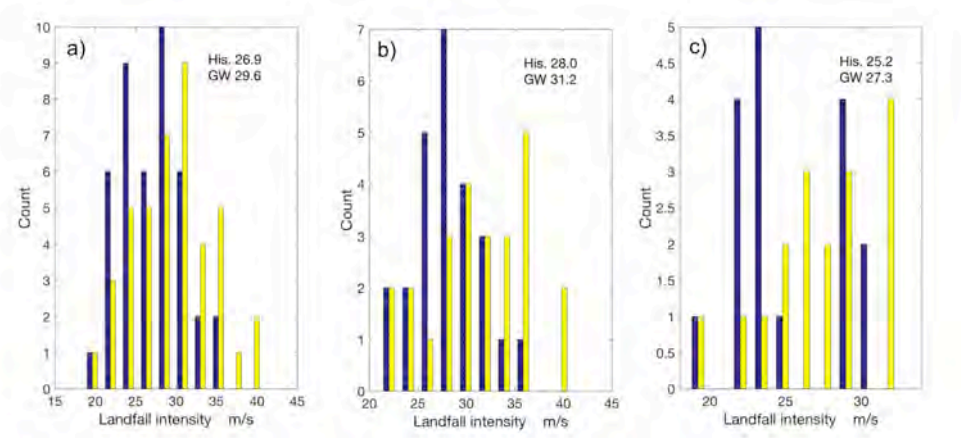

Figure 6.5: Distribution of seed Atlantic TCs landfall intensity (m/s) in the 1980-2015 (His.) and 2075-2099 (GW) periods, averaged over (a) the whole domain; (b) for TCs from region 1 and (c) for TCs from Region 2.

Impacts on the east coast of US due to stronger landfall TCs are also studied. Here, we only consider those TCs which (1) do not recurve back to the ocean, and (2) do not make landfall the second time. Tracks of the selected TCs are shown in Fig. 6.7a. There are 29 TCs in total, with 24 making landfall in Region 1, and only five TCs in Region 2. In view

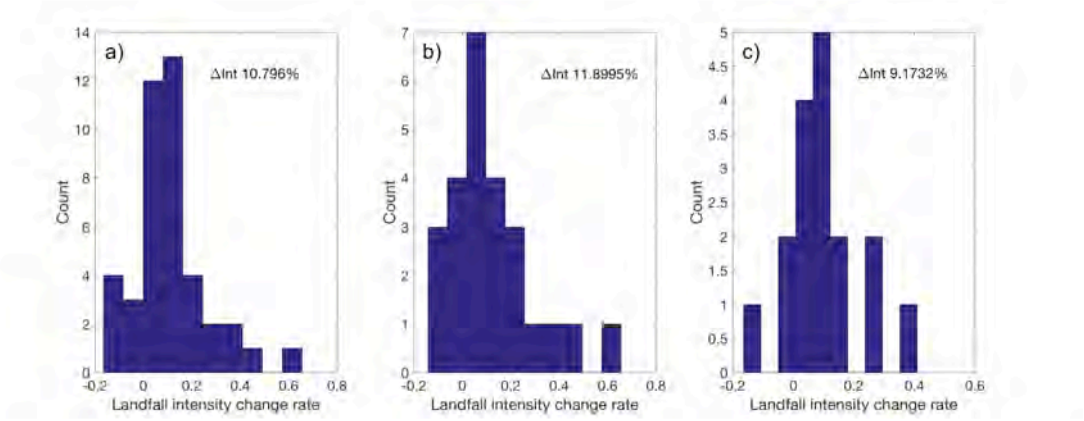

Figure 6.6: Differences in landfall intensity distribution between the 2075-2099 and 1980-2015 era. Average over (a) the overall domain; (b) for TCs from Region 1 and (c) for TCs from Region 2.

of the rather small sample size (only five) for region 2, criteria (2) is relaxed to that the time duration between the two landfall should be longer than half a day. After relaxing criterion (2), 6 more TCs are added in Region 1, and the tracks of the 6 TCs are shown in Fig. 6.7b.

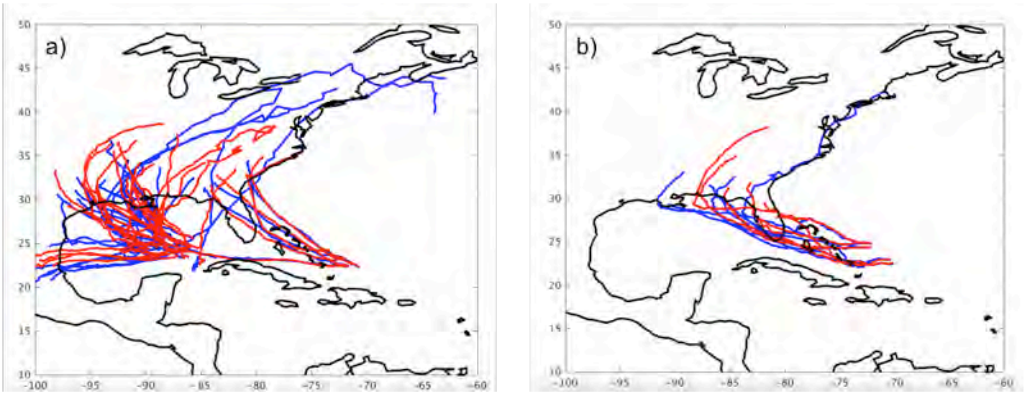

Figure 6.7: The tracks of selected landfall TCs in the two considered regions. (a) TC tracks based on the strict criteria (make landfall once); (b) The added TC tracks after the relaxation of criteria (make landfall twice).

Figure 6.8 compares TC sustaining time over the land in historical and global warming conditions. Overall, TCs can last 18.7 hours after landfall at present, while the time increases to 24.5 hours in warmer future (see Fig. 6.8a). TCs in Region 1 also sustain 5.3 hours longer over land due to global warming (Fig. 6.8b). Both of these increments pass the 90% confidence test. For region 2, there is a 7 hours increase, but the difference does not pass the 90% confidence level (Fig. 6.8c). Fractional change of TC maintaining time after landfall is 61.8% over land in total, 53.4% and 81.8% in Regions 1 and 2.

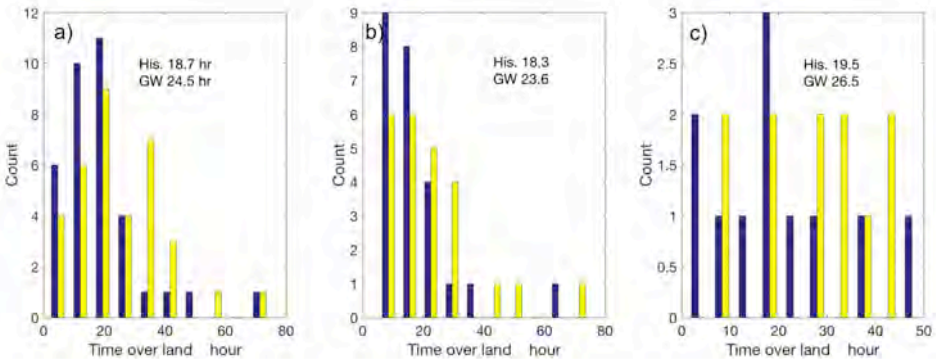

Figure 6.8: Same as Fig. 6.5 except for TC lifetime over land.

TC travelling distance over land in both model experiments are compared in Fig. 6.10. TC can travel 434.7 km after landfall in the historical runs, and 606.9 km under PGW (see Fig. 6.10a). TCs in Region 1 travel 150 km longer in the warmer future (Fig. 6.10b). Both of these two changes are significant at the 90% confidence level. Region 2 also shows an increase of 220 km, but the difference does not pass the 90% confidence level (Fig. 6.10c). Fractional change of distance over the land from all TCs is 87%, while increase in Region 1 (2) is 79.7% (106.4%).

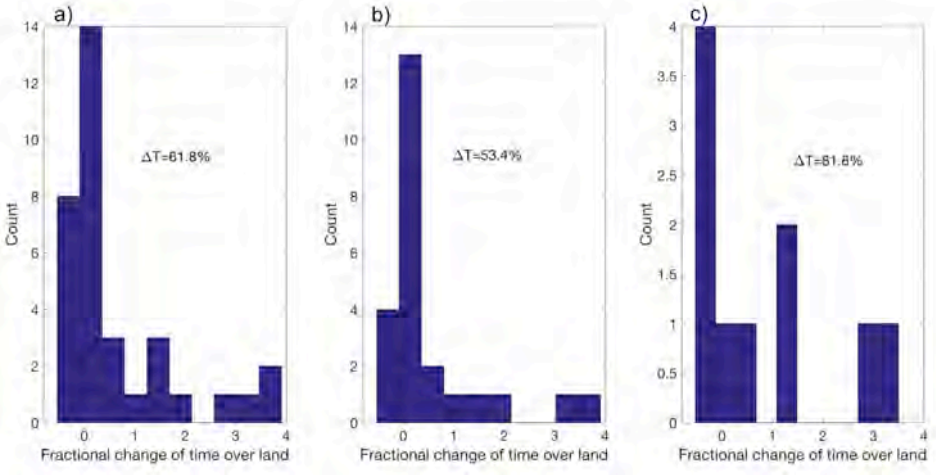

Figure 6.9: Same as Fig. 6.6 except for TC lifetime over land.

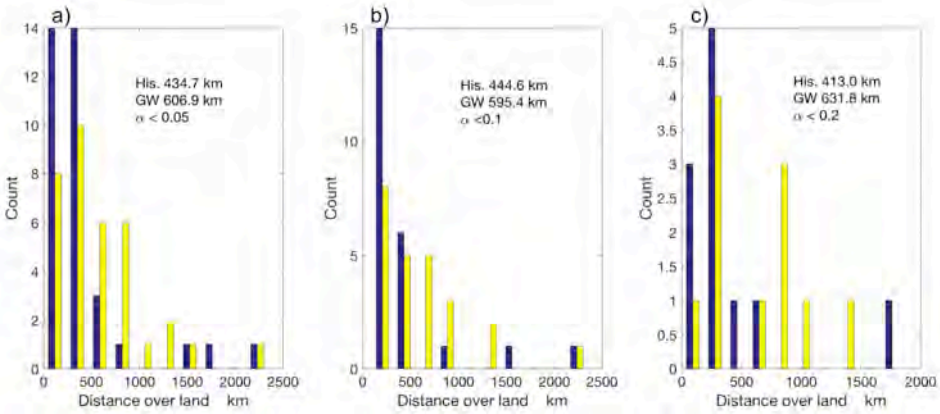

Figure 6.10: Same as Fig. 6.5 except for distance traveled by TCs over land.

Results for PDI of TCs over the land are shown in Fig. 6.12. The PDI is 171.6 kW*h after landfall in the historical experiments, while the value increases to 243.7 kW*h under the global warming (see Fig. 6.12a). For Region 1, it is 82.3 kW*h more in the warmer future (Fig. 6.12b). These increments are significant at the 99% confidence level. For region 2, there is a 21.4 kW*h increase, but the difference does not pass the 90% confidence

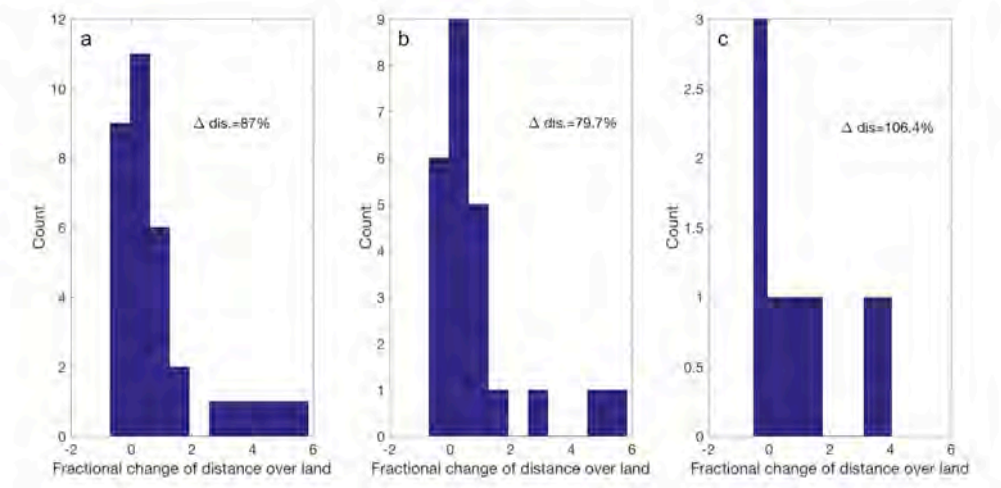

Figure 6.11: Same as Fig. 6.6 except for distance traveled by TCs over land.

level (Fig. 6.12c). Finally, the fractional change of PDI over land is 52%; for Region 1 is 56.3%, and for Region 2 it is 40.7%.

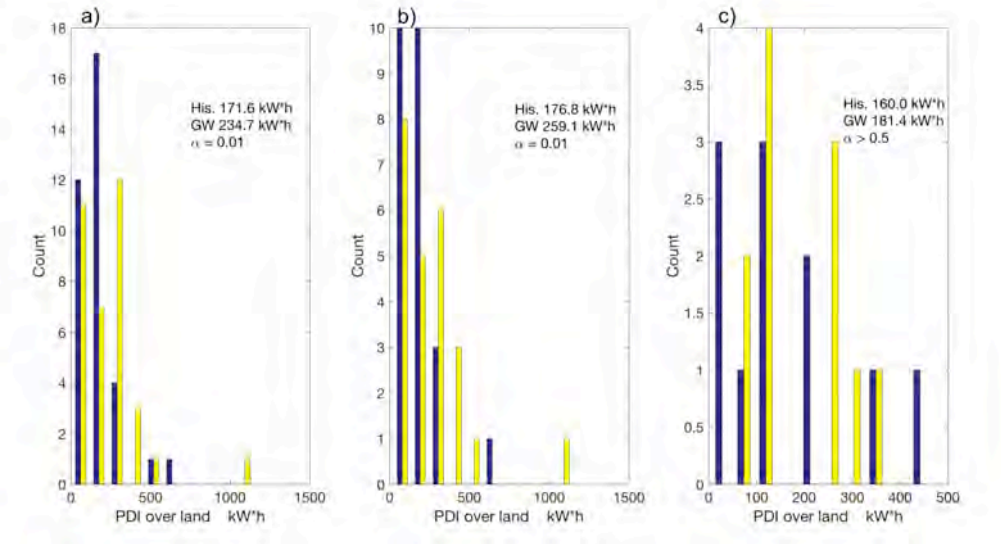

Figure 6.12: Same as Fig. 6.5 except for PDI released by TCs over land.

In summary, how global warming might influence the impacts of Atlantic landfall

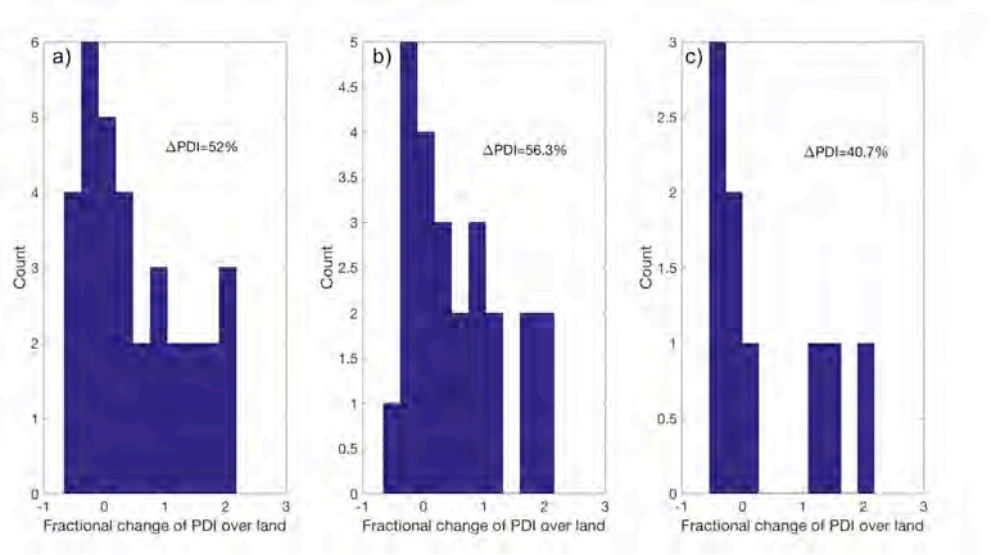

Figure 6.13: Same as Fig. 6.6 except for PDI released by TCs over land.

TCs on land area are projected in the two TC active regions, namely Gulf of Mexico and Caribbean Sea. North Atlantic landfalling TCs are expected an increase by 2.7 m/s (10.8%) in landfall intensity in the warmer future according to the RCP8.5 scenario. This results in 5.8 hours (61.8%) longer sustaining time after landfall, with 172 km (87%) longer travelling distance over land and 63.1 kW*h (52%) more energy.

Chapter 7

Conclusions and discussion

7.1 Major conclusions

7.1.1 Observed changes in WNP TC landfall intensity and influences over inland area

The change of TC landfall intensity over WNP during 1960-2016 was examined. In perticular, landfalling TCs at least of typhoon category or stronger that made landfall in the East and Southeast Asia coastline were considered. It was found that the variation of landfall intensity can be decomposed into a long-term change onto which strong inter-annual variabilities are superimposed. The later inter-annual signal is closely associated with the occurrence of CP El Niño. During CP El Niño boreal summers, stronger low level vorticity is found over climatological genesis locations of WNP landfall TCs, and the vertical wind

shear in the region covering their trajectories is also weakened. Both of these circulation changes are favourable for the development of stronger TCs. The long-term change of TC landfall intensity shows an increasing trend in the period of 1960-2016. This may be attributed to the increase of potential intensity, due to the rapid local SST warming in South China Sea and WNP in the last few decades. There is also reduced vertical wind shear in western north quarter of WNP region associated with weakened upper level anti-cyclone over East China. However, such weakening of upper level anti-cyclonic circulation is still not fully understood. One possibility is natural variation of the SAH. Some studies suggest that SAH can be weakened due to heavier snowfall during 1970-2000 over TP, reduced land-sea thermal contrast during the last decades in addition to warmer eastern Pacific. Other researches argued that anthropogenic aerosols, can slowdown the tropical meridional overturning circulation, which can also weaken SAH[165].

East Asia inland areas also see increasingly strong TC landfall intensity. In addition, TCs sustaining time over land has also become longer. From 1970 to 2016, the sustaining time was increased by 7 hours (50%), and travelling distance over the land also rose by 100 km (67%), while the PDI released to the land area was also doubled. These increments imply more and more East Asian inland locations are impacted by TCs from the ocean.

Using an empirical exponentially-decaying model of TC wind speed, it was found that the decay time scale actually depends on the TC landfall intensity. Such decay time scale tends to be shorter (longer) for stronger (weaker) TCs, which means very intense

systems may not sustain substantially longer than weaker ones. But the PDI released over land is always stronger for stronger TCs, which means more dissipation energy may be released to coastal regions as TC intensity increases. As TC landfall intensity is expected to be enhanced under global warming, the impacts of landfall TCs on the inland areas will become stronger in the warmer future, while for some extreme cases, much stronger influence on coastal regions than expected.

7.1.2 Fewer but stronger WNP TCs under anthropogenic warming projected in MRI-AGCM3.2s

The change of WNP landfalling TCs activity was inferred from MRI-AGCM3.2s model projections. This model can simulate well WNP TC genesis locations and occurrence, albeit weaker TCs in its environment. Suppression TC genesis frequency was found, from 11 per year in the historical run dropping to only 8 in the 2075-2099 period, according to the A1B scenario. The strongest decrease of TC number happens near the Philippines region, which may be related to the low-level anti-cyclonic anomaly in the warmer future. On the other hand, landfall intensity was projected to become about 3 m/s stronger in the 2075-2099. The sustaining time of the storms over land is expected to extend by 6 hours (25.8%), travelling distance over land to increase by 130 km (35%) and PDI released over land to increase by 42%.

7.1.3 Stronger WNP TCs and impacts over PRD based on PGW method using high resolution regional model

Changes of TCs making landfall near PRD in the warmer future (2075-2099), according to the RCP 8.5 scenario, were also examined through the PGW technique. 20 TCs that induced the strongest storm surges to Hong Kong were selected. Their responses to PGW forcing were evaluated, using the 15/3 km high resolution WRF model. It was found that WRF could simulate the TCs structures and tracks well, with reasonable storm intensities. SLOSH model was also used to simulate storm surge heights induced by these TCs. TCs' peak intensities were projected to be intensified by 7.5%∼9.5% on average, while the mean landfall intensity could be enhanced by as much as 11.4%. The RMW is expected to be reduced by 7.4%. The whole storm size (defined as A17) will be 10% larger and PDI is projected to be 18.4% stronger. TC precipitation will be more extreme, with the extreme precipitation near RMW increased by about 22%. Storm surges will also be stronger, with increase of 14.7 cm, 15.6 cm, 9.4 cm and 38.5 cm at Tai Po Kau, North Point, Quarry Bay and Tsim Bei Tsui station, respectively, averaged over all 20 TCs considered. For more than 20% of TCs, the increase of surge height will exceed 40 cm at all stations except Quarry Bay. Some super TCs, such as TC Hope in 1979, can cause an increase of storm surge more than 1 m under a warmer climate.

However, different TCs respond to global warming differently. Fluctuations of intensity increment in the PGW experiments may be related to the specific background environ-

ments of individual TCs. Four background factors were focused on, namely background SST, vertical wind shear, 850 hPa vorticity and 600 hPa RH, and the stepwise regression method was used to assess their relative importance on storm intensification. It was found that the background vertical wind shear is the most important factor, followed by the background SST and mid-level RH. TCs under a weaker vertical shear background tend to get stronger intensification than those with a stronger environmental vertical wind shear in the warmer future.

7.1.4 Stronger influences on East Coast of US

How Atlantic hurricanes might change were also studied by the PGW method, using the ZETAC model, based on GFDL-CM4 projections according to RCP 8.5 scenario. 60 Rainkine vortices were randomly seeded in Gulf of Mexico and the Caribbean Sea in the ZITAC model environment. It was found that the overall landfall intensity could increase 2.7 m/s (10%); enhancement of TC in Gulf of Mexico is 3.2 m/s (11.9%), and that in the Caribbean Sea is 2.1 m/s (9.2%). The TC sustaining time over land could increase by 5.8 hours (61.8%), with the 172.2 km (87%) longer travelling distance and 52% increase in PDI over land. Projection for TCs in Gulf of Mexico region is similar to the overall results, with 5.3 hours (53.4%) increase of sustaining time, 150 km (79.7%) longer in traveling distance and 56.3% stronger of PDI over land.

7.2 Study limitations

First, in Chapter 3, due to the limitations of observation techniques, the accurate observed period for TC best track data is limited to the last 50 years. The observation period means it is difficult to distinguish decadal changes from long-term trend in the TC intensity record. Moreover, the TC activity changes in other regions, such as EP, NA, IO and SP, are not analysed in this study.

Second, in Chapter 4, the MRI-AGCM3.2s model output data used covers the domain of 60^o-150^oE only. Some WNP TCs might be generated outside this region. The relatively coarse resolution of the model (20 km) is another limitation. MRI-AGCM3.2s still cannot simulate very intense TCs, or produce a reasonable TC structure.

Third, in Chapter 5, only TCs making landfall near the PRD area were considered. The results thus cannot represent the TC behaviour in the whole WNP. Further more, a case study on selected storms was conducted. By the design of the experiment, TC tracks remain almost unchanged under PGW, so that the impacts of global warming on TC genesis location cannot be assessed. In fact, the anomalous wind field was not imposed onto the initial and boundary conditions in these PGW experiments. Any change of TC tracks, such as a polar shift as discussed by recent papers, is not studied. Also, changes of climate mode, such as ENSO, in the warmer future, and how they affect TC characteristics, are not considered.

Last but not least, in Chapter 6, the sample size of landfalling TCs in the Caribbean

Sea is too small. The seeded vortices are artificial, and results need to be verified by high-resolution models in long term integration, in which the TCs are generated by model itself.

7.3 Future directions

In Chapter 3, causes of long-term increase in TC landfall intensity are still not ascertained. Model simulations can be conducted to better understand which forcing factor(s) can lead to upper level circulation change near TP. Global TC landfall intensity change also needs to be studied and various circulation elements can be further examined.

The PGW technique can also be applied to study other processes, such as the effects of El Niño on TC intensity change in various basins under global warming. Moreover, previous decades have seen a rapid pace of urbanization in many Asian coastal locations. In the process of urbanization, land surface properties and other conditions will be changed. These factors might also influence the TC landfall process. In the future work, such effects can be added into the PGW experiments, by changing the local landuse, anthropogenic heat etc, over coastal city areas.

Finally, the Rainkine vortex seeding experiments can be carried over the other regions, such as WNP, so as to assess the threats of landfalling TCS to various inland regions under a warmer background climate.

Bibliography

[1] Khouakhi, A., Villarini, G. & Vecchi, G. A. Contribution of tropical cyclones to rainfall at the global scale. ***Journal of Climate*** **30**, 359–372 (2017).

[2] Ramsay, H. The global climatology of tropical cyclones (2017). URL `https://oxfordre.com/naturalhazardscience/view/10.1093/acrefore/9780199389407.001.0001/acrefore-9780199389407-e-79`.

[3] Mei, W. & Xie, S.-P. Intensification of landfalling typhoons over the northwest Pacific since the late 1970s. ***Nature Geoscience*** **9**, 753–757 (2016).

[4] Kossin, J. P., Camargo, S. J. & Sitkowski, M. Climate modulation of North Atlantic hurricane tracks. ***Journal of Climate*** **23**, 3057–3076 (2010).

[5] Kossin, J. P. ***et al.*** Estimating hurricane wind structure in the absence of aircraft reconnaissance. ***Weather and Forecasting*** **22**, 89–101 (2007).

[6] Gray, W. M. & Shea, D. J. The hurricane's inner core region. II. thermal stability and dynamic characteristics. ***Journal of the Atmospheric Sciences*** **30**, 1565–1576 (1973).

[7] Frank, W. M. The structure and energetics of the tropical cyclone I. storm structure. ***Monthly Weather Review*** **105**, 1119–1135 (1977).

[8] Smith, R. Tropical cyclone eye dynamics. ***Journal of the Atmospheric Sciences*** **37**, 1227–1232 (1980).

[9] Shapiro, L. J. & Willoughby, H. E. The response of balanced hurricanes to local sources of heat and momentum. ***Journal of the Atmospheric Sciences*** **39**, 378–394 (1982).

[10] Willoughby, H. Tropical cyclone eye thermodynamics. ***Monthly Weather Review*** **126**, 3053–3067 (1998).

[11] Knapp, K. R., Velden, C. S. & Wimmers, A. J. A global climatology of tropical cyclone eyes. ***Monthly Weather Review*** **146**, 2089–2101 (2018). URL `https://doi.org/10.1175/MWR-D-17-0343.1`. `https://doi.org/10.1175/MWR-D-17-0343.1`.

[12] Montgomery, M. T. & Kallenbach, R. J. A theory for vortex rossby-waves and its application to spiral bands and intensity changes in hurricanes. ***Quarterly Journal of the Royal Meteorological Society*** **123**, 435–465 (1997).

[13] Schubert, W. H. ***et al.*** Polygonal eyewalls, asymmetric eye contraction, and potential vorticity mixing in hurricanes. ***Journal of the Atmospheric Sciences*** **56**, 1197–1223 (1999).

[14] Kossin, J. P. & Schubert, W. H. Mesovortices, polygonal flow patterns, and rapid pressure falls in hurricane-like vortices. ***Journal of the Atmospheric Sciences*** **58**, 2196–2209 (2001).

[15] Nolan, D. S. & Montgomery, M. T. Nonhydrostatic, three-dimensional perturbations to balanced, hurricane-like vortices. part I: Linearized formulation, stability, and evolution. ***Journal of the Atmospheric Sciences*** **59**, 2989–3020 (2002).

[16] Wang, Y. & Wu, C.-C. Current understanding of tropical cyclone structure and intensity changes–a review. ***Meteorology and Atmospheric Physics*** **87**, 257–278 (2004).

[17] Wang, Y. An explicit simulation of tropical cyclones with a triply nested movable mesh primitive equation model: TCM3. part I: Model description and control experiment. ***Monthly Weather Review*** **129**, 1370–1394 (2001).

[18] Schecter, D. A. & Montgomery, M. T. Damping and pumping of a vortex rossby wave in a monotonic cyclone: critical layer stirring versus inertia–buoyancy wave emission. ***Physics of Fluids*** **16**, 1334–1348 (2004).

[19] Diercks, J. W. & Anthes, R. A. Diagnostic studies of spiral rainbands in a nonlinear hurricane model. ***Journal of the Atmospheric Sciences*** **33**, 959–975 (1976).

[20] Willoughby, H. A possible mechanism for the formation of hurricane rainbands. ***Journal of the Atmospheric Sciences*** **35**, 838–848 (1978).

[21] Anthes, R. Tropical cyclones: Their evolution, structure and effects: Boston. ***American Meteorological Society*** (1982).

[22] Chow, K., Chan, K. L. & Lau, A. K. Generation of moving spiral bands in tropical cyclones. ***Journal of the Atmospheric Sciences*** **59**, 2930–2950 (2002).

[23] Schecter, D. A. & Montgomery, M. T. Conditions that inhibit the spontaneous radiation of spiral inertia–gravity waves from an intense mesoscale cyclone. ***Journal of the Atmospheric Sciences*** **63**, 435–456 (2006).

[24] Wang, Y. An explicit simulation of tropical cyclones with a triply nested movable mesh primitive equation model: TCM3. part II: Model refinements and sensitivity to cloud microphysics parameterization. ***Monthly Weather Review*** **130**, 3022–3036 (2002).

[25] Gray, W. M. & Brody, L. ***Global view of the origin of tropical disturbances and storms*** (Citeseer, 1967).

[26] Wang, Y. Rapid filamentation zone in a numerically simulated tropical cyclone. ***Journal of the Atmospheric Sciences*** **65**, 1158–1181 (2008).

[27] Emanuel, K. & Rotunno, R. Self-stratification of tropical cyclone outflow. part I: Implications for storm structure. ***Journal of the Atmospheric Sciences*** **68**, 2236–2249 (2011).

[28] Black, P. G. & Anthes, R. A. On the asymmetric structure of the tropical cyclone outflow layer. ***Journal of the Atmospheric Sciences*** **28**, 1348–1366 (1971).

[29] Dickinson, M. & Molinari, J. Mixed rossby–gravity waves and western Pacific tropical cyclogenesis. part I: Synoptic evolution. ***Journal of the Atmospheric Sciences*** **59**, 2183–2196 (2002).

[30] Montgomery, M. T. & Enagonio, J. Tropical cyclogenesis via convectively forced vortex rossby waves in a three-dimensional quasigeostrophic model. ***Journal of the Atmospheric Sciences*** **55**, 3176–3207 (1998).

[31] Wang, Y. Vortex rossby waves in a numerically simulated tropical cyclone. part I: Overall structure, potential vorticity, and kinetic energy budgets. ***Journal of the Atmospheric Sciences*** **59**, 1213–1238 (2002).

[32] Charney, J. G. & Eliassen, A. On the growth of the hurricane depression. ***Journal of the Atmospheric Sciences*** **21**, 68–75 (1964).

[33] Lander, M. & Holland, G. J. On the interaction of tropical-cyclone-scale vortices. I: Observations. ***Quarterly Journal of the Royal Meteorological Society*** **119**, 1347–1361 (1993).

[34] Ritchie, E. A. & Holland, G. J. On the interaction of tropical-cyclone-scale vortices. II: Discrete vortex patches. ***Quarterly Journal of the Royal Meteorological Society*** **119**, 1363–1379 (1993).

[35] Holland, G. J. & Dietachmayer, G. S. On the interaction of tropical-cyclone-scale vortices. III: Continuous barotropic vortices. ***Quarterly Journal of the Royal Meteorological Society*** **119**, 1381–1398 (1993).

[36] Simpson, J., Ritchie, E., Holland, G., Halverson, J. & Stewart, S. Mesoscale interactions in tropical cyclone genesis. ***Monthly Weather Review*** **125**, 2643–2661 (1997).

[37] Bister, M. & Emanuel, K. A. The genesis of Hurricane Guillermo: TEXMEX analyses and a modeling study. ***Monthly Weather Review*** **125**, 2662–2682 (1997).

[38] Rappin, E. D. & Nolan, D. S. The effect of vertical shear orientation on tropical cyclogenesis. ***Quarterly Journal of the Royal Meteorological Society*** **138**, 1035–1054 (2012).

[39] Hendricks, E. A., Montgomery, M. T. & Davis, C. A. The role of "vortical" hot towers in the formation of tropical cyclone Diana (1984). ***Journal of the Atmospheric Sciences*** **61**, 1209–1232 (2004).

[40] Houze Jr, R. A., Lee, W.-C. & Bell, M. M. Convective contribution to the genesis of Hurricane Ophelia (2005). ***Monthly Weather Review*** **137**, 2778–2800 (2009).

[41] Reasor, P. D., Montgomery, M. T. & Bosart, L. F. Mesoscale observations of the genesis of Hurricane Dolly (1996). ***Journal of the Atmospheric Sciences*** **62**, 3151–3171 (2005).

[42] Montgomery, M., Nicholls, M., Cram, T. & Saunders, A. A vortical hot tower route to tropical cyclogenesis. ***Journal of the Atmospheric Sciences*** **63**, 355–386 (2006).

[43] Jarosz, E., Mitchell, D. A., Wang, D. W. & Teague, W. J. Bottom-up determination of air-sea momentum exchange under a major tropical cyclone. ***Science*** **315**, 1707–1709 (2007).

[44] Cadet, D. Tropical cyclones: Their evolution, structure, and effects. ***Eos, Transactions American Geophysical Union*** **64**, 25–26 (1983).

[45] Gray, W. M. & Landsea, C. W. African rainfall as a precursor of hurricane-related destruction on the US East coast. ***Bulletin of the American Meteorological Society*** **73**, 1352–1364 (1992).

[46] Adler, R. F. Estimating the benefit of trmm tropical cyclone data in saving lives (2005).

[47] Saunders, M. & Rockett, P. Improving typhoon predictions. ***Global Reinsurance Magazine, East Asia Special Report*** 26–29 (2001).

[48] Ryan, C. J. Costs and benefits of tropical cyclones, severe thunderstorms and bushfires in Australia. ***Climatic Change*** **25**, 353–367 (1993).

[49] Capel, A. ***Tropical Cyclone-induced Storm Surges*** (TU Delft, Faculty of Civil Engineering and Geosciences, Hydraulic Engineering, 2001).

[50] Needham, H. F., Keim, B. D. & Sathiaraj, D. A review of tropical cyclone-generated storm surges: Global data sources, observations, and impacts. ***Reviews of Geophysics*** **53**, 545–591 (2015).

[51] Zhang, Q., Gu, X., Shi, P. & Singh, V. P. Impact of tropical cyclones on flood risk in southeastern China: Spatial patterns, causes and implications. ***Global and Planetary Change*** **150**, 81–93 (2017).

[52] Zhang, Q., Zhang, W., Chen, Y. D. & Jiang, T. Flood, drought and typhoon disasters during the last half-century in the Guangdong province, China. ***Natural Hazards*** **57**, 267–278 (2011).

[53] Lee, T. & Wong, C. Historical storm surges and storm surge forecasting in Hong Kong. In ***Hong Kong Observatory, Paper for the JCOMM Scientific and Technical Symposium on Storm Surges (SSS) in Seoul*** (2007).

[54] Otto, P., Mehta, A. & Liu, B. Mind the gap: Towards and beyond impact to enhance tropical cyclone risk communication. ***Tropical Cyclone Research and Review*** **7**, 140–151 (2018).

[55] Pui-yin, H. Weathering the storm: Hong Kong Observatory and social development (2003).

[56] Knutson, T. R. ***et al.*** Tropical cyclones and climate change. ***Nature Geoscience*** **3**, 157–163 (2010).

[57] Nicholls, R. J. & Cazenave, A. Sea-level rise and its impact on coastal zones. ***Science*** **328**, 1517–1520 (2010).

[58] Church, J. A. ***et al.*** Sea-level rise by 2100. ***Science*** **342**, 1445–1445 (2013).

[59] Trenberth, K. E. The definition of El Nino. ***Bulletin of the American Meteorological Society*** **78**, 2771–2778 (1997).

[60] Chan, J. C. Tropical cyclone activity over the Western North Pacific associated with El Niño and La Niña events. ***Journal of Climate*** **13**, 2960–2972 (2000).

[61] Emanuel, K. & Nolan, D. S. Tropical cyclone activity and the global climate system. In ***26th Conference on Hurricanes and Tropical Meteorolgy***, 240–241 (2004).

[62] Camargo, S. J., Emanuel, K. A. & Sobel, A. H. Use of a genesis potential index to diagnose enso effects on tropical cyclone genesis. ***Journal of Climate*** **20**, 4819–4834 (2007).

[63] Chen, G. & Tam, C.-Y. Different impacts of two kinds of Pacific Ocean warming on tropical cyclone frequency over the Western North Pacific. ***Geophysical Research Letters*** **37** (2010).

[64] Wang, B. & Chan, J. C. How strong ENSO events affect tropical storm activity over the Western North Pacific. ***Journal of Climate*** **15**, 1643–1658 (2002).

[65] D CLARK, J. & Chu, P.-S. Interannual variation of tropical cyclone activity over the central North Pacific. ***Journal of the Meteorological Society of Japan. Ser. II*** **80**, 403–418 (2002).

[66] Camargo, S. J. & Sobel, A. H. Western North Pacific tropical cyclone intensity and ENSO. ***Journal of Climate*** **18**, 2996–3006 (2005).

[67] Chu, P.-S. ENSO and tropical cyclone activity. ***Hurricanes and Typhoons: Past, Present, and Potential*** 297–332 (2004).

[68] Lin, I. & Chan, J. C. Recent decrease in typhoon destructive potential and global warming implications. ***Nature Communications*** **6**, 7182 (2015).

[69] Zhao, H. & Wang, C. On the relationship between ENSO and tropical cyclones in the western North Pacific during the boreal summer. ***Climate Dynamics*** 1–14 (2018).

[70] Rodríguez-Fonseca, B. ***et al.*** A review of ENSO influence on the North Atlantic. a non-stationary signal. ***Atmosphere*** **7**, 87 (2016).

[71] Krishnamurthy, L. ***et al.*** Impact of strong ENSO on regional tropical cyclone activity in a high-resolution climate model in the North Pacific and North Atlantic Oceans. ***Journal of Climate*** **29**, 2375–2394 (2016).

[72] Camargo, S. J., Robertson, A. W., Barnston, A. G. & Ghil, M. Clustering of eastern North Pacific tropical cyclone tracks: ENSO and MJO effects. ***Geochemistry, Geophysics, Geosystems*** **9** (2008).

[73] Kuleshov, Y., Qi, L., Fawcett, R. & Jones, D. On tropical cyclone activity in the Southern Hemisphere: Trends and the ENSO connection. ***Geophysical Research Letters*** **35** (2008).

[74] Evans, J. L. & Allan, R. J. El Nino/Southern Oscillation modification to the structure of the monsoon and tropical cyclone activity in the Australasian region. ***International Journal of Climatology*** **12**, 611–623 (1992).

[75] Geng, H., Shi, D., Zhang, W. & Huang, C. A prediction scheme for the frequency of summer tropical cyclone landfalling over China based on data mining methods. ***Meteorological Applications*** **23**, 587–593 (2016).

[76] Gray, W. M. Atlantic seasonal hurricane frequency. part I: El Niño and 30 mb quasi-biennial oscillation influences. ***Monthly Weather Review*** **112**, 1649–1668 (1984).

[77] Hansen, F., Matthes, K. & Wahl, S. Tropospheric QBO–ENSO interactions and differences between the Atlantic and Pacific. ***Journal of Climate*** **29**, 1353–1368 (2016).

[78] Fan, K. North Pacific sea ice cover, a predictor for the western North Pacific typhoon frequency? ***Science in China Series D: Earth Sciences*** **50**, 1251–1257 (2007).

[79] Xie, L., Yan, T., Pietrafesa, L. J., Karl, T. & Xu, X. Relationship between western North Pacific typhoon activity and Tibetan Plateau winter and spring snow cover. ***Geophysical Research Letters*** **32** (2005).

[80] Xie, L. & Yan, T. West North Pacific typhoon track patterns and their potential connection to Tibetan Plateau snow cover. ***Natural Hazards*** **42**, 317–333 (2007).

[81] Wang, X. & Liu, H. PDO modulation of ENSO effect on tropical cyclone rapid intensification in the western North Pacific. ***Climate Dynamics*** **46**, 15–28 (2016).

[82] Liu, K. S. & Chan, J. C. Interdecadal variability of western North Pacific tropical cyclone tracks. ***Journal of Climate*** **21**, 4464–4476 (2008).

[83] Wang, H., Sun, J. & Fan, K. Relationships between the North Pacific Oscillation and the typhoon/hurricane frequencies. ***Science in China Series D: Earth Sciences*** **50**, 1409–1416 (2007).

[84] Mann, M. E. & Emanuel, K. A. Atlantic hurricane trends linked to climate change. ***Eos, Transactions American Geophysical Union*** **87**, 233–241 (2006).

[85] Kossin, J. P. & Vimont, D. J. A more general framework for understanding Atlantic hurricane variability and trends. ***Bulletin of the American Meteorological Society*** **88**, 1767–1782 (2007).

[86] Aiyyer, A. & Molinari, J. MJO and tropical cyclogenesis in the Gulf of Mexico and eastern Pacific: Case study and idealized numerical modeling. ***Journal of the Atmospheric Sciences*** **65**, 2691–2704 (2008).

[87] Liebmann, B., Hendon, H. H. & Glick, J. D. The relationship between tropical cyclones of the western Pacific and Indian Oceans and the Madden-Julian oscillation. ***Journal of the Meteorological Society of Japan. Ser. II*** **72**, 401–412 (1994).

[88] Ho, C.-H., Kim, J.-H., Jeong, J.-H., Kim, H.-S. & Chen, D. Variation of tropical cyclone activity in the South Indian Ocean: El Niño–Southern Oscillation and Madden-Julian Oscillation effects. ***Journal of Geophysical Research: Atmospheres*** **111** (2006).

[89] Hall, J. D., Matthews, A. J. & Karoly, D. J. The modulation of tropical cyclone activity in the Australian region by the Madden–Julian oscillation. ***Monthly Weather Review*** **129**, 2970–2982 (2001).

[90] Trenberth, K. Uncertainty in hurricanes and global warming. ***Science*** **308**, 1753–1754 (2005).

[91] Knutson, T. R. ***et al.*** Global projections of intense tropical cyclone activity for the late twenty-first century from dynamical downscaling of CMIP5/RCP4.5 scenarios. ***Journal of Climate*** **28**, 7203–7224 (2015).

[92] Webster, P. J., Holland, G. J., Curry, J. A. & Chang, H.-R. Changes in tropical cyclone number, duration, and intensity in a warming environment. ***Science*** **309**, 1844–1846 (2005).

[93] Elsner, J. B., Kossin, J. P. & Jagger, T. H. The increasing intensity of the strongest tropical cyclones. ***Nature*** **455**, 92–95 (2008).

[94] Walsh, K. Tropical cyclones and climate change: unresolved issues. ***Climate Research*** **27**, 77–83 (2004).

[95] Gualdi, S., Scoccimarro, E. & Navarra, A. Changes in tropical cyclone activity due to global warming: Results from a high-resolution coupled general circulation model. ***Journal of Climate*** **21**, 5204–5228 (2008).

[96] Chan, J. C. Comment on" changes in tropical cyclone number, duration, and intensity in a warming environment". ***Science*** **311**, 1713–1713 (2006).

[97] Lin, I.-I., Chen, C.-H., Pun, I.-F., Liu, W. T. & Wu, C.-C. Warm ocean anomaly, air sea fluxes, and the rapid intensification of tropical cyclone Nargis (2008). ***Geophysical Research Letters*** **36** (2009).

[98] Murakami, H., Mizuta, R. & Shindo, E. Future changes in tropical cyclone activity projected by multi-physics and multi-SST ensemble experiments using the 60-km-mesh MRI-AGCM. ***Climate Dynamics*** **39**, 2569–2584 (2012).

[99] Oouchi, K. ***et al.*** Tropical cyclone climatology in a global-warming climate as simulated in a 20 km-mesh global atmospheric model: Frequency and wind intensity analyses. ***Journal of the Meteorological Society of Japan. Ser. II*** **84**, 259–276 (2006).

[100] Stocker, T. F. & Schmittner, A. Influence of CO_2 emission rates on the stability of the thermohaline circulation. ***Nature*** **388**, 862 (1997).

[101] DeMaria, M. The effect of vertical shear on tropical cyclone intensity change. ***Journal of the Atmospheric Sciences*** **53**, 2076–2088 (1996).

[102] Corbosiero, K. L. & Molinari, J. The effects of vertical wind shear on the distribution of convection in tropical cyclones. ***Monthly Weather Review*** **130**, 2110–2123 (2002).

[103] Briegel, L. M. & Frank, W. M. Large-scale influences on tropical cyclogenesis in the western North Pacific. ***Monthly Weather Review*** **125**, 1397–1413 (1997).

[104] Ritchie, E. A. & Holland, G. J. Large-scale patterns associated with tropical cyclogenesis in the western Pacific. ***Monthly Weather Review*** **127**, 2027–2043 (1999).

[105] Taylor, K. E., Stouffer, R. J. & Meehl, G. A. An overview of CMIP5 and the experiment design. ***Bulletin of the American Meteorological Society*** **93**, 485–498 (2012).

[106] Camargo, S. J., Ting, M. & Kushnir, Y. Influence of local and remote SST on North Atlantic tropical cyclone potential intensity. ***Climate Dynamics*** **40**, 1515–1529 (2013).

[107] Camargo, S. J. Global and regional aspects of tropical cyclone activity in the CMIP5 models. ***Journal of Climate*** **26**, 9880–9902 (2013).

[108] Strachan, J., Vidale, P. L., Hodges, K., Roberts, M. & Demory, M.-E. Investigating global tropical cyclone activity with a hierarchy of AGCMs: The role of model resolution. ***Journal of Climate*** **26**, 133–152 (2013).

[109] Manganello, J. V. ***et al.*** Tropical cyclone climatology in a 10-km global atmospheric GCM: toward weather-resolving climate modeling. ***Journal of Climate*** **25**, 3867–3893 (2012).

[110] Murakami, H. & Wang, B. Future change of North Atlantic tropical cyclone tracks: Projection by a 20-km-mesh global atmospheric model. ***Journal of Climate*** **23**, 2699–2721 (2010).

[111] Lavender, S. & Walsh, K. Dynamically downscaled simulations of Australian region tropical cyclones in current and future climates. ***Geophysical Research Letters*** **38** (2011).

[112] Zhao, M. & Held, I. M. An analysis of the effect of global warming on the intensity of Atlantic hurricanes using a GCM with statistical refinement. ***Journal of Climate*** **23**, 6382–6393 (2010).

[113] Emanuel, K. A. Downscaling CMIP5 climate models shows increased tropical cyclone activity over the 21st century. ***Proceedings of the National Academy of Sciences*** **110**, 12219–12224 (2013).

[114] Kimura, F. & Kitoh, A. Downscaling by pseudo global warming method. ***The Final Report of ICCAP*** **4346** (2007).

[115] Schär, C., Frei, C., Lüthi, D. & Davies, H. C. Surrogate climate-change scenarios for regional climate models. ***Geophysical Research Letters*** **23**, 669–672 (1996).

[116] Hara, M., Yoshikane, T., Kawase, H. & Kimura, F. Estimation of the impact of global warming on snow depth in Japan by the pseudo-global-warming method. ***Hydrological Research Letters*** **2**, 61–64 (2008).

[117] Kawase, H. ***et al.*** Intermodel variability of future changes in the baiu rainband estimated by the pseudo global warming downscaling method. ***Journal of Geophysical Research: Atmospheres*** **114** (2009).

[118] Hill, K. A. & Lackmann, G. M. The impact of future climate change on TC intensity and structure: A downscaling approach. ***Journal of Climate*** **24**, 4644–4661 (2011).

[119] Ninomiya, J., Mori, N., Takemi, T. & Arakawa, O. SST ensemble experiment-based impact assessment of climate change on storm surge caused by pseudo-global warming: Case study of typhoon Vera in 1959. ***Coastal Engineering Journal*** **59**, 1740002 (2017).

[120] Jisan, M. A. ***et al.*** Hurricane Matthew (2016) and its impact under global warming scenarios. ***Modeling Earth Systems and Environment*** **4**, 97–109 (2018).

[121] Parker, C. L., Bruyère, C. L., Mooney, P. A. & Lynch, A. H. The response of land-falling tropical cyclone characteristics to projected climate change in northeast Australia. ***Climate Dynamics*** 1–19 (2018).

[122] Nakamura, R., Shibayama, T., Esteban, M. & Iwamoto, T. Future typhoon and storm surges under different global warming scenarios: case study of Typhoon Haiyan (2013). ***Natural Hazards*** **82**, 1645–1681 (2016).

[123] Kaplan, J. & DeMaria, M. A simple empirical model for predicting the decay of tropical cyclone winds after landfall. ***Journal of Applied Meteorology*** **34**, 2499–2512 (1995).

[124] Kaplan, J. & DeMaria, M. On the decay of tropical cyclone winds after landfall in the New England area. ***Journal of Applied Meteorology*** **40**, 280–286 (2001).

[125] Yukimoto, S. ***Meteorological research institute earth system model version 1 (MRI-ESM1): model description*** (Meteorological Research Institute, 2011).

[126] Kitoh, A. ***et al.*** Projection of changes in future weather extremes using super-high-resolution global and regional atmospheric models in the KAKUSHIN program: Results of preliminary experiments. ***Hydrological Research Letters*** **3**, 49–53 (2009).

[127] Kanamitsu, M., Tada, K., Kudo, T., Sato, N. & Isa, S. Description of the JMA operational spectral model. ***Journal of the Meteorological Society of Japan. Ser. II*** **61**, 812–828 (1983).

[128] JMA. Outline of the operational numerical weather prediction at the Japan Meteorological Agency (appendix to WMO numerical weather prediction progress report). ***Japan Meteorological Agency*** 194 (2007).

[129] Mellor, G. L. & Yamada, T. A hierarchy of turbulence closure models for planetary boundary layers. ***Journal of the Atmospheric Sciences*** **31**, 1791–1806 (1974).

[130] Hirai, M. ***et al.*** Development and validation of a new land surface model for JMA's operational global model using the CEOP observation dataset. ***Journal of the Meteorological Society of Japan. Ser. II*** **85**, 1–24 (2007).

[131] Mizuta, R. ***et al.*** Climate simulations using MRI-AGCM3.2 with 20-km grid. ***Journal of the Meteorological Society of Japan. Ser. II*** **90**, 233–258 (2012).

[132] Rayner, N. ***et al.*** Global analyses of sea surface temperature, sea ice, and night marine air temperature since the late nineteenth century. ***Journal of Geophysical Research: Atmospheres*** **108** (2003).

[133] Bourke, R. H. & Garrett, R. P. Sea ice thickness distribution in the Arctic ocean. ***Cold Regions Science and Technology*** **13**, 259–280 (1987).

[134] Skamarock, W. ***et al.*** A description of the advanced research WRF version 3, NCAR technical note, mesoscale and microscale meteorology division. ***National Center for Atmospheric Research, Boulder, Colorado, USA*** (2008).

[135] Gentry, M. S. & Lackmann, G. M. Sensitivity of simulated tropical cyclone structure and intensity to horizontal resolution. ***Monthly Weather Review*** **138**, 688–704 (2010).

[136] Dudhia, J. Numerical study of convection observed during the winter monsoon experiment using a mesoscale two-dimensional model. ***Journal of the Atmospheric Sciences*** **46**, 3077–3107 (1989).

[137] Mlawer, E. J., Taubman, S. J., Brown, P. D., Iacono, M. J. & Clough, S. A. Radiative transfer for inhomogeneous atmospheres: RRTM, a validated correlated-k model for the longwave. ***Journal of Geophysical Research: Atmospheres*** **102**, 16663–16682 (1997).

[138] Rogers, E. ***et al.*** Changes to the NCEP Meso-eta analysis and forecast system: Increase in resolution, new cloud microphysics, modified precipitation assimilation, modified 3DVAR analysis. ***NWS Technical Procedures Bulletin*** **488**, 15 (2001).

[139] Kain, J. S. The Kain–Fritsch convective parameterization: an update. ***Journal of Applied Meteorology*** **43**, 170–181 (2004).

[140] Hong, S.-Y., Noh, Y. & Dudhia, J. A new vertical diffusion package with an explicit treatment of entrainment processes. ***Monthly Weather Review*** **134**, 2318–2341 (2006).

[141] Tewari, M. ***et al.*** Implementation and verification of the unified NOAH land surface model in the WRF model. In ***20th conference on weather analysis and forecasting/16th conference on numerical weather prediction***, vol. 1115 (2004).

[142] Jiménez, P. A. ***et al.*** A revised scheme for the WRF surface layer formulation. ***Monthly Weather Review*** **140**, 898–918 (2012).

[143] Glahn, B., Taylor, A., Kurkowski, N. & Shaffer, W. A. The role of the SLOSH model in National Weather Service storm surge forecasting. ***National Weather Digest*** **33**, 3–14 (2009).

[144] Lin, N., Emanuel, K. A., Smith, J. & Vanmarcke, E. Risk assessment of hurricane storm surge for New York City. ***Journal of Geophysical Research: Atmospheres*** **115** (2010).

[145] Platzman, G. W. The dynamical prediction of wind tides on Lake Erie. In ***The Dynamical Prediction of Wind Tides on Lake Erie***, 1–44 (Springer, 1963).

[146] Jelesnianski, C. P. Numerical computations of storm surges with bottom stress. ***Monthly Weather Review*** **95**, 740–756 (1967).

[147] Chow, V. T. Open-channel hydraulics. In ***Open-channel hydraulics*** (McGraw-Hill, 1959).

[148] Wanstrath, J. J., Whitaker, R. E., Reid, R. O. & Vastano, A. C. Storm surge simulation in transformed coordinates. volume I. theory and application. Tech. Rep., TEXAS A AND M RESEARCH FOUNDATION COLLEGE STATION (1976).

[149] Jelesnianski, C. P., Chen, J. & Shaffer, W. A. SLOSH: Sea, lake, and overland surges from hurricanes (1992).

[150] Skamarock, W. C. & Klemp, J. B. The stability of time-split numerical methods for the hydrostatic and the nonhydrostatic elastic equations. ***Monthly Weather Review*** **120**, 2109–2127 (1992).

[151] Garner, S. T., Frierson, D., Held, I., Pauluis, O. & Vallis, G. Resolving convection in a global hypohydrostatic model. ***Journal of the Atmospheric Sciences*** **64**, 2061–2075 (2007).

[152] Frierson, D. M., Held, I. M. & Zurita-Gotor, P. A gray-radiation aquaplanet moist GCM. part I: Static stability and eddy scale. ***Journal of the Atmospheric Sciences*** **63**, 2548–2566 (2006).

[153] Knapp, K. R., Kruk, M. C., Levinson, D. H., Diamond, H. J. & Neumann, C. J. The international best track archive for climate stewardship (IBTrACS) unifying tropical cyclone data. ***Bulletin of the American Meteorological Society*** **91**, 363–376 (2010).

[154] Jarraud, M. Guide to meteorological instruments and methods of observation (WMO-No. 8). ***World Meteorological Organisation: Geneva, Switzerland*** (2008).

[155] Berrisford, P. ***et al.*** The ERA-Interim archive version 2.0 23 (2011).

[156] Poli, P. ***et al.*** ERA-20C: An atmospheric reanalysis of the twentieth century. ***Journal of Climate*** **29**, 4083–4097 (2016).

[157] Ji, M., Kumar, A. & Leetmaa, A. A multiseason climate forecast system at the National Meteorological Center. ***Bulletin of the American Meteorological Society*** **75**, 569–578 (1994).

[158] Kobayashi, S. ***et al.*** The JRA-55 reanalysis: General specifications and basic characteristics. ***Journal of the Meteorological Society of Japan. Ser. II*** **93**, 5–48 (2015).

[159] Ebita, A. ***et al.*** The Japanese 55-year reanalysis "JRA-55": an interim report. ***Sola*** **7**, 149–152 (2011).

[160] Ishii, M., Shouji, A., Sugimoto, S. & Matsumoto, T. Objective analyses of sea-surface temperature and marine meteorological variables for the 20th century using ICOADS and the KOBE collection. ***International Journal of Climatology*** **25**, 865–879 (2005).

[161] Guo, H. ***et al.*** NOAA-GFDL GFDL-CM4 model output (2018). URL `https://doi.org/10.22033/ESGF/CMIP6.1402`.

[162] Emanuel, K. A. The dependence of hurricane intensity on climate. ***Nature*** **326**, 483 (1987).

[163] Kosaka, Y. & Xie, S.-P. Recent global-warming hiatus tied to equatorial pacific surface cooling. ***Nature*** **501**, 403 (2013).

[164] Ding, Y., Sun, Y., Wang, Z., Zhu, Y. & Song, Y. Inter-decadal variation of the summer precipitation in China and its association with decreasing Asian summer monsoon part II: Possible causes. ***International Journal of Climatology: A Journal of the Royal Meteorological Society*** **29**, 1926 (2009).

[165] Bollasina, M. A., Ming, Y. & Ramaswamy, V. Anthropogenic aerosols and the weakening of the $s$outh $a$sian summer monsoon. ***Science*** **334**, 502–505 (2011).

[166] Kossin, J. P. A global slowdown of tropical-cyclone translation speed. ***Nature* 558**, 104 (2018).

[167] Bhowmik, S. R., Kotal, S. & Kalsi, S. An empirical model for predicting the decay of tropical cyclone wind speed after landfall over the Indian region. ***Journal of Applied Meteorology* 44**, 179–185 (2005).

[168] Tuleya, R. E., Bender, M. A. & Kurihara, Y. A simulation study of the landfall of tropical cyclones. ***Monthly Weather Review* 112**, 124–136 (1984).

[169] Powell, M. D., Dodge, P. P. & Black, M. L. The landfall of Hurricane Hugo in the Carolinas: Surface wind distribution. ***Weather and Forecasting* 6**, 379–399 (1991).

[170] Tuleya, R. E. Tropical storm development and decay: Sensitivity to surface boundary conditions. ***Monthly Weather Review* 122**, 291–304 (1994).

[171] Tuleya, R. E. & Kurihara, Y. A numerical simulation of the landfall of tropical cyclones. ***Journal of the Atmospheric Sciences* 35**, 242–257 (1978).

[172] Murakami, H. ***et al.*** Future changes in tropical cyclone activity projected by the new high-resolution MRI-AGCM. ***Journal of Climate* 25**, 3237–3260 (2012).

[173] LUI, Y. S. ***Simulations of Daily Extremes and Diurnal Variations of Precipitation over East and Southeast Asia by Climate Models***. Ph.D. thesis, The Chinese University of Hong Kong (2017).

[174] Wang, S. & Toumi, R. Reduced sensitivity of tropical cyclone intensity and size to sea surface temperature in a radiative-convective equilibrium environment. ***Advances in Atmospheric Sciences*** **35**, 981–993 (2018).

[175] Pall, P., Allen, M. & Stone, D. A. Testing the Clausius–Clapeyron constraint on changes in extreme precipitation under CO_2 warming. ***Climate Dynamics*** **28**, 351–363 (2007).

Appendix A

Rankine vortex

The Rainkine vortex is a simple mathematical model to describe a vortex in fluid. The Rainkine vortex can be characterized by a symmetric central core comprising a forced vortex, surrounded by a free vortex. The radial and vertical distribution of tangential wind is

$$v = \begin{cases} V_{max} \frac{r}{R} e^{-z/H} & (r \leq R) \\ V_{max} \frac{R}{r} e^{-z/H} & (r > R) \end{cases} \tag{A.1}$$

Here the Rainkine vortex wind speed increases linearly from vortex center to RMW (R) up to the maximum tangential wind speed V_{max}, and then decreases as $1/r$ to the infinity. The wind speed also decreases exponentially with a factor of $e^{-z/H}$ vertically, where z is the vertical height and H is the scale height (suggested to be 5000 m). The wind distribution is shown in Fig. A.1, with $V_{max} = 40m/s$ and $R = 100km$.

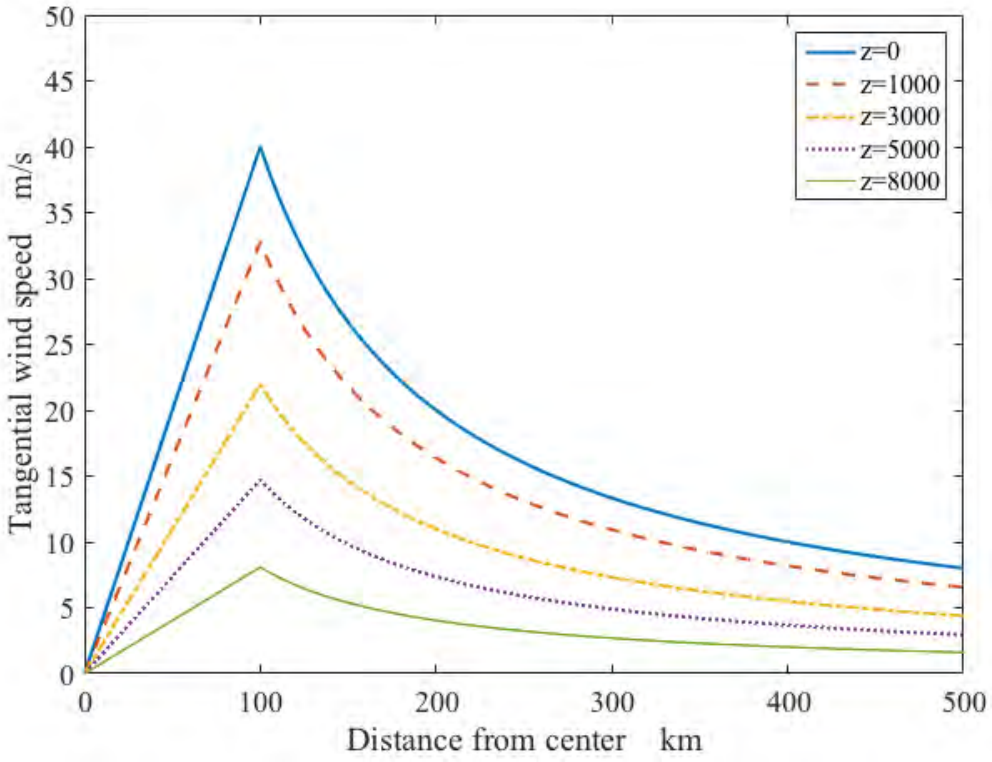

Figure A.1: Tangential velocity distribution in a Rainkine vortex

Ignoring Coriolis force effect, the equation of motion is,

$$\frac{dv}{dt} = -\frac{v^2}{r} - \frac{1}{\rho}\frac{\partial p}{\partial r} \tag{A.2}$$

Supposed the centrifugal force being in balance with pressure gradient force, subtracting the wind speed distribution using Eq. A.1, a differential pressure distribution can be

derived as,

$$\frac{\partial p}{\partial r} = \begin{cases} -\rho V_{max}^2 \frac{r}{R^2} e^{-2z/H} & (r \leq R) \\ -\rho V_{max}^2 \frac{R^2}{r^3} e^{-2z/H} & (r > R) \end{cases} \tag{A.3}$$

Integrating Eq. A.3, the pressure distribution is given by,

$$P = \begin{cases} \frac{1}{2}\rho V_{max}^2 \frac{r^2}{R^2} e^{-2z/H} + C_1 & (r \leq R) \\ -\frac{1}{2}\rho V_{max}^2 \frac{R^2}{r^2} e^{-2z/H} + C_2 & (r > R) \end{cases} \tag{A.4}$$

where C_1 is the vortex's center pressure and C_2 is the pressure at the infinity in a specific height. When $r = R$, $P(r \leq R) = P(r > R)$, and one gets $C_2 - C_1 = \rho V_{max}^2 e^{-2z/H}$. In this study, the farthest effect of the Rainkine vortex is supposed to be around 350 km, and C_2 equals to the background P at the distance of 500 km from the vortex center.

Assuming hydrostatic balance,

$$\frac{\partial P}{\partial z} = -\rho g \tag{A.5}$$

where ρ is air density and $P = \rho RT$ due to the ideal gas law, with R gas constant. Using the ideal gas law, Eq. A.5 can be integrated to obtain,

$$< T >= \frac{g\delta z}{R(lnP_0 - lnP_1)} \tag{A.6}$$

where $< T >$ is the mean temperature of the isothermal layer, while P_0 and P_1 are the

lower and upper pressure of the isothermal layer and δz is the depth of the isothermal layer. Combining Eqs. A.4 with Eq.A.6, the vertical structure of temperature in the Rainkine vortex can be found in Fig. A.2. From Fig. A.2, the pressure drops to minimum as the temperature becomes warmest in the vortex center, as expected for a TC.

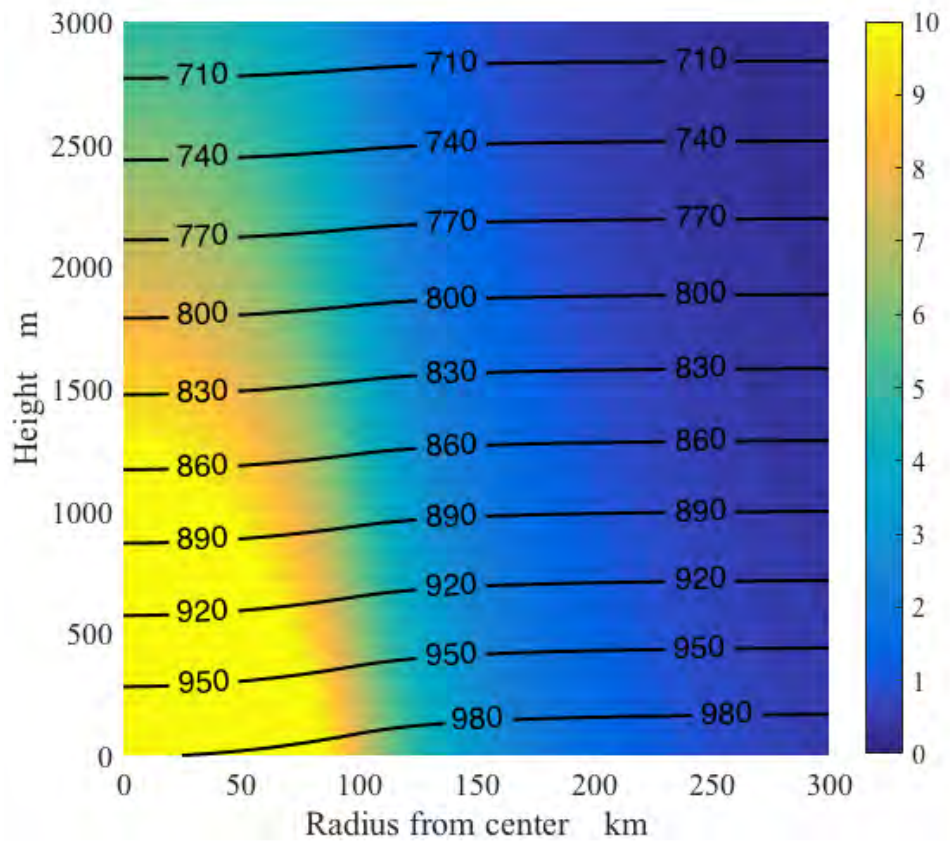

Figure A.2: Vertical pressure and temperature structure of Rainkine vortex. Counter lines are pressure profile (Units: hPa), while the shading is the warm centre of vertical temperature with background temperature (∼290 K at surface level, gradually decrease with height) deducted(Units: K).

RH is set to 100% from vortex center to RMW, and then smoothly drops to the back-

ground RH value at the edge of the vortex (around 300 km from the vortex center). High RH is needed for the growth of the vortex into a mature TC.

In order to ensure smooth translation between the vortex and background meteorological variables, a weighting function ω of vortex is used to combine the two fields. It can be seen from Fig. A.3 that ω is almost 1 from vortex center up to 250 km of distance, and from 250 to 350 km the function drops to zero rapidly. The weighting function corresponding for the background field is $1 - \omega$.

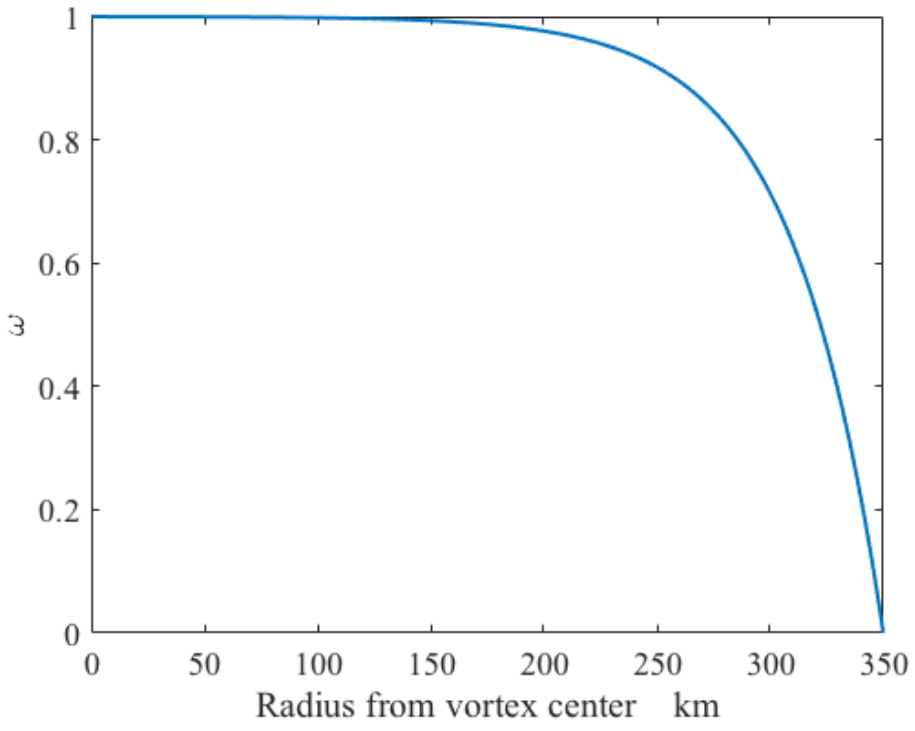

Figure A.3: Weighting function used in inserting the Rainkine vortex.

Appendix B

Description of 31 CMIP models

Table B.1: Descriptions of the 31 CMIP5 models in this study.

Model name	Modelling group
ACCESS1.0	Commonwealth Scientific and Industrial Research Organization and

See next page

Continued from previous page

Model name	Modelling group
	Bureau of Meteorology (CSIRO-BOM)
ACCESS1.3	Same as above
BCC-CSM1.1	Beijing Climate Center (BCC), China Meteorological Administration
BNU-ESM	College of Global Change and Earth System Science (GCESS), Beijing Normal University (BNU)
CanESM2	Canadian Centre for Climate Modelling and Analysis(CCCMA)
CCSM4	National Center for Atmospheric Research (NCAR)
CESM1-BGC	Same as above
CESM1-CAM5	Same as above
CMCC-CM	Centro Euro-Mediterraneo sui Cambiamenti Climatici (CMCC)
CNRM-CM5	Centre National de Recherches Météorologiques (CNRM)/Centre

See next page

Continued from previous page

Model name	Modelling group
	Européen de Recherche et Formation Avancée en Calcul Scientifique (CERFACS)
CSIRO-Mk3-6-0	CSIRO in collaboration with Queensland Climate Change Centre of Excellence (CSIRO-QCCCE)
FGOALS-g2	State Key Laboratory of Numerical Modeling for Atmospheric Sciences and Geophysical Fluid Dynamics (LASG), Institute of Atmospheric Physics, Chinese Academy of Sciences
FGOALS-s2	Same as above
GFDL-CM3	National Oceanic and Atmospheric Administration (NOAA) Geophysical Fluid Dynamics Laboratory (GFDL)
GFDL-ESM2G	Same as above

See next page

Continued from previous page

Model name	Modelling group
GISS-E2-H	National Aeronautics and Space Administration (NASA) Goddard Institute for Space Studies (GISS)
GISS-E2-R	Same as above
HadGEM2-AO	National Institute of Meteorological Research/KoreaMeteorological Administration (NIMR/KMA)
HadGEM2-ES	Same as above
INM-CM4	Institute for Numerical Mathematics (INM)
IPSL-CM5A-LR	L'Institut Pierre-Simon Laplace (IPSL)
IPSL-CM5A-MR	Same as above
IPSL-CM5B-LR	Same as above
MIROC-ESM	Japan Agency for Marine-Earth Science and Technology (JAMSTEC),

See next page

Continued from previous page

Model name	Modelling group
	Atmosphere and Ocean Research Institute (AORI; University of Tokyo), and National Institute for Environmental Studies (NIES) AORI (University of Tokyo), NIES, and JAMSTEC
MIROC-ESM-CHEM	Same as above
MIROC5	Same as above
MPI-ESM-LR	Max Planck Institute for Meteorology (MPI-M)
MPI-ESM-MR	Same as above
MRI-CGCM3	Meteorological Research Institute (MRI)
NorESM1-M	Norwegian Climate Centre (NCC)
NorESM1-ME	Same as above

Appendix C

Method to calculate TC track bias

Fig. C.1 shows the track of TC Hato (2017) in both WRF simulated (Blue line) and observed by HKO (Red line). In order to calculate the track bias between the simulations and observations, the perpendicular distance is used. For every time point in the WRF simulated track, such as the point C, two nearest time points, a and b, in the observed track could be found. Given the exact location of these three points, the perpendicular distance of C to AB can be calculated in the length of CD by applying trigonometric function.

$$CD = AC \times sin(\angle CAB) \tag{C.1}$$

For every simulated location of TC Hato (2018) over the ocean, a perpendicular distance could be calculated. Averaging all the obtained perpendicular distance, the TC bias can be derived.

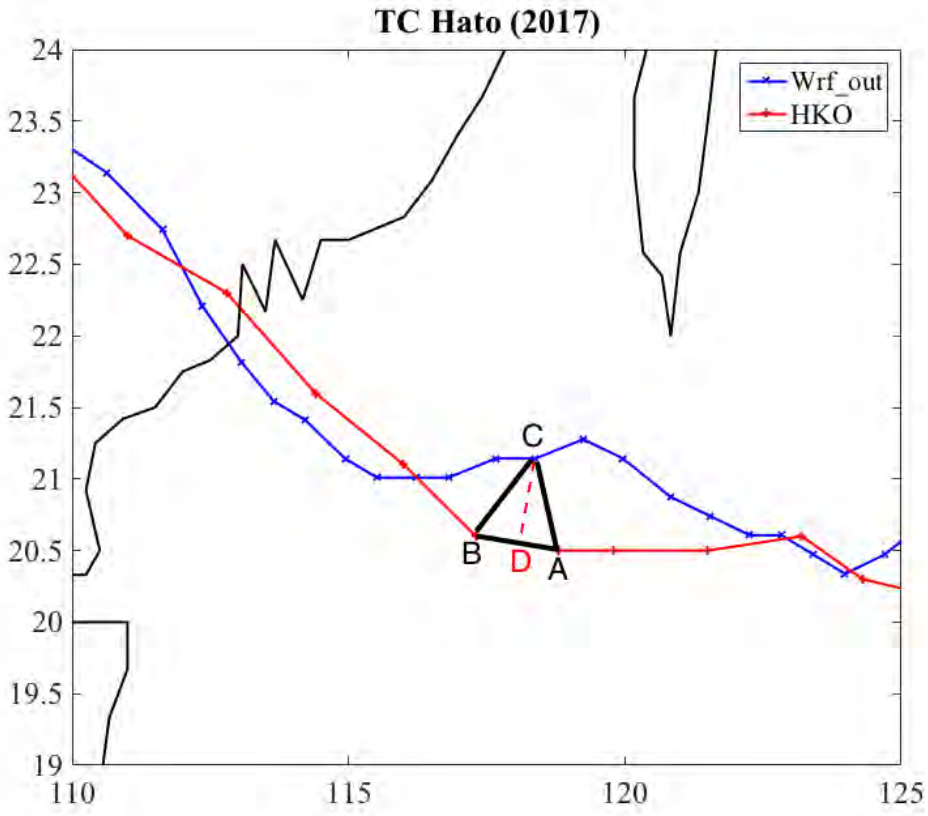

Figure C.1: Track of simulated and observed TC Hato (2017), for illustrating the way to calculate track bias